

Understanding Pattern Formation and Improving Fidelity in Phototropic Growth

Thesis by
Ethan Simonoff

In Partial Fulfillment of the Requirements for the degree of
Doctor of Philosophy



CALIFORNIA INSTITUTE OF TECHNOLOGY
Pasadena, California

2021
(Defended January 7, 2021)

© 2021

Ethan Simonoff
ORCID: 0000-0002-2156-8602

ACKNOWLEDGEMENTS

Firstly, I'd like to thank my advisor, Nathan Lewis, for allowing me to join his lab and research group. In particular I'd like to thank him for cultivating a group culture that embraces intellectual freedom and strong mentorship between all group members. I also want to separately thank Nate for sharing his expertise in paper-writing, project design, energy systems, his policy outlooks, and his stereo (I also can't forget to mention the citrus groves that continually bless the Lewis group with their incredible bounty).

I also have to thank the rest of my thesis committee for their help, especially over the last few months of my PhD. To Harry Gray, thank you for being a wonderful advocate for students everywhere and for being a great committee chair. To Jack Beauchamp and Bruce Brunschwig, thanks for all of your time spent in meetings and for all of the valuable feedback given on my graduation timeline and dissertation work.

I don't believe that any Lewis group member could make it through their studies here without the immense support offered by Kimberly Papadantonakis, Bruce Brunschwig, and Barbara Miralles. Kim, thank you so much for all of the roles you have played during my time here — advisor, editor, all-around advice-giver, and friend. Bruce, thank you for always being so invested and involved in the work of the group. Barbara, we would all be literally nowhere without you. Thank you for advocating for us and being such an integral part of the Lewis group.

I want to thank the Graduate Studies Office for the resources that they offer students. In particular, a very big thank you to Dean David Chan and Associate Dean Kate McAnulty for advocating for me and helping me to feel welcome here at Caltech, especially in the last year. Your

support during this time was so appreciated and helped to make one of the more stressful times in my life a little more manageable.

Thank you to all of the undergraduate students, graduate students, and post-docs I've interacted with since coming to Caltech — apologies if any of you are not listed specifically. You have all contributed to my experiences here in one way or another. Firstly, Azhar Carim, thank you for being one of the first Lewis group members I met on my visit weekend and helping me to find my first project, even if the “trees” remain elusive. I also would be remiss in not at least mentioning your social-planning abilities. Jonathan Thompson, I would not be where I am without your formal and informal mentorship, not to mention your friendship. I can also confidently say that the time spent doing absolute nonsense in lab or otherwise taught me as much as, if not more than, the “standard” lab work. If not for you, the Lewis group would also be without its tough little equine mascot, small in stature but by no means in personality. Also, I will never forgive you for the cake incident. To all the rest of the Squigglers and LMI (now since passed) people, thanks for all of the time spent looking at blue plots, discussing research, drinking coffee, and eating pizza — Nick Batara, Katie Hamann, Madeline Meier, and Sisir Yalamanchili. Though you didn't get any free pizza, Sean Byrne, we're happy to have you anyway. Lorenzo Van Muñoz, thanks for being just about the best SURF anyone could ever ask for.

Noyes is a wonderful building full of wonderful people and glorious premises. Thanks to everyone in Noyes 220 way back when we had offices. Annelise Thompson, Michael Mazza (and Richie!), Ellen Yan, Maureen Morla (and Sumi!), and anyone else who ever stopped by or squatted in a desk in our little burrow. Whether sweating and squiggling during the summer solstice or eating hazelnuts during the solar eclipse, my time at Caltech has been made better by knowing you all — and by the paperclip game. Paul Kempler — many a day we spent building and rebuilding the

evaporator... but really, we were building our friendship. Katherine Rinaldi — wow, thanks for the invite. But really, thanks for being a good friend and also for inviting me to the Abolition Study Group. Weilai Yu — thank you for the tea and for your wonderful photography!

I have to thank my family, especially my parents, for giving me so much support both prior to and during my graduate studies. To my brothers, Aaron and Michael, thanks for asking about my research even when I didn't make any sense or sounded like I was speaking gibberish. To my mom and dad, I would definitely not be here today without your guidance and love. Thanks for always pushing me to succeed and supporting me no matter what. This past year has been especially difficult for all of us – I am thankful for all of you and I love you all.

Finally, I want to say thank you to my fiancée, Monica Dimson. There isn't enough I could say to truly show how much I appreciate all of the emotional and other support you've given me over the past few years. Nevertheless, thank you for everything you have given me and for continually helping me to grow to become a better person. You are a wonderful role model and one of the most thoughtful and talented people I have ever met. I will always appreciate the treats you baked me, the times you serenaded me, and the ways in which you make our home so beautiful.

ABSTRACT

Phototropic growth of Se-Te yields highly anisotropic lamellar nanostructures and is achieved photoelectrochemically from an isotropic solution of oxidized Se and Te precursors deposited onto isotropic conductive substrates under conformal illumination. In contrast to other spontaneous patterning processes, phototropic growth has no requirement for illumination source coherency and can be performed under mild conditions using low illumination power. Furthermore, as a bottom-up, solution-based synthesis, phototropic growth is scalable and demonstrates high tunability via optical input (i.e., control of wavelength and polarization). However, relative to more traditional lithographic patterning methods, phototropically grown films exhibit defective patterns which may impede their application in devices requiring high pattern fidelities.

Chapter I investigates the role of the growth substrate and its effect on pattern fidelity in phototropically grown Se-Te films, quantified by peak-fitting and analysis of frequency modes in 2D Fourier transform spectra. The work function or Fermi level of the substrate was determined to be the major factor in determining pattern fidelity. Substrates that had work functions closely aligned with Se-Te (p^+ -Si and Au) demonstrated higher fidelity patterns than those that had misaligned work functions (n^+ -Si and Ti). In cases of both nominally identical illumination conditions and nominally identical growth rates, phototropically grown Se-Te films on p^+ -Si exhibited a higher degree of anisotropy and higher pattern fidelity than phototropically grown Se-Te films on n^+ -Si, attributed to energetics and charge conduction at the junction formed by the substrate and growing Se-Te film.

Chapter II follows up on the analysis performed in **Chapter I** by investigating the role of nucleation and the earliest levels of mass addition to growth substrates in the phototropic growth of Se-Te films. In particular, the relationship between the inter-nucleate spacing of the initial dark

electrodeposited material and the pattern formation pathways during the phototropic growth process is described. Conditions that produced small nucleate spacings resulted in phototropically grown films with a higher pattern fidelity and a pattern period that more strongly agreed with the theoretical trend ($\lambda/2n$). Furthermore, on substrates that generally produced low pattern fidelity films, use of an applied striking potential during the initial nucleation stage demonstrated both smaller nucleate spacings and improved pattern fidelity of resulting phototropically grown films.

Finally, **Chapter III** investigates the effect of extrinsic (i.e., lithographically patterned) optical scattering elements on the phototropic growth process. Relative to non-templated substrates, substrates with templated ridges demonstrated higher pattern fidelities, confined pattern periods, and enforced pattern orientation. Full-wave electromagnetic modeling and Monte Carlo growth simulations of Se-Te onto simulated templated substrates resulted in simulated films demonstrating good agreement with the patterns observed experimentally. In simulation, for a given set of illumination conditions that produced a single pattern period on non-templated substrates, films grown on templated substrates were able to attain a much wider range of periods (~80% to ~160% vs. the non-templated pattern period). Additionally, the orientation of phototropically grown patterns (usually dependent on the axis polarization) were enforced to the orientation of the templates to an angular offset tolerance of up to $\sim 40^\circ$.

PUBLISHED CONTENT AND CONTRIBUTIONS

Chapter I:

Simonoff, E.; Lichterman, M. F.; Papadantonakis, K. M.; Lewis, N. S., Influence of Substrates on the Long-Range Order of Photoelectrodeposited Se-Te Nanostructures. *Nano Lett* **2019**, *19* (2), 1295-1300. doi: 10.1021/acs.nanolett.8b04891

E.S. designed the project, performed all experiments, imaged all samples, performed all image analysis, performed all solid-state tests, prepared all data and figures, and wrote the manuscript.

Chapter II:

Simonoff, E.; Van Munoz, L. X.; Lewis, N. S., Increased spatial randomness and disorder of nucleates in dark-phase electrodeposition lead to increased spatial order and pattern fidelity in phototropically grown Se-Te electrodeposits. *Nanoscale* **2020**, *12* (44), 22478-22486. doi: 10.1039/d0nr07617a

E.S. designed the project, performed experiments, imaged all samples, performed image analysis, prepared all data and figures, and wrote the manuscript.

Chapter III:

Simonoff, E.; Thompson, J. R.; Meier, M. C.; Kennedy, K.; Hamann, K. R.; Lewis, N.S., *Manuscript in Preparation*.

E.S. co-designed the project, performed all experiments, performed all image analysis, prepared all data and figures, and wrote the manuscript.

TABLE OF CONTENTS

Acknowledgements	iii
Abstract.....	vi
Published Content and Contributions	viii
Table of Contents	ix
Chapter I: Influence of Substrates on the Long-Range Order of Photoelectrodeposited Se-Te Nanostructures.....	
1.1 Introduction.....	1
1.2 Results and Discussion.....	3
1.2.1 Matched-illumination growth conditions	3
1.2.2 Nucleation dynamics.....	6
1.2.3 Junction analysis.....	8
1.2.4 Matched deposition-rate conditions.....	12
1.3 Conclusion	15
1.4 Supporting Information	16
1.4.1 Experimental methods and materials.....	16
1.4.2 Low-magnification SEM images used for FT analysis in Figure 1.1	21
1.4.3 Additional data gathered for Se-Te films deposited on n+-Si and p+-Si substrates	22
1.4.4 Results and data gathered for Se-Te films deposited on Au and Ti substrates	27
1.4.5 Low-magnification SEM images of Se-Te films on p+-Si in Figure 1.5	30
1.4.6 Nucleation density and growth substrate discussions	31
1.4.7 Table with additional information for all samples fabricated.....	33
1.5 References.....	36
Chapter II: Increased Spatial Randomness and Disorder of Nucleates in Dark-Phase Electrodeposition Lead to Increased Spatial Order and Pattern Fidelity in Phototropically Grown Se-Te Electrodeposits	
2.1 Introduction.....	38
2.2 Results and Discussion.....	39
2.3 Conclusion	53
2.4 Supporting Information	55
2.4.1 Experimental methods and materials.....	55
2.4.2 Examples of low-magnification images	55
2.4.3 Reproducibility	57
2.4.4 Pair-correlation function (PCF) examples.....	61
2.4.5 Peak-fitting methodologies	62
2.4.6 Schemes for phototropic growth mechanism	65
2.4.7 Electron dispersive X-ray spectroscopy (EDS) compositional analysis	67

2.4.8	Extended discussion of Fourier transforms and SEM images in Figure 2.2.....	68
2.4.9	Graphical representation of striking potential	71
2.4.10	Dark growth during Se-Te electrodeposition on n ⁺ -Si.....	72
2.4.11	Summary of previous phototropic growth studies	73
2.4.12	Se-Te on Au substrates.....	74
2.5	References.....	76
Chapter III: Pre-seeded Optical Scatterers as a Template for Phototropic Growth ..		80
3.1	Introduction.....	80
3.2	Results and Discussion	82
3.3	Conclusion	98
3.4	Experimental Methods and Materials	99
3.5	References.....	104

CHAPTER I

Influence of Substrates on the Long-Range Order of Photoelectrodeposited Se-Te Nanostructures

Simonoff, E.; Lichterman, M. F.; Papadantonakis, K. M.; Lewis, N. S., Influence of Substrates on the Long-Range Order of Photoelectrodeposited Se-Te Nanostructures. *Nano Lett* **2019**, *19* (2), 1295-1300. doi: 10.1021/acs.nanolett.8b04891

1.1 Introduction

Highly anisotropic nanoscale lamellar patterns spontaneously develop over macroscopic areas during electrodeposition of phototropic Se-Te alloy films onto unpatterned substrates illuminated uniformly by incoherent polarized light.¹ The lamellae adopt an orientation parallel to the direction of polarization, and the width and periodicity of the lamellae are controlled by the intensity-weighted average wavelength of the illumination.² The patterns of the phototropic Se-Te films respond dynamically during growth to changes in the illumination, enabling the template-free synthesis of complex three-dimensional nanostructures with fully controllable morphologies based on controlling the properties of the incident light during the phototropic growth process.¹ Phototropic growth may therefore offer an intrinsically three-dimensional approach to the design and synthesis of adaptive, complex, mesostructured materials with a variety of novel properties, including materials with optical properties tailored for use as elements in next-generation optical devices (e.g., lenses, filters, modulators), light absorbers in thin-film solar cells or photodetectors, and mesoscopic materials for supporting thermal or electrochemical catalysts with controlled electronic and ionic conductivity.

The Se-Te alloys are semiconductors with energy-band gaps (E_g) that are between those of Se ($E_g \sim 1.85$ eV) and Te ($E_g \sim 0.33$ eV), depending on the ratio of Se to Te as well as the crystallinity of the material.³⁻⁶ Phototropic growth with consequent optically based nanoscale morphology control has also been observed for PbSe films, suggesting that the phenomenon may be general for semiconductors with short minority-carrier diffusion lengths.⁷ A model that combines full-wave optical simulations with weighted Monte-Carlo mass addition accurately reproduces the average pattern period and morphology for phototropic Se-Te structures grown under multiple and complex optical inputs.^{2, 8, 9}

Se-Te photoelectrodeposits exhibit phototropic growth on a variety of substrates, including Au, highly oriented pyrolytic graphite, n^+ -Si(111), and p-Si(100).¹ Hence the atomic-level structural properties of the substrate/film interface do not substantially influence the morphology of the resultant photoelectrodeposited phototropic Se-Te film. Electrochemical reactions of semiconductors involve the conduction of charge through either the conduction or valence band, and often are affected by differences in the behavior and distribution of charge carriers under dark or illuminated conditions, as in the anodic etching of Si.¹⁰⁻¹² Band conduction and the electrochemical behavior of semiconductors are important during the deposition of metals onto structured Si working electrodes, with the work function of the deposited metals influencing the spatial distribution of the electrodeposit, either in the dark or under illumination.¹³ In addition, wavelength-dependent light-absorption profiles have been shown to direct deposition of metal anisotropically onto patterned, photoactive Si microwire arrays.¹⁴

After an initial light-independent deposition phase, phototropic growth of the Se-Te films results from absorption of light with energy above the Se-Te band gap, producing an electron-hole

pair. Photogenerated electrons that reach the Se-Te/electrolyte interface reduce oxidized Se or Te species dissolved in the solution, whereas photogenerated holes are collected at the back contact to the Se-Te film. Holes must be conducted across the back contact, so the energetics of the interface between the phototropically growing semiconducting electrodeposit and the substrate may influence the morphology and growth of the phototropic film. Herein we examine whether and how the substrate influences the development of the lamellar patterns in photoelectrodeposited Se-Te films, with a focus on possible electrical effects due to the energetics of the junction between the substrate and the phototropic semiconducting film.

1.2 Results and Discussion

Detailed experimental procedures are provided in the Supporting Information. Se-Te films were deposited potentiostatically from an aqueous bath of 1.00 M H₂SO₄, 0.020 M SeO₂, and 0.010 M TeO₂. The p⁺-Si and n⁺-Si planar substrates had a resistivity < 0.005 Ω-cm and had a (111) ± 0.5° crystal orientation. Unless otherwise noted, all substrates were illuminated with constant, vertically polarized light from a narrow-band light-emitting diode (LED) source producing an intensity-weighted average wavelength of 927 nm at a nominally uniform power density of 53 mW cm⁻² over the whole substrate. Mass was deposited by cathodic deposition until a total charge density of -750 mC cm⁻² had passed through the working electrode.

1.2.1 Matched-illumination growth conditions

Figure 1.1a and b show representative scanning-electron microscopy (SEM) images of Se-Te films grown on p⁺-Si and n⁺-Si substrates, respectively. The films grown on p⁺-Si exhibited a

higher degree of anisotropy along the axis of optical polarization than films grown on n^+ -Si, and more defects were apparent in the patterns of the n^+ -Si/Se-Te films than in the p^+ -Si/Se-Te films. Figure S1.1a and b provide high-resolution, low-magnification images showing wide areas of the photoelectrodeposited Si/Se-Te films that contain the regions shown in Figure 1.1a and b.

Figure 1.1c and d show two-dimensional Fourier transforms (2D FT) of wide-area images of phototropic Se-Te films grown on p^+ -Si and n^+ -Si substrates. The 2D FT data were converted to and analyzed in the polar coordinate system where the radial coordinate, r , is the linear distance from the center of the FT, equivalent to the periodicity of the pattern in real space. The angular coordinate, θ , is the angle formed between the position of the radial coordinate and the positive x axis in Cartesian coordinates, equivalent to the direction of the pattern. Thus, the horizontal component of the 2D FT was evaluated where $\theta = 0$ (and $r = x$) along the direction perpendicular to the polarization vector used during film growth, and reflects the spacing of the lamellae in the SEM images, with a narrow band in the horizontal component of the 2D FT corresponding to a lamellar pattern with a highly defined period. The vertical component of the 2D FT was then evaluated at a distance, r , corresponding to the position of the primary FT band as determined by the peak position in the horizontal direction. The vertical component is parallel to the polarization vector used during film growth and reflects the alignment of the lamellae with the axis of polarization. A narrow band in the vertical component of the 2D FT corresponds to a highly anisotropic pattern, approaching perfectly parallel and straight lamellae.

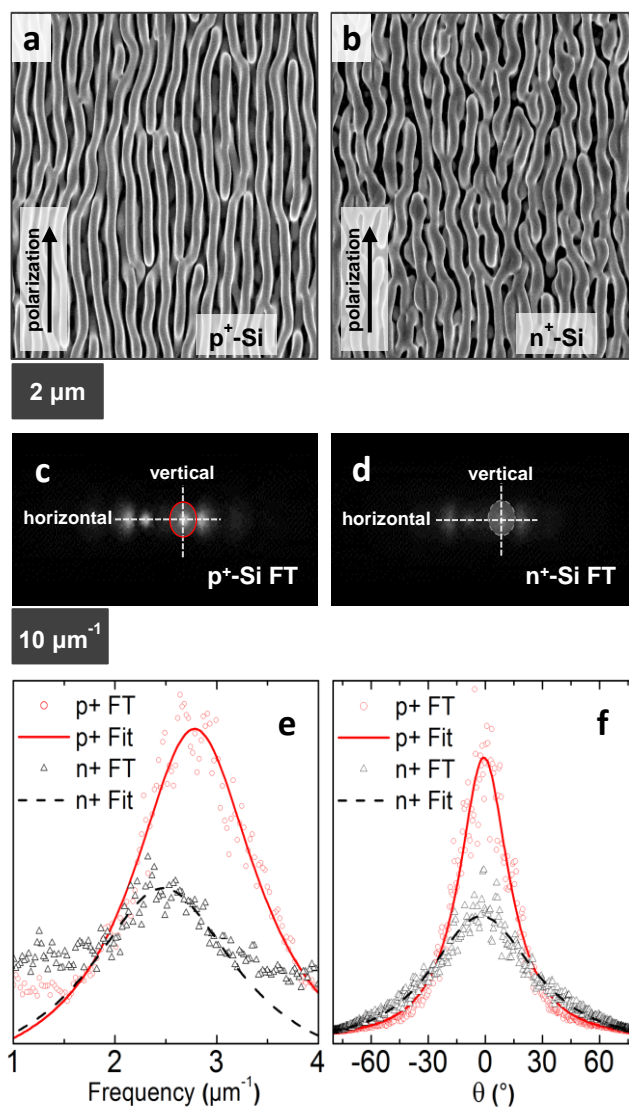


Figure 1.1. Representative SEM images of SeTe photoelectrodeposited on (a) p⁺-Si and (b) n⁺-Si substrates using vertically polarized illumination with $\lambda = 927$ nm and a power density of 53 mW cm⁻². (c) and (d) 2D FT spectra generated from wide-area SEM images including the regions depicted in (a) and (b), respectively, with primary FT bands highlighted. Co-plotted (e) horizontal (normal to polarization) and (f) vertical (parallel to polarization) surface profiles of integrated intensity and Lorentzian curve fits for the primary FT bands in the 2D FT spectra in (c) and (d).

Figure 1.1e and f show the horizontal and vertical surface profiles that were extracted from the bands corresponding to the primary periods in the 2D FTs shown in Figure 1.1c and d. For the horizontal and vertical profiles, the bands were sharper for p⁺-Si/Se-Te than for n⁺-Si/Se-Te films,

consistent with a more defined pattern, and straighter lamellae, for Se-Te films grown on p⁺-Si substrates than on n⁺-Si substrates. The horizontal and vertical profiles were fitted to Lorentzian functions, and the full-widths at half maximum (FWHMs) of the fitted peaks provide figures-of-merit for the uniformity of the lamellar Se-Te structure. The FWHMs of the fits to the horizontal profiles were 1.49 μm^{-1} and 1.77 μm^{-1} for p⁺-Si/Se-Te and n⁺-Si/Se-Te films, respectively. For the vertical profiles, the FWHMs were 30.9° and 57.9° for p⁺-Si/Se-Te and n⁺-Si/Se-Te films, respectively. Average horizontal FWHM values for samples prepared under nominally identical conditions were $1.44 \pm 0.26 \mu\text{m}^{-1}$ and $1.79 \pm 0.07 \mu\text{m}^{-1}$ for p⁺-Si/Se-Te and n⁺-Si/Se-Te films, respectively. For the vertical FWHM values, averages for p⁺-Si/Se-Te were $31.3^\circ \pm 1.0^\circ$; for n⁺-Si/Se-Te films, averages were $63.4^\circ \pm 10.1^\circ$.

Films grown on the different substrates yielded different locations in reciprocal Fourier space of the maxima of the peaks fitted to the horizontal surface profiles, with higher values in reciprocal Fourier space corresponding to smaller periods in real space. The fit to the peak associated with p⁺-Si/Se-Te films was centered at 2.79 μm^{-1} , corresponding to an average period of 358 nm, whereas the fit to the peak associated with n⁺-Si/Se-Te films was centered at 2.47 μm^{-1} , corresponding to an average period of 405 nm. This increase in the average period results from the higher degree of disorder in the pattern, which led to a less closely packed pattern for the n⁺-Si/Se-Te films as compared to the p⁺-Si/Se-Te films.

1.2.2 Nucleation dynamics

To elucidate the development of the patterns in the phototropically grown films as well as any differences in how the phototropic patterns develop on the two differently doped types of Si

substrates, the phototropic growth of Se-Te films on p⁺-Si or n⁺-Si was observed at several steps early in the photoelectrodeposition process. Figure 1.2 shows the structures observed during nucleation and development of the phototropic Se-Te films. At low levels of mass deposited and cathodic charge density passed (-0.75 mC cm⁻²), the morphology of the phototropic Se-Te deposit was nearly identical on both substrates, with more uniform nucleation on p⁺-Si (Figure 1.2a), and the initial development of some larger islands on n⁺-Si (Figure 1.2f). On p⁺-Si substrates, as additional cathodic charge density (-3.75 mC cm⁻²) was passed, the deposition density sharply increased, resulting in a thin, continuous film (Figure 1.2b). In contrast, on n⁺-Si substrates, larger nucleated sites continued to develop (Figure 1.2g). At the next step in cathodic charge density (-37.5 mC cm⁻²), a nearly continuous film of nucleation sites was observed on p⁺-Si (Figure 1.2c) whereas on n⁺-Si the film remained discontinuous even though the nucleation sites were larger than for the previous current step (Figure 1.2h). At the subsequent charge density step (-75 mC cm⁻²), on p⁺-Si the nucleation sites had merged into a lamellar pattern (Figure 1.2d), whereas void space and islanded nucleation sites were still present on n⁺-Si even though some nucleation sites had merged (Figure 1.2i). After the final charge density step (-750 mC cm⁻²), the phototropically grown films on p⁺-Si (Figure 1.2e) and n⁺-Si (Figure 1.2j) had developed into structures with mutually similar lamellar patterns, but with mutually distinctive and clearly identifiable differences in the pattern fidelity.

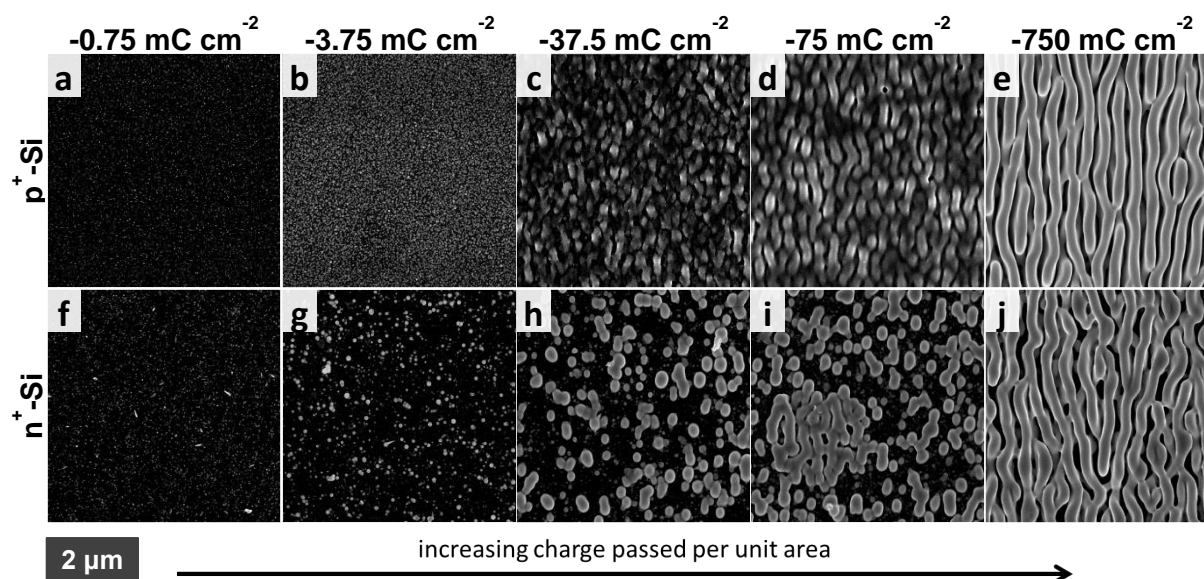


Figure 1.2. Series of SEM images demonstrating films with characteristic amounts of charge passed (mass deposited) per unit area on (a-e) p⁺-Si and (f-j) n⁺-Si with (a), (f) at -0.75 mC cm⁻²; (b), (g) at -3.75 mC cm⁻²; (c), (h) at -37.5 mC cm⁻²; (d), (i) at -75 mC cm⁻²; and (e), (j) at -750 mC cm⁻².

1.2.3 Junction analysis

To further investigate the reasons for the variation in nucleation dynamics and resulting film morphologies on the two types of Si substrates, the electrical characteristics of junctions formed between Se-Te films and p⁺-Si or n⁺-Si substrates were investigated (see Supporting Information for detailed experimental methods describing solid-state measurements). Figure 1.3a shows the current density versus voltage, J - V , behavior of Se-Te deposited on p⁺-Si or n⁺-Si. The linear J - V relationship for Se-Te deposited on p⁺-Si indicates an ohmic contact, whereas the J - V relationship between Se-Te and n⁺-Si was non-linear. The Si substrates had nominally mutually equal resistivity, thickness, and crystal orientations, and nominally only differed in dopant type and Fermi level. The lower current density observed for Se-Te films grown on n⁺-Si relative to the current density for Se-Te

grown on p^+ -Si at the same applied potential is thus consistently ascribable to the presence of a non-ohmic voltage drop at the n^+ -Si/Se-Te junction.

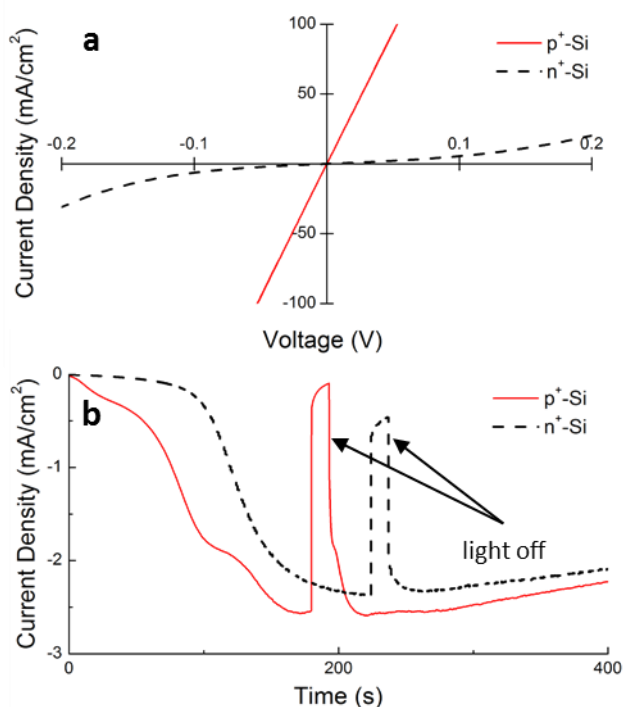


Figure 1.3. (a) Current-voltage behavior of Se-Te on p^+ -Si and n^+ -Si. (b) Chopped-light chronoamperometry experiments showing the ratio of light to dark current density for Se-Te films representative of those grown on p^+ -Si and n^+ -Si.

Figure 1.3b shows the change in current density with time for representative Se-Te films photoelectrodeposited on p^+ -Si or n^+ -Si substrates. The substrates were held for ~ 200 s at a potential of -0.065 V (for p^+ -Si) and -0.200 V (for n^+ -Si) vs. Ag/AgCl, under nominally mutually identical injection conditions (53 mW cm^{-2} illumination power). The light was then blocked for 10 s. Throughout the photoelectrodeposition, the cathodic photocurrent densities for phototropic Se-Te growth on p^+ -Si were greater than those for phototropic Se-Te growth on n^+ -Si (Figure 1.3b); for example, immediately prior to the light being blocked, a photocurrent density of -2.44 mA cm^{-2} was

measured for Se-Te on p⁺-Si, whereas a photocurrent density of -1.89 mA cm⁻² was observed for Se-Te on n⁺-Si. Additionally, the dark current comprised a larger proportion of the total current for films grown on n⁺-Si than for films grown on p⁺-Si. For example, in the dark, -0.09 mA cm⁻² was passed by Se-Te on p⁺-Si, while -0.47 mA cm⁻² was passed by Se-Te on n⁺-Si. The photocurrent from the Se-Te film was negative, indicating that the film exhibited p-type conductivity during the deposition. These results are characteristic of the general morphology produced by inorganic phototropic growth of Se-Te films on p⁺-Si or n⁺-Si (Figure S1.4).

Figure S1.3 shows the ultraviolet photoelectron spectroscopy (UPS) data for as-deposited and for sputter-cleaned Se-Te films. After removal of a surface oxide via sputter-cleaning, the work function, ϕ_m , of Se-Te was measured to be ~5 eV, and the position of the valence-band maximum (VBM) relative to the Fermi level (E_F), or $VBM - E_F$, was ~395 meV for Se-Te deposited on both n⁺-Si and p⁺-Si substrates. For a film of 60-80 at.% Te, the optical bandgap, E_g , of Se-Te has been experimentally determined to be 1.06 eV.⁶

Figure 1.4 shows a simplified band diagram¹⁵ for Se-Te in contact with p⁺-Si or n⁺-Si.¹⁶ During the deposition of Se-Te, photogenerated electrons, i.e., the minority carriers, are collected at the dynamic semiconductor-solution interface and result in mass addition to the growing film. For the photo-driven mass-addition process to occur, the photogenerated holes must thus be collected at the Si/Se-Te junction before recombining. In the case of p⁺-Si/Se-Te films, the observed ohmic contact and proximity of the observed work function measured for Se-Te to the valence-band maximum of Si suggest a minimal barrier to hole collection at that interface. Conversely, the difference between the work functions of Se-Te and n⁺-Si implies the presence of a substantial barrier

to hole collection, thus inhibiting the flow of photocurrent into solution and preventing mass addition to the electrodeposit.

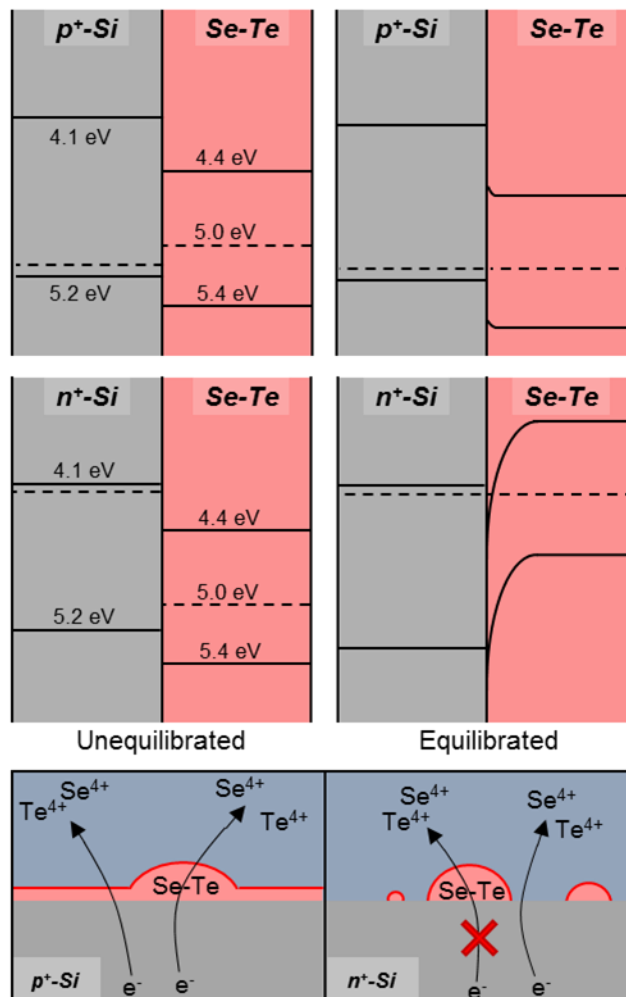


Figure 1.4. Simplified band diagrams showing the energies of the band positions relative to the vacuum level and the expected trends in the equilibration of the junctions formed by n^+ -Si or p^+ -Si with Se-Te. Lower panel shows a schematic with the hypothesized preferential pathways for mass deposition during the electrodeposition of Se-Te. In the case of the n^+ -Si/Se-Te interface, the non-ohmic potential drop inhibits deposition onto nucleated Se-Te sites.

The observed junction behavior between Se-Te and the Si growth substrates can explain the nucleation dynamics observed in Figure 1.2. The non-ohmic contact between n^+ -Si and Se-Te would enhance electrical isolation of the nucleated Se-Te sites, due to the potential drop at the junction with

n^+ -Si. The variation in the material in contact with the solution would lead to a surface of mixed barrier height across the partially nucleated n^+ -Si substrate. This behavior is consistent with the sustained discontinuous nature of the film grown on n^+ -Si (vs. the continuous films present on p^+ -Si), even at late stages of deposition.

1.2.4 Matched deposition-rate conditions

Under nominally mutually identical illumination power, Se-Te films phototropically grown on p^+ -Si substrates were observed to exhibit greater photocurrent densities, and thus to grow faster, than phototropically grown Se-Te films on n^+ -Si substrates. Se-Te films were therefore grown on p^+ -Si substrates with the applied potential and illumination power tuned such that the photocurrent densities, and the ratios of light to dark current density, matched to within 15% the values for films grown on n^+ -Si. Figure 1.5 shows three such matched pairs of growths, providing examples of samples having matched rates of deposition for relatively low ($\sim -0.5 \text{ mA cm}^{-2}$), intermediate ($\sim -0.7 \text{ mA cm}^{-2}$), and high ($\sim -1.0 \text{ mA cm}^{-2}$) total current densities. See Figure S1.9 for large-area SEM images of these images. The films deposited on p^+ -Si exhibited patterns with fewer defects and straighter, more anisotropic lamellae, whereas films on n^+ -Si exhibited patchier morphologies and patterns with more defects. These observations correlated with much sharper horizontal and vertical 2D FT peaks (Table 1) for phototropic p^+ -Si/Se-Te films than for phototropic n^+ -Si/Se-Te films.

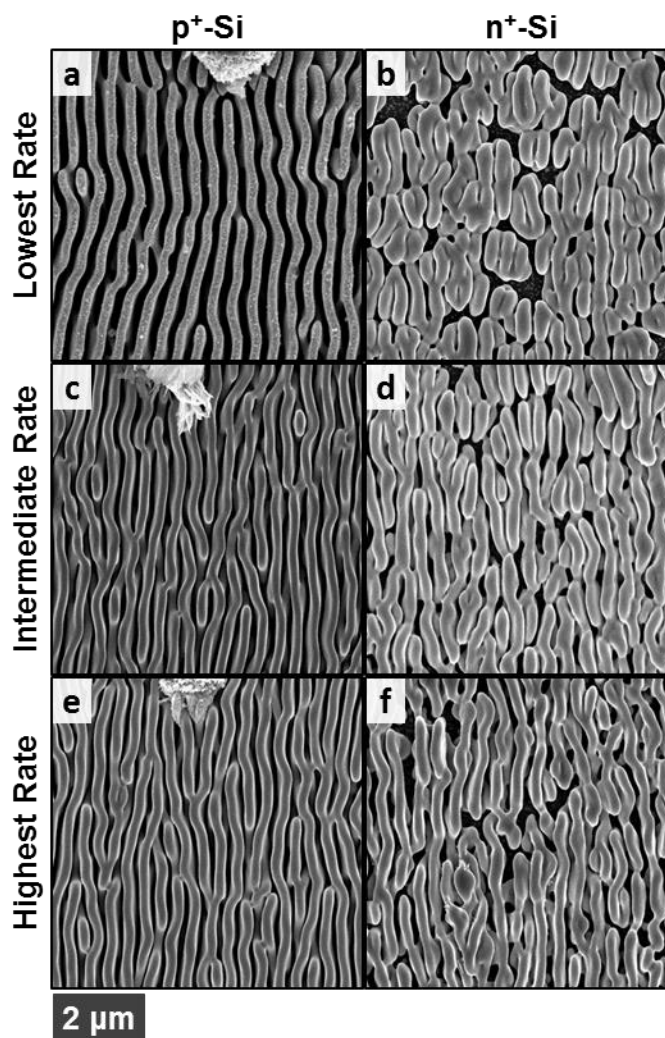


Figure 1.5. Se-Te films grown at (a), (b) low, $\sim -0.5 \text{ mA cm}^{-2}$; (c), (d) intermediate, $\sim -0.7 \text{ mA cm}^{-2}$; and (e), (f) high, $\sim -1.0 \text{ mA cm}^{-2}$, matched relative deposition rates on (a), (c), (e) $\text{p}^+\text{-Si}$ and (b), (d), (f) $\text{n}^+\text{-Si}$.

Films grown on $\text{n}^+\text{-Si}$ exhibited an increased photocurrent density at more negative applied potentials whereas films grown on $\text{p}^+\text{-Si}$ showed less relative change in the observed photocurrent density with applied potential (Figure S1.4). Figure S1.5 shows the FWHMs for the 2D FTs for the films deposited at varied growth rates on $\text{p}^+\text{-Si}$ or $\text{n}^+\text{-Si}$ substrates. Films grown on $\text{p}^+\text{-Si}$ at low rates resulted in narrower 2D FT bands than films deposited at higher rates. The opposite trend was

observed for films grown on n^+ -Si, with films grown on n^+ -Si at lower relative rates having broader 2D FT bands than films grown at high rates. Figure S1.6 and S1.7 show that the same general trend was observed for films deposited on metals of varying work function, with Se-Te deposited on metal substrates having work functions closely aligned with Se-Te (i.e., Au, $\phi_m = 5.3$ -5.4 eV) exhibiting higher photocurrent densities, and less defective patterns, than films deposited on substrates having a work function misaligned with Se-Te (i.e., Ti, $\phi_m = 4.33$ eV).¹⁷ In addition, Figure S1.8 shows the J - V behavior of Se-Te films on substrates that exhibited better electrical contact than was observed for Ti contacts to Se-Te.

Table 1. Growth Parameters and FT Analysis of Structures Grown with Matching Rates of Deposition

	<i>growth substrate</i>	
	<i>p+ Si</i>	<i>n+ Si</i>
<i>Lowest Growth Rate</i>		
peak current density (mA cm ⁻²)	-0.515	-0.483
light-to-dark current ratio	2.22	2.41
FT horizontal FWHM (μm ⁻¹)	0.59	2.48
FT vertical FWHM (°)	33.7	104.2
<i>Intermediate Growth Rate</i>		
peak current density (mA cm ⁻²)	-0.685	-0.705
light-to-dark current ratio	2.74	3.17
FT horizontal FWHM (μm ⁻¹)	1.10	2.51
FT vertical FWHM (°)	30.1	72.9
<i>Highest Growth Rate</i>		
peak current density (mA cm ⁻²)	-1.031	-1.077
light-to-dark current ratio	3.91	4.21
FT horizontal FWHM (μm ⁻¹)	1.00	1.73
FT vertical FWHM (°)	31.4	57.3

Nucleation may play a role in the effect of deposition rate on the fidelity of the Se-Te film pattern (Figure S1.10). To achieve higher rates of growth, the required relative applied potentials

were more negative, leading to decreases in the band bending at the interface between n^+ -Si and Se-Te. Consequently, Se-Te nucleation may be denser on n^+ -Si at these more negative potentials. Conversely, the ohmic contact between Se-Te and p^+ -Si suggests negligible barrier to nucleation at less negative potentials. In both cases, the observed higher-fidelity patterns are consistent with expectations for the formation of more continuous and thin film nucleation relative to island nucleation of Se-Te deposits.

1.3 Conclusion

In summary, in all cases examined herein, the fidelity of the pattern was greater for phototropic Se-Te films grown on p^+ -Si substrates than for phototropic Se-Te films grown on n^+ -Si. Parameterization using only conditions of deposition rate and illumination power does not allow prediction of the pattern fidelity or of the observed differences in film properties on either substrate. However, the energetics of the junction between the phototropic Se-Te film and the substrate influences the nucleation dynamics and subsequent morphological variation and pattern fidelity, thus providing an example of the influence of interfacial electrical effects, as opposed to structural effects, of the substrate on the morphology of phototropically grown Se-Te films.

1.4 Supporting Information

1.4.1 Experimental methods and materials

Chemicals and Materials

SeO₂ (Aldrich, 99.999% trace metals basis), TeO₂ (Aldrich, 99.995% trace metals basis), Buffer HF Improved (BHF) (Transene, Ammonium Hydrogen Difluoride Solution), H₂SO₄ (J.T. Baker, 90-100%), Nickel Sulfamate Solution (Transene), Ga (Alfa Aesar, 6mm diameter pellets, 99.9999% trace metals basis), In (ESPI Metals, shot, 99.9999%), Acetone (BDH, ACS Grade, 99.5% min.), Isopropyl Alcohol (BDH, ACS Grade, 99.5% min.), Ir wire (Alfa Products, 1mm dia., 99.9%), and Ni pellets (Kurt J. Lesker, 1/4" dia. x 1/4" long, 99.995%) were used as received. H₂O (Barnstead Nanopure Infinity Ultrapure Water System, $\rho = 18.3 \text{ M}\Omega\text{-cm}$) was used throughout.

Silicon substrates used as working electrodes include n⁺ silicon (Addison Engineering Inc., As-doped, $\rho = 0.001\text{-}0.004 \text{ }\Omega\text{-cm}$, [111], $525 \pm 25 \text{ }\mu\text{m}$ thick, SSP) and p⁺ silicon (Virginia Semiconductor Inc., B-doped, $\rho < 0.0025 \text{ }\Omega\text{-cm}$, [111], $500 \pm 25 \text{ }\mu\text{m}$ thick, SSP).

Loctite 1C Hysol Epoxy Adhesive, Conductive Silver Paint (SPI Supplies), Clear Nail Polish (Sally Hansen "Hard as Nails Xtreme Wear"), tinned Cu wire (AWG 22), and glass tubing (7740 Borosilicate Pyrex, 9mm OD x 1.0mm wall thickness) were used to fabricate electrodes.

Preparation of Au and Ti Metal Substrates

Au and Ti substrates used as working electrodes in the deposition of Se-Te were fabricated via electron-beam evaporation of the target metals onto n⁺-Si wafers. Prior to metal evaporation and loading into the vacuum chamber, n⁺-Si wafers were etched in BHF until the native silicon oxide layer was removed from both the top and bottom sides of the Si. For Au substrates, 20 nm of Ti and

70 nm of Au were evaporated onto the polished side of n⁺-Si; for Ti substrates, 100 nm of Ti was evaporated. Evaporated Ti was used as an ohmic contact layer to the n⁺-Si (and additionally as an adhesion layer in the case of the Au substrates). 20 nm of Ti was evaporated onto the back side of the n⁺-Si wafers as an ohmic back contact for both substrates.

Silicon and Metal Electrode Fabrication

Au substrates, Ti substrates, p⁺-Si, and n⁺-Si wafers were cleaved into small chips (between 0.01 cm² and 0.15 cm²) to be fabricated into working electrodes. Ga-In eutectic (75.5 wt. % gallium, 24.5 wt. % indium) was prepared and scratched into the back of the n⁺-Si and p⁺-Si pieces using a carbide-tipped scribe. Electrode mounts were fabricated from glass tubing (~5-6 inches long) and tinned Cu wire bent into a flat coil and affixed to the glass tube using inert epoxy. The exposed flat coil on the electrode mount was placed in contact with the Ga-In coated surface of the silicon or metal-coated chip and was glued in place using Ag paint. After the Ag paint had dried, clear nitrocellulose nail polish was applied to temporarily electrically insulate the tinned Cu wire, Ag paint, and backside of the electrode.

Iridium Wire Electrode Fabrication

A piece of Ir wire (~30 mm) was soldered to a ~6-inch segment of tinned Cu wire and placed in a ~5-inch glass tube. The soldered contact and glass tube opening nearest to the Ir wire was insulated with inert epoxy.

Nickel Electrode Fabrication

A single Ni pellet was soldered to a ~6-inch segment of tinned Cu wire. The soldered contact was insulated with inert epoxy.

Photoelectrochemical and Solid-State Measurements

All electrochemical and solid-state measurements were performed using a Biologic VMP3 Potentiostat, controlled via EC Lab for Windows. The light intensity was measured using a calibrated Si photodiode (Thorlabs FDS100). A three-port Pyrex glass electrochemical cell with a flat glass window was utilized for all photoelectrochemical depositions and tests.

For electrochemical experiments, a three-electrode configuration was used with an Ir wire counter electrode and a Ag/AgCl (3M NaCl, BASi RE-5B) reference electrode. Working electrodes were p⁺- or n⁺- Si wafer pieces. Unless otherwise stated, most films were deposited until a charge density of -750 mC cm⁻² had been passed. Depending on substrate and other parameters, various applied potentials were used in the deposition of Se-Te films (see Table S1.2). Silicon substrates were etched with BHF for ~20 s and rinsed with H₂O immediately before testing and deposition. The light source used in the deposition of most Se-Te films was a homemade LED apparatus fashioned out of an aluminum printed circuit board (PCB) (Sink Pad II 1939) fastened onto an Al block and cooled by chilled-water at a temperature of 14 °C. Thermal contact was obtained using an interfacial layer of Ag thermal paste (Arctic Silver 5 High-Density Polysynthetic Silver Thermal Compound). Three LEDs (Osram SFH 4725S) were soldered in series to the PCB. The LEDs had an intensity weighted average wavelength of 927 nm, a spectral bandwidth of 37 nm, and were powered by a DC power supply (Hewlett Packard E3611A) in constant current mode at 0.78 A. The

output from the LEDs was passed through a dichroic film linear polarizer (Thorlabs LPNIRE200-B) and collected with an aspheric condenser lens (Edmund Optics, $\text{\O} = 75 \text{ mm}$, $f = 50 \text{ mm}$). A 600 grit diffuser (Thorlabs DG20) was placed in front of the window of the electrochemical cell to produce illumination of uniform intensity incident on the working electrodes. An illumination power density of 53 mW cm^{-2} was used during the photoelectrochemical deposition.

For solid-state, ultraviolet photoemission spectroscopic (UPS), and x-ray photoemission spectroscopic (XPS) measurements, Se-Te films were grown for 10 min using unpolarized $\sim 200 \text{ mW cm}^{-2}$ illumination from a homemade broad-band white light source constructed from a 300 W ELH-type W-halogen bulb with an intensity weighted average wavelength of 640 nm at 120 V. For solid-state measurements, top contact was made by electroplating Ni onto the deposited Se-Te films. For electrodeposited top contacts, Ni films were deposited from a Ni sulfamate solution in a three-electrode configuration with a Ni pellet counter electrode and a Ag/AgCl (1M KCl, CH Instruments, CHI111) reference electrode. Nickel films were deposited potentiostatically for $\sim 2 \text{ h}$ between -0.600 V and -0.800 V vs. Ag/AgCl, depending on the substrate. Nickel is known to make ohmic contact to both Se and Te^{18, 19}. Contact was made to the deposited Ni film with a tinned Cu wire and Ag paint. To determine the current-voltage behavior of the Se-Te – Si junctions, a two-electrode configuration was utilized, with the Si substrate as the working electrode and the electrodeposited Ni top contact as the counter electrode.

Sample Preparation and Image Acquisition

Following electrodeposition, a razor blade was utilized to cut samples from electrode mounts. Samples were then placed in an acetone bath to remove excess nail polish and Ag paint. All samples

were imaged using an FEI Nova NanoSEM 450 with an accelerating voltage of 5 kV. A through-lens (immersion) secondary electron detector was utilized at a working distance of 5 mm. For Fourier analysis, samples were imaged at a magnification of 6250 X and resolution 4096 pixels wide, corresponding to a scale of ~ 85.8 pixels μm^{-1} . Gwyddion (<http://gwyddion.net/>) was used for all image analysis, Fourier Transform analysis and Lorentzian peak fitting. Horizontal and vertical surface profiles were extracted from 2D FT plots with an integration width of 30 pixels. Other images used were obtained at a magnification of 25k X and with a resolution 2048 pixels wide, corresponding to a scale of ~ 171.6 pixels μm^{-1} .

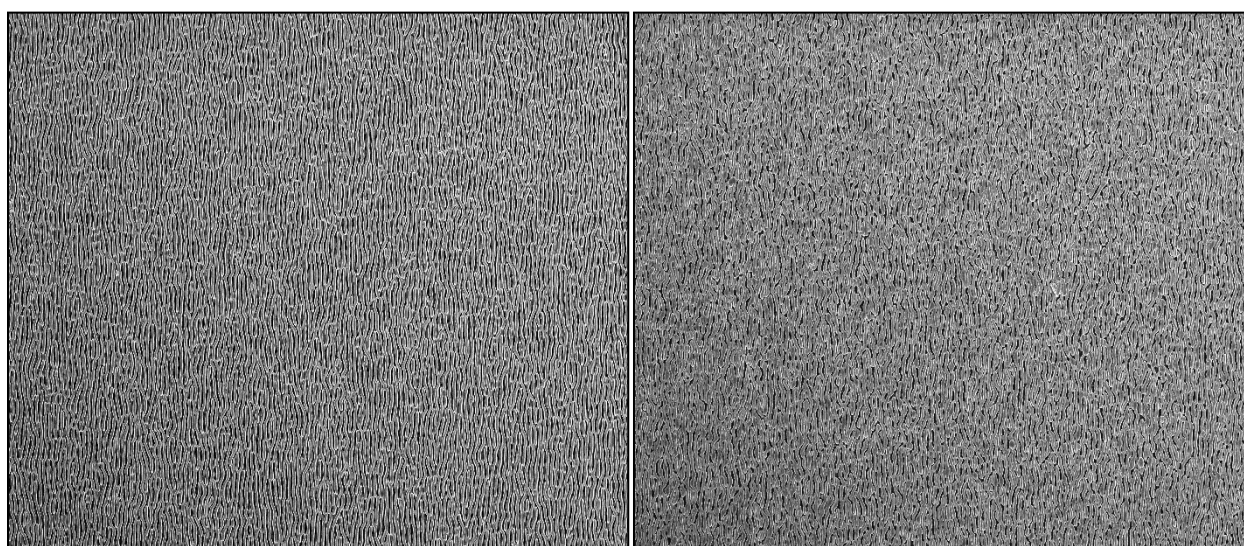
Work Function, Valence Band Position, and Compositional Analysis

Work function, valence band position, and compositional analysis measurements were acquired using a Kratos AXIS Ultra XPS and UPS (Kratos Analytical, Manchester, UK). The x-ray source was the monochromatic Al K α line at 1486.6 eV, with 0.2 eV resolution at full width half maximum. The ultraviolet source was a He I line at 21.22 eV photon energy. XPS and UPS data were analyzed using CasaXPS, CASA Software Ltd. Charge neutralization was not utilized during data acquisition. The XPS instrument was calibrated to the Au 4f_{7/2} peak at 84 eV. Samples were calibrated to the adventitious carbon peak at 284.5 eV. The UPS instrument was calibrated such that the zero binding-energy position was the Fermi edge of freshly sputtered Au.

To measure work functions, the linear portions of the secondary-electron cutoff in the UPS data were extrapolated to the x-intercept positions, as shown by the linear fit lines in Figure S1.3. The x-intercept values were then subtracted from the He I photon energy (21.22 eV) to yield the work function values for the Se-Te films.

For valence-band positions, the linear portions of the low binding-energy regions in the UPS data were extrapolated to the x-intercept positions, as shown by the linear fit lines in Figure S1.3. The x-intercept values were then added to the observed Fermi level/work function values to obtain the valence-band maxima (VBM).

1.4.2 Low-magnification SEM images used for FT analysis in Figure 1.1



10 μm

Figure S1.1. Low-magnification SEM images of photoelectrodeposited Se-Te films grown on (a) $\text{p}^+\text{-Si}$ /Figure 1.1a and b $\text{n}^+\text{-Si}$ /Figure 1.1b used in Fourier analysis in Figure 1.1c-f. SEM images are obtained at a magnification of 6250 X and at a resolution of 4096 pixels wide, corresponding to a scale of 85.8 pixels μm^{-1} .

1.4.3 Additional data gathered for Se-Te films deposited on n⁺-Si and p⁺-Si substrates

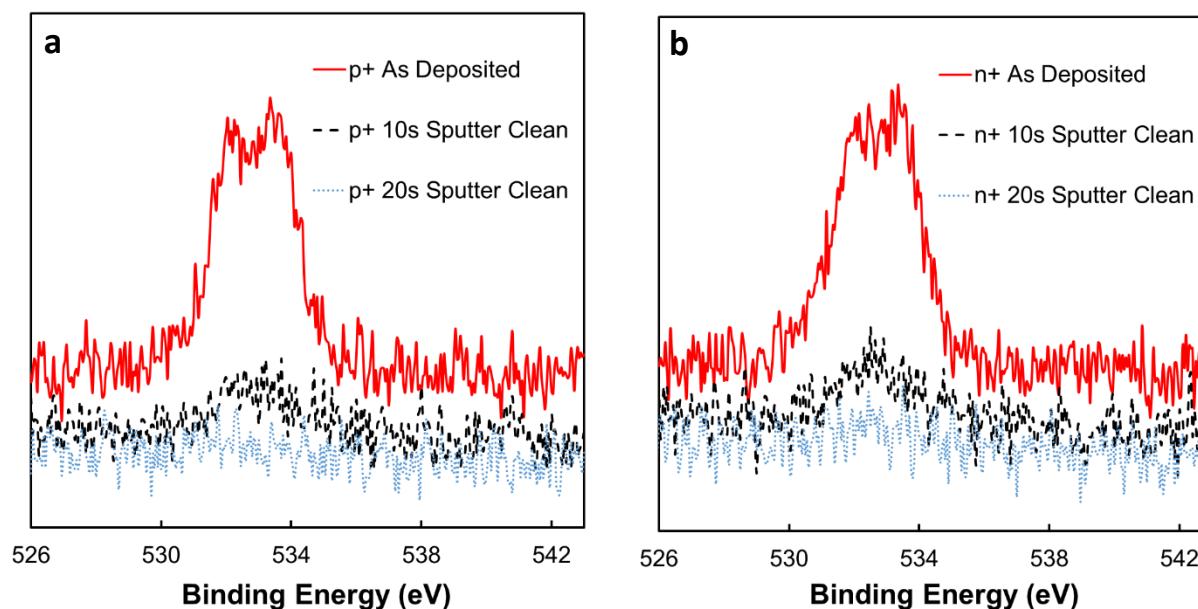


Figure S1.2. XPS data of O 1s (Se-O and Te-O) core-level region for as deposited; 10 s sputter cleaned; and 20 s sputter cleaned Se-Te films on (a) p⁺-Si and (b) n⁺-Si substrates, showing the progressive removal of a surface oxide after sputter cleaning.

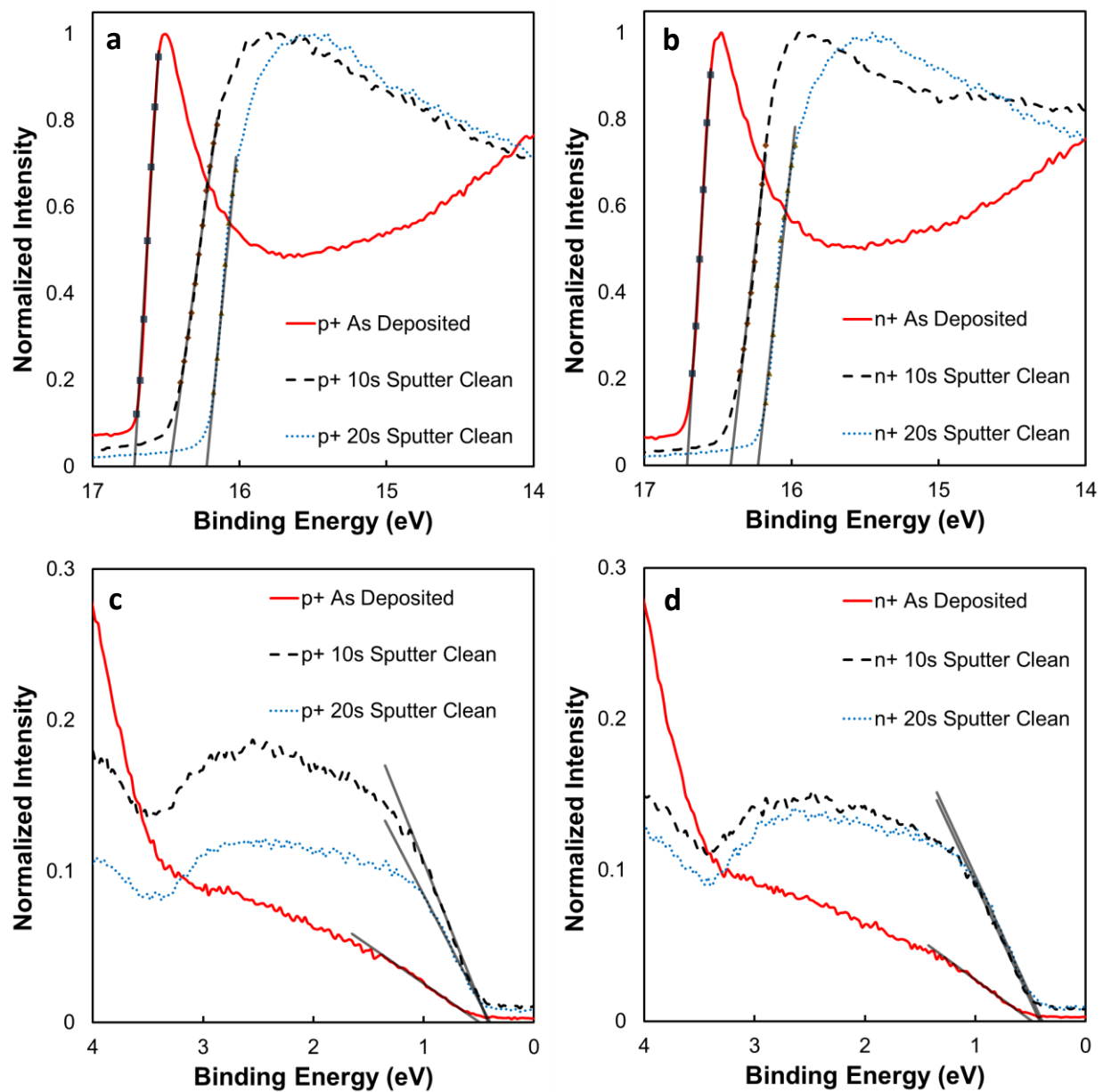


Figure S1.3. Normalized UPS data for as deposited, 10 s sputter cleaned, and 20 s sputter cleaned Se-Te films showing work function and valence band maximum positions on (a), (c) p⁺-Si and (b), (d) n⁺-Si substrates. The spectra show that the work function values shifted to a higher kinetic energy as the surface oxide on Se-Te was gradually removed by sputter cleaning.

Table S1.1. List of Work Function and Valence Band Maxima (VBM) Values Calculated from UPS Spectra

Sample	VBM - E_F (eV)	Work Function (eV)
n+ As Deposited	0.486 ± 0.017	4.51 ± 0.10
n+ 10s Sputter Cleaning	0.416 ± 0.014	4.81 ± 0.15
n+ 20s Sputter Cleaning	0.395 ± 0.015	4.99 ± 0.15
p+ As Deposited	0.488 ± 0.014	4.51 ± 0.09
p+ 10s Sputter Cleaning	0.415 ± 0.017	4.75 ± 0.20
p+ 20s Sputter Cleaning	0.396 ± 0.013	5.00 ± 0.12

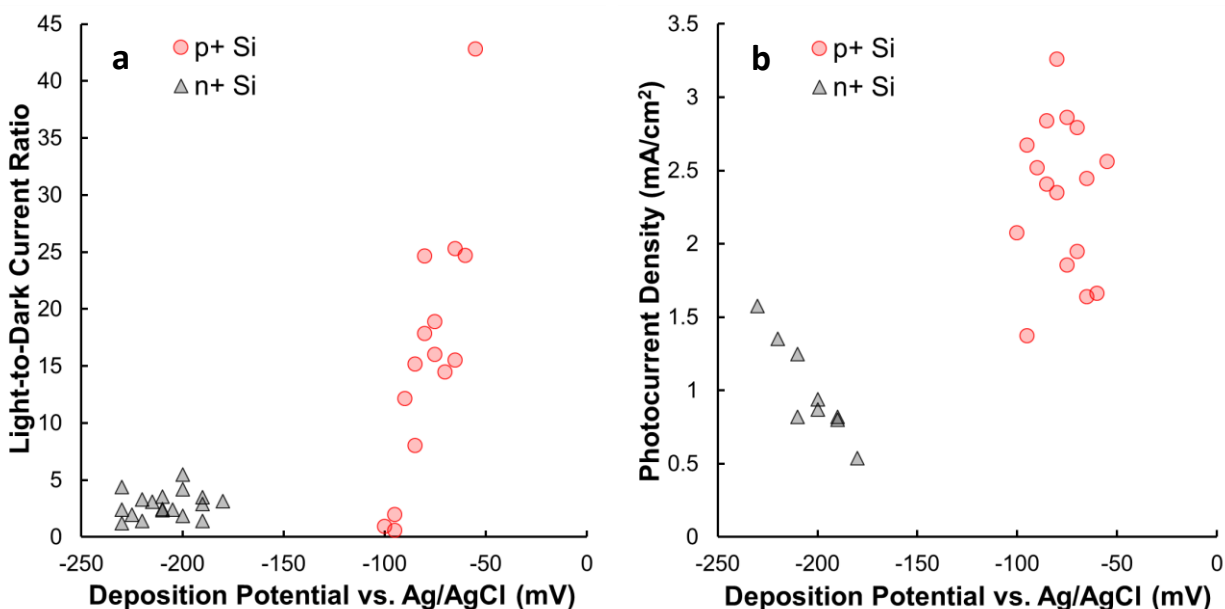


Figure S1.4. Plots showing the relationship between (a) light-to-dark current ratios (measured during chopped light chronoamperometry) and (b) measured peak photocurrent densities vs. the applied potential in the deposition of Se-Te on p⁺-Si and n⁺-Si. At peak current during growth, the light-to-dark current ratios sharply increased at more negative deposition potentials on p⁺-Si, whereas on n⁺-Si these ratios exhibited little to no trend with deposition potential. Peak photocurrent densities showed nearly no relationship to deposition potential for films deposited on p⁺-Si. On n⁺-Si, a stronger trend yielded a higher photocurrent density (and more extracted photocurrent) at more negative deposition potentials. The unchanging (with applied potential) light-to-dark current ratios on n⁺-Si suggest that the photo- and dark-current densities increased concomitantly as films were deposited at more negative potentials. On p⁺-Si, however, photocurrent densities were more stable to changes in applied potential, suggesting no change in extracted photocurrent but rather purely a change in dark current densities as the deposition potential was made more negative. The experiments shown here depict the range of working potentials for which the photoelectrodeposition produced lamellar structures (rather than purely dark growth or no growth) on either substrate. A relatively more negative applied potential is required for phototropic growth to occur on n⁺-Si vs. p⁺-Si.

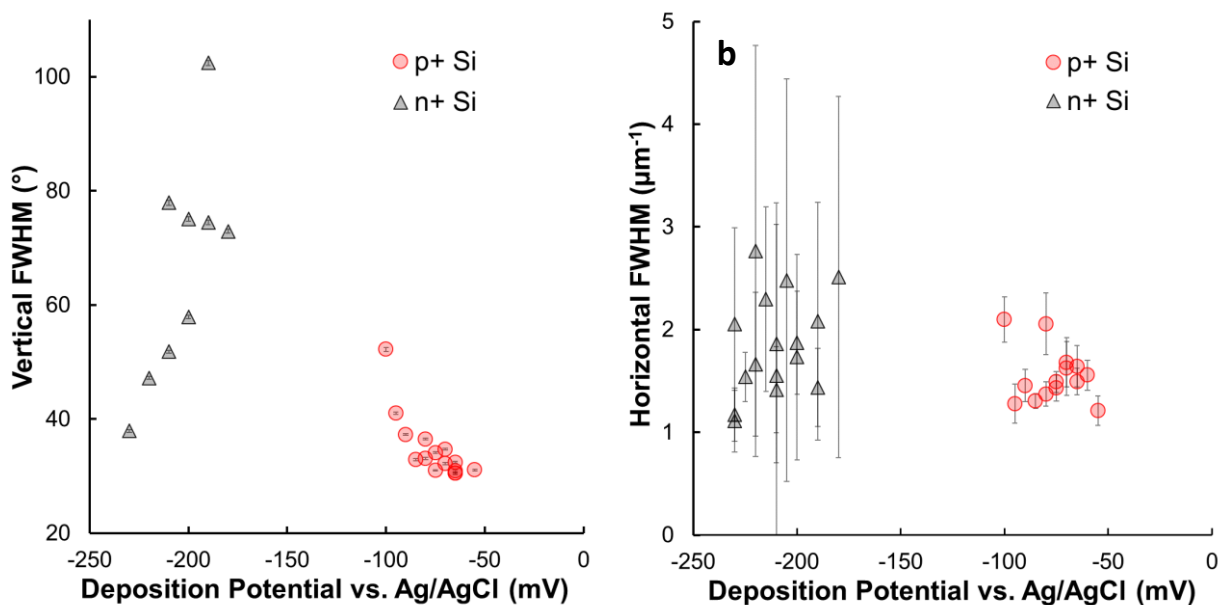


Figure S1.5. Plots showing the relationship between the (a) vertical and (b) horizontal primary peak FWHM in the FT spectra of SEM images of Se-Te films deposited on p⁺-Si or n⁺-Si vs. the potential applied in the deposition of those films. The horizontal FWHM did not track well with deposition potential, due to both a low signal-to-noise ratio and less pattern fidelity information encoded in the horizontal (perpendicular to input polarization) periodicity of the Se-Te film pattern. Conversely, in the vertical direction, the FWHM had a stronger relationship with deposition potential, with different trends observed for films grown on p⁺-Si and n⁺-Si. Straighter patterns were observed when deposition potentials were more positive on p⁺-Si; however, on n⁺-Si, straighter patterns developed with more negative relative applied potentials.

1.4.4 Results and data gathered for Se-Te films deposited on Au and Ti substrates

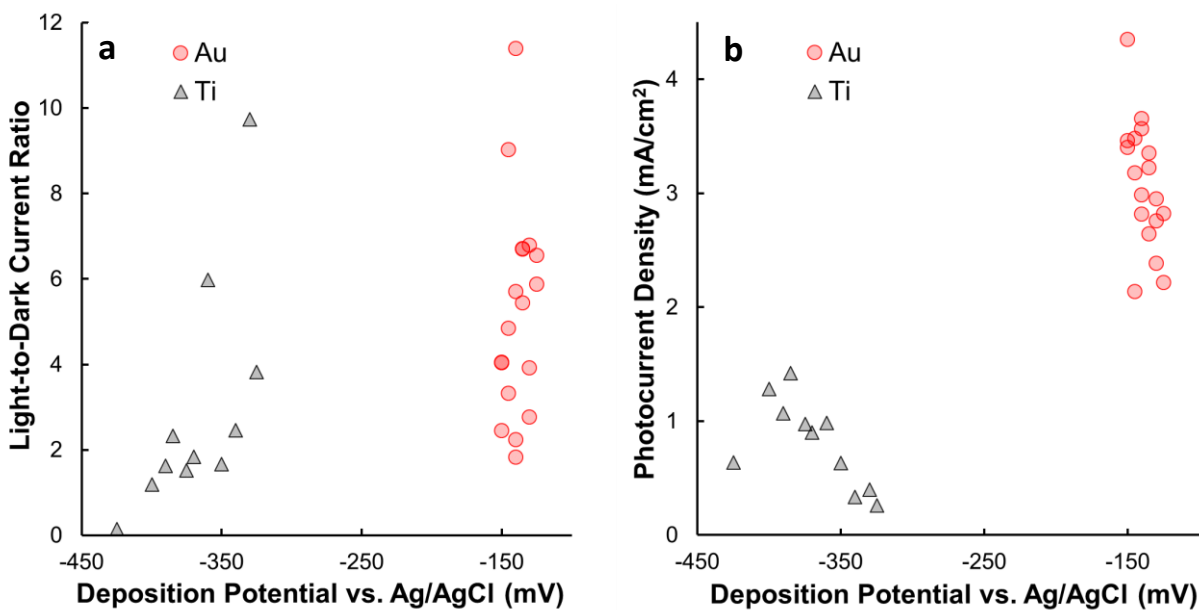


Figure S1.6. Plots showing the relationship between (a) light-to-dark current ratios (measured during chopped light chronoamperometry) and (b) measured peak photocurrent densities vs. the applied potential in the deposition of Se-Te on Au and Ti substrates. Se-Te films deposited on Au substrates generally displayed higher measured light-to-dark current ratios and higher photocurrent densities than were observed for films deposited on Ti substrates.

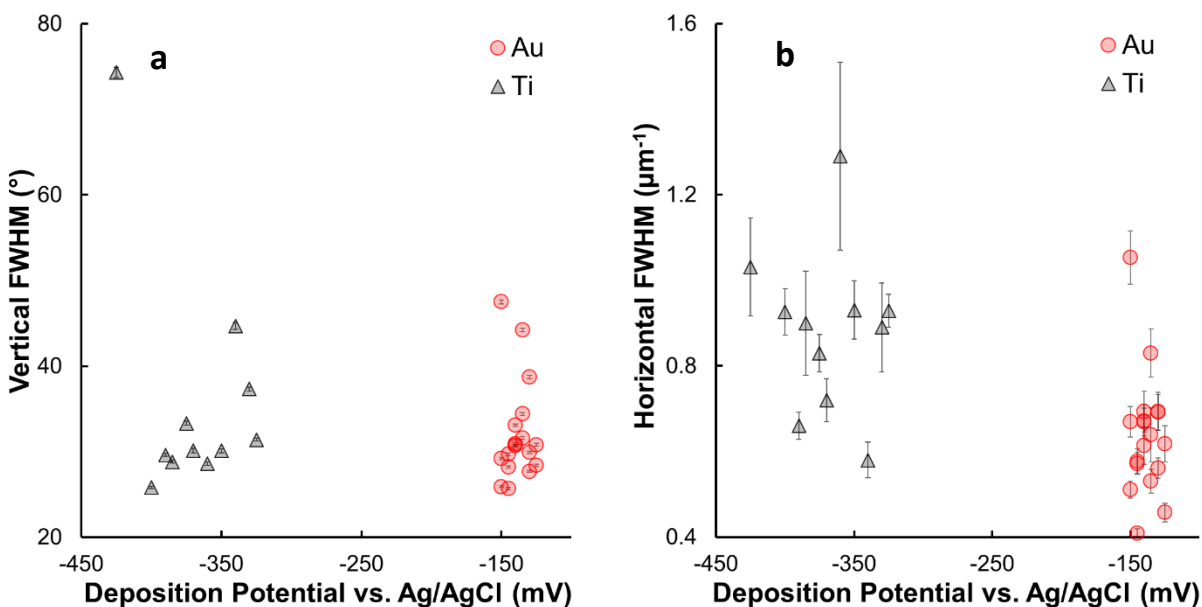


Figure S1.7. Plots showing the relationship between the (a) vertical and (b) horizontal primary peak FWHM in the FT spectra of SEM images of Se-Te films deposited on Au or Ti substrates vs. the potential applied in the deposition of those films. Similar to the results on Si substrates, the horizontal FWHM data was noisier and provided less information on the pattern fidelity of Se-Te films relative to the observed vertical FWHM values. In general, straighter and higher fidelity patterns were observed in Se-Te films deposited on Au vs. Ti substrates.

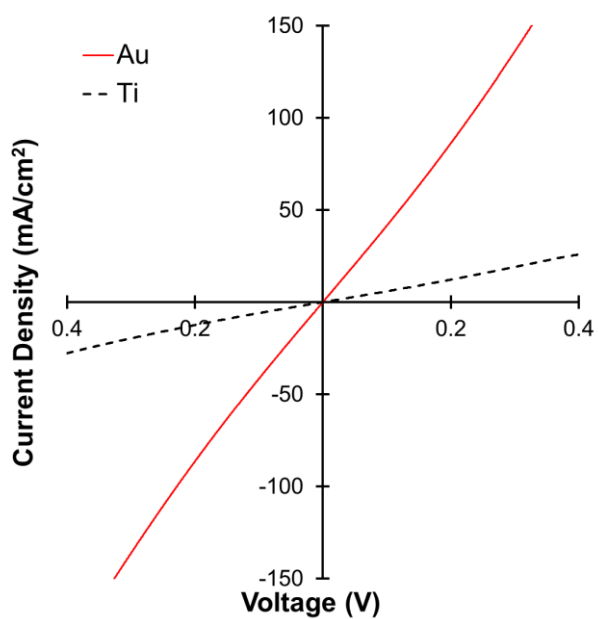


Figure S1.8. Current-voltage behavior of Se-Te on Au and Ti. As expected, better electrical contact and lower contact resistance was observed between Se-Te and Au, due to the closer work function alignment of Se-Te to Au relative to Ti.

1.4.5 Low-magnification SEM images of Se-Te films on p⁺-Si in Figure 1.5

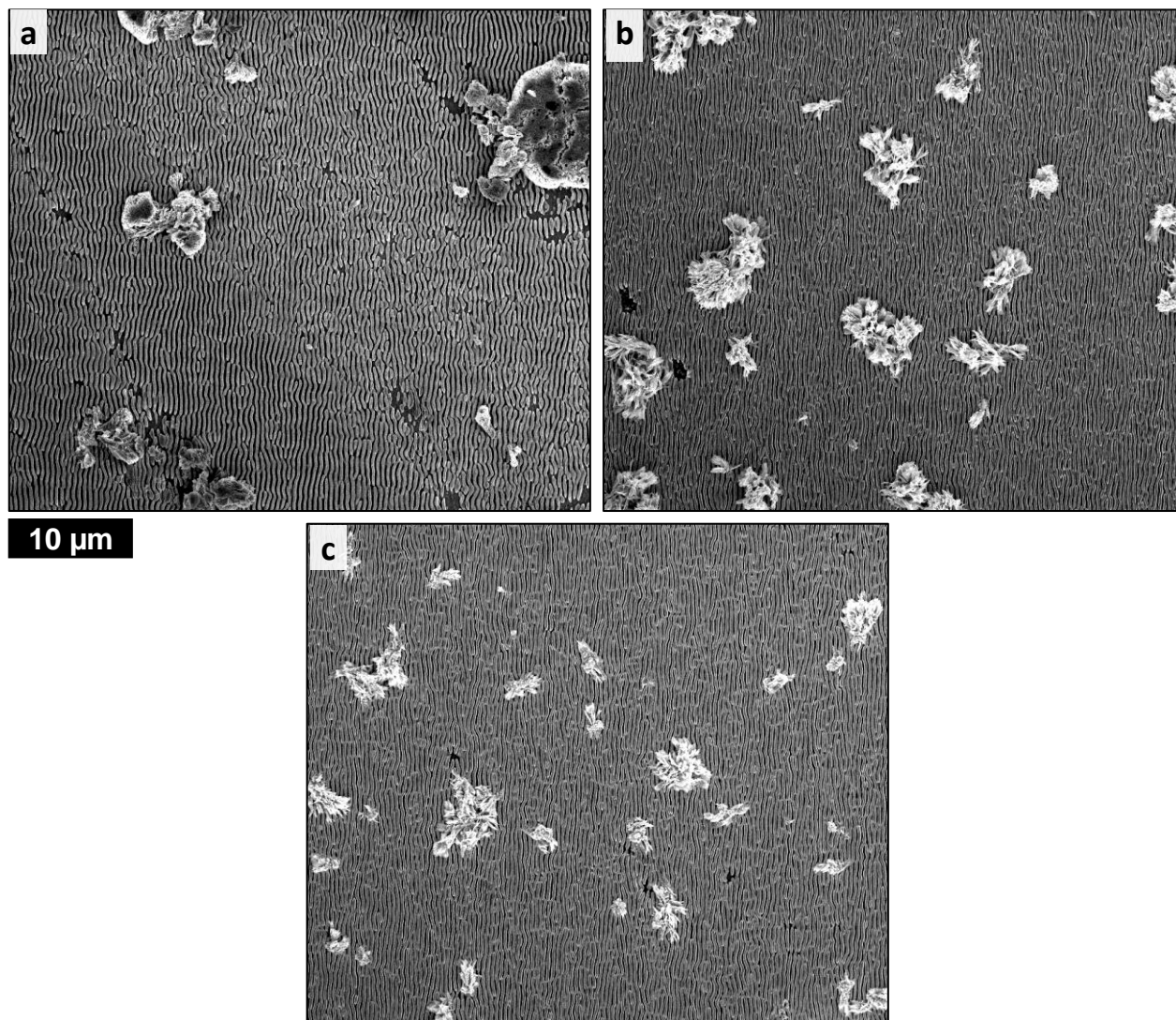


Figure S1.9. Low-magnification SEM images of photoelectrodeposited Se-Te films grown on p⁺-Si from (a) Figure 1.5a, (b) Figure 1.5c, and (c) Figure 1.5e, showing dark spherulitic/dendritic growth. The dark growth appearing on these films was unavoidable at the dark current densities and more negative applied potentials necessary to match the dark deposition rates on n⁺-Si in Figure 1.5b, d, and f.

1.4.6 Nucleation density and growth substrate discussions

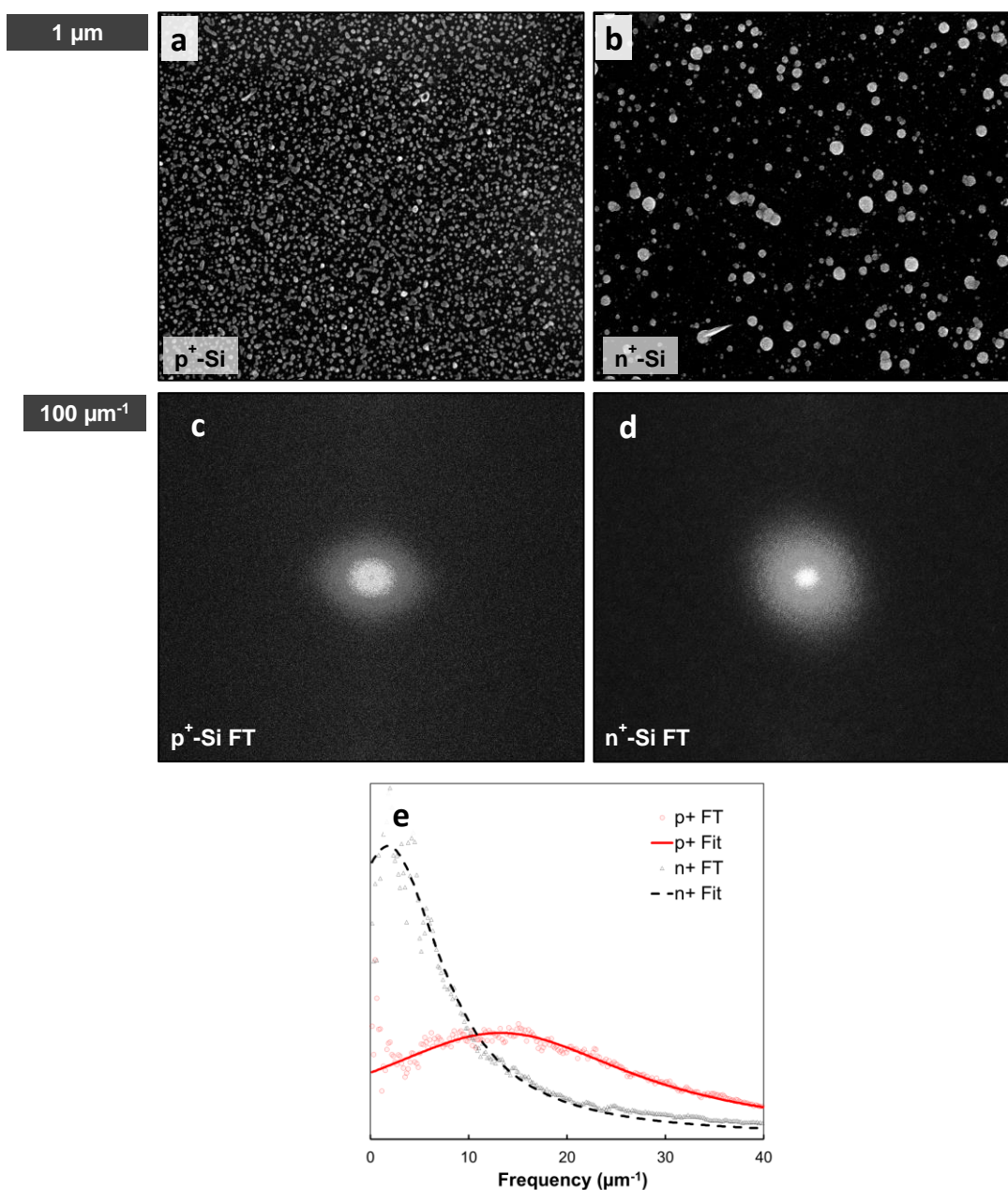


Figure S1.10. Nucleated Se-Te films deposited on (a) p⁺-Si and (b) n⁺-Si at a charge passed of -3.75 mC cm⁻². 2D FT of the images on (c) p⁺-Si and (d) n⁺-Si in (a) and (b), respectively. (e) Comparison of surface profile plots integrated radially over the FT spectra showing larger average particle-to-particle spacing for n⁺-Si vs. p⁺-Si. Isotropic peak shapes at this early level of deposition indicate random nucleation on both substrates. Although random, the peak positions in (e) are at $13.2 \pm 0.05 \mu\text{m}^{-1}$ and $1.8 \pm 0.07 \mu\text{m}^{-1}$ for p⁺-Si and n⁺-Si, respectively, confirming the higher nucleation density observed on p⁺-Si vs. n⁺-Si. Random nucleation of Se-Te is hypothesized to be a required

morphological precursor to the optical scattering effect that produces lamellar features in the photoelectrodeposit.^{1, 2, 7-9} The morphology of phototropically grown Se-Te alloys is similar on a variety of substrates, as shown by past work primarily on either n⁺-Si or Au. However, certain effects, such as nucleation density, depend in detail quantitatively on the characteristics of the substrate, as seen in the variation between (a) and (b). The nucleation behavior also has implications for the pattern period and fidelity, implying quantitative differences between the phototropic film growth morphology on chemically different substrates as well as on substrates that only have mutually different electronic properties, such as doping density, as demonstrated herein.

1.4.7 Table with additional information for all samples fabricated

Table S1.2. List of Photoelectrochemical Details for All Samples Fabricated.

Figure ID	Sample ID	Substrate	Applied Potential (mV vs. Ag/AgCl)	Horizontal FWHM (μm^{-1})	Vertical FWHM ($^{\circ}$)	Vertical FWHM (μm^{-1})	Peak Current Density (mA cm^{-2})	Light-to-Dark Current Ratio	Charge Passed (mC cm^{-2})	Illumination Power (mW cm^{-2})	Deposition Time (s)
<i>Fl.1, Fl.3, Sl.1, Sl.4, Sl.5</i>	138-4	p ⁺	-65	1.49 ± 0.13	30.9 ± 0.16	1.51 ± 0.008	-2.54	25.30	-750	53	-
<i>Fl.1, Fl.2, Fl.3, Sl.1, Sl.4, Sl.5</i>	140-9	n ⁺	-200	1.77 ± 1.00	57.9 ± 0.31	2.74 ± 0.015	-2.36	4.03	-750	53	-
<i>Fl.2</i>	143-3	p ⁺	-65	-	-	-	-	-	-0.75	53	-
<i>Fl.2, Sl.10</i>	143-2	p ⁺	-65	-	-	-	-	-	-3.75	53	-
<i>Fl.2</i>	143-4	p ⁺	-65	-	-	-	-	-	-37.5	53	-
<i>Fl.2</i>	143-5	p ⁺	-65	-	-	-	-	-	-75	53	-
<i>Fl.2, Sl.4, Sl.5</i>	142-10	p ⁺	-65	1.06 ± 0.08	30.5 ± 0.16	1.52 ± 0.008	-1.54	24.62	-750	53	-
<i>F2</i>	140-6	n ⁺	-200	-	-	-	-	-	-0.75	53	-
<i>F2, Sl.10</i>	140-7	n ⁺	-200	-	-	-	-	-	-3.75	53	-
<i>Fl.2</i>	144-1	n ⁺	-200	-	-	-	-	-	-37.5	53	-
<i>Fl.2</i>	144-2	n ⁺	-200	-	-	-	-	-	-75	53	-
<i>Fl.3</i>	-	p ⁺	-200	-	-	-	-	-	-	200	600
<i>Fl.3</i>	-	n ⁺	-200	-	-	-	-	-	-	200	600
<i>Fl.5, Sl.9</i>	148-5	p ⁺	-90	0.59 ± 0.03	33.7 ± 0.17	1.42 ± 0.007	-0.52	2.22	-750	16.56	-
<i>Fl.5, Sl.9</i>	148-9	p ⁺	-94	1.10 ± 0.07	30.1 ± 0.15	1.44 ± 0.007	-0.69	2.74	-750	14.91	-
<i>Fl.5, Sl.9</i>	142-3	p ⁺	-85	1.00 ± 0.08	31.4 ± 0.18	1.53 ± 0.009	-1.03	3.91	-750	20.88	-
<i>Fl.5, Sl.4, Sl.5</i>	137-8	n ⁺	-205	2.48 ± 1.96	104.2 ± 0.57	5.86 ± 0.032	-0.52	2.41	-750	53	-
<i>Fl.5, Sl.4, Sl.5</i>	139-6	n ⁺	-180	2.51 ± 1.76	72.9 ± 0.35	3.53 ± 0.017	-0.71	3.17	-750	53	-
<i>Fl.5, Sl.4, Sl.5</i>	139-1	n ⁺	-200	1.73 ± 1.00	57.3 ± 0.30	2.54 ± 0.013	-1.08	4.21	-750	53	-
<i>Sl.4, Sl.5</i>	136-3	p ⁺	-100	2.10 ± 0.22	52.2 ± 0.34	3.10 ± 0.020	-4.33	0.92	-750	53	-
<i>Sl.4, Sl.5</i>	136-4	p ⁺	-75	1.49 ± 0.10	31.0 ± 0.13	1.71 ± 0.007	-1.97	15.98	-750	53	-
<i>Sl.4, Sl.5</i>	136-5	p ⁺	-85	1.30 ± 0.07	32.9 ± 0.17	1.82 ± 0.009	-2.57	15.15	-750	53	-
<i>Sl.4, Sl.5</i>	136-6	p ⁺	-95	1.28 ± 0.19	41.0 ± 0.21	2.49 ± 0.013	-3.83	0.56	-750	53	-
<i>Sl.4, Sl.5</i>	136-7	p ⁺	-65	1.64 ± 0.20	32.4 ± 0.14	1.78 ± 0.008	-1.74	15.52	-750	53	-
<i>Sl.4, Sl.5</i>	136-8	p ⁺	-70	1.62 ± 0.26	34.7 ± 0.16	1.91 ± 0.009	-2.08	14.46	-750	53	-
<i>Sl.4, Sl.5</i>	136-9	p ⁺	-80	1.37 ± 0.12	33.1 ± 0.17	1.87 ± 0.010	-2.48	17.86	-750	53	-
<i>Sl.4, Sl.5</i>	136-10	p ⁺	-90	1.45 ± 0.16	37.3 ± 0.19	2.09 ± 0.011	-2.73	12.14	-750	53	-
<i>Sl.4, Sl.5</i>	138-2	p ⁺	-75	1.43 ± 0.13	34.1 ± 0.15	1.72 ± 0.008	-3.01	18.88	-750	53	-
<i>Sl.4</i>	138-5	p ⁺	-85	-	-	-	-3.19	7.99	-750	53	-

<i>Sl.4, Sl.5</i>	138-6	p ⁺	-70	1.68 ± 0.24	32.2 ± 0.17	1.67 ± 0.009	-2.83	77.47	-750	53	-
<i>Sl.4, Sl.5</i>	138-7	p ⁺	-80	2.06 ± 0.30	36.5 ± 0.18	2.03 ± 0.010	-3.39	24.64	-750	53	-
<i>Sl.4, Sl.5</i>	138-8	p ⁺	-60	1.56 ± 0.15	30.5 ± 0.14	1.55 ± 0.007	-1.73	24.69	-750	53	-
<i>Sl.4</i>	138-9	p ⁺	-95	-	-	-	-4.05	1.94	-750	53	-
<i>Sl.4, Sl.5</i>	138-10	p ⁺	-55	1.21 ± 0.14	31.1 ± 0.15	1.82 ± 0.009	-2.62	42.79	-750	53	-
<i>Sl.4</i>	137-1	n ⁺	-200	-	-	5.66 ± 0.030	-0.82	5.47	-750	53	-
<i>Sl.4</i>	137-2	n ⁺	-190	-	-	-	-0.70	3.52	-750	53	-
<i>Sl.4, Sl.5</i>	137-3	n ⁺	-210	1.55 ± 1.68	83.5 ± 0.44	4.53 ± 0.024	-0.88	3.57	-750	53	-
<i>Sl.4, Sl.5</i>	137-4	n ⁺	-220	2.76 ± 2.00	114.8 ± 0.64	5.70 ± 0.032	-0.97	3.30	-750	53	-
<i>Sl.4, Sl.5</i>	137-5	n ⁺	-230	2.05 ± 0.94	62.9 ± 0.37	3.19 ± 0.019	-1.81	1.20	-750	53	-
<i>Sl.4, Sl.5</i>	137-6	n ⁺	-230	1.11 ± 0.30	60.9 ± 0.27	2.81 ± 0.013	-0.94	4.39	-750	53	-
<i>Sl.4, Sl.5</i>	137-7	n ⁺	-215	2.30 ± 0.90	104.9 ± 0.49	5.61 ± 0.026	-0.48	3.10	-750	53	-
<i>Sl.4, Sl.5</i>	137-10	n ⁺	-225	1.54 ± 0.24	57.2 ± 0.30	2.82 ± 0.015	-1.16	1.96	-750	53	-
<i>Sl.4, Sl.5</i>	139-2	n ⁺	-190	1.44 ± 0.38	74.5 ± 0.40	3.50 ± 0.019	-1.40	1.40	-750	53	-
<i>Sl.4, Sl.5</i>	139-3	n ⁺	-210	1.41 ± 0.42	77.9 ± 0.42	3.29 ± 0.018	-1.15	2.46	-750	53	-
<i>Sl.4, Sl.5</i>	139-4	n ⁺	-220	1.66 ± 0.70	47.2 ± 0.23	2.18 ± 0.011	-2.30	1.42	-750	53	-
<i>Sl.4, Sl.5</i>	139-5	n ⁺	-230	1.17 ± 0.26	37.9 ± 0.20	1.70 ± 0.009	-2.24	2.39	-750	53	-
<i>Sl.4, Sl.5</i>	139-8	n ⁺	-210	1.86 ± 1.16	51.8 ± 0.23	2.46 ± 0.011	-1.78	2.34	-750	53	-
<i>Sl.4, Sl.5</i>	139-9	n ⁺	-190	2.08 ± 1.16	102.4 ± 0.48	5.15 ± 0.024	-1.08	2.90	-750	53	-
<i>Sl.4, Sl.5</i>	139-10	n ⁺	-200	1.87 ± 0.50	75.1 ± 0.40	3.64 ± 0.019	-1.45	1.85	-750	53	-
<i>Sl.2, Sl.3, Table Sl.1</i>	82-1	p ⁺	-200	-	-	-	-	-	-	200	600
<i>Sl.2, Sl.3, Table Sl.1</i>	82-4	n ⁺	-200	-	-	-	-	-	-	200	600
<i>Sl.6, Sl.7</i>	160-6	Au	-135	0.64 ± 0.06	34.4 ± 0.16	1.53 ± 0.007	-2.64	5.43	-750	53	-
<i>Sl.6, Sl.7</i>	160-7	Au	-130	0.56 ± 0.02	27.7 ± 0.13	1.24 ± 0.006	-2.38	2.76	-750	53	-
<i>Sl.6, Sl.7</i>	160-8	Au	-150	0.67 ± 0.04	29.2 ± 0.14	1.30 ± 0.006	-3.46	4.03	-750	53	-
<i>Sl.6, Sl.7</i>	161-1	Ti	-350	0.93 ± 0.07	30.1 ± 0.25	1.60 ± 0.013	-1.01	1.67	-750	53	-
<i>Sl.6, Sl.7</i>	161-2	Ti	-375	0.83 ± 0.04	33.3 ± 0.24	1.78 ± 0.013	-1.62	1.51	-750	53	-
<i>Sl.6, Sl.7</i>	161-3	Ti	-400	0.93 ± 0.05	25.8 ± 0.13	1.42 ± 0.007	-2.36	1.19	-750	53	-
<i>Sl.6, Sl.7</i>	161-4	Ti	-425	1.03 ± 0.11	74.3 ± 0.59	4.57 ± 0.036	-4.91	0.15	-750	53	-
<i>Sl.6, Sl.7</i>	161-5	Ti	-325	0.93 ± 0.04	31.4 ± 0.16	1.67 ± 0.008	-0.33	3.82	-750	53	-
<i>Sl.6, Sl.7</i>	161-6	Au	-145	0.57 ± 0.03	28.2 ± 0.11	1.23 ± 0.005	-3.18	4.84	-750	53	-
<i>Sl.6, Sl.7</i>	161-7	Au	-140	0.67 ± 0.03	30.9 ± 0.16	1.39 ± 0.007	-3.57	5.71	-750	53	-
<i>Sl.6, Sl.7</i>	161-8	Au	-135	0.83 ± 0.06	44.2 ± 0.22	2.01 ± 0.010	-3.22	6.69	-750	53	-
<i>Sl.6, Sl.7</i>	161-9	Au	-130	0.69 ± 0.04	38.7 ± 0.20	1.72 ± 0.009	-2.75	6.78	-750	53	-

<i>Sl.6, Sl.7</i>	<i>161-10</i>	Au	-125	0.46 ± 0.02	30.8 ± 0.15	1.36 ± 0.007	-2.21	6.55	-750	53	-
<i>Sl.6, Sl.7</i>	<i>159-1</i>	Au	-150	1.05 ± 0.06	47.5 ± 0.24	2.12 ± 0.011	-3.40	4.04	-750	53	-
<i>Sl.6, Sl.7</i>	<i>159-2</i>	Au	-145	0.41 ± 0.01	25.7 ± 0.12	1.10 ± 0.005	-2.14	9.02	-750	53	-
<i>Sl.6, Sl.7</i>	<i>159-3</i>	Au	-140	0.61 ± 0.04	33.1 ± 0.15	1.42 ± 0.007	-2.82	11.39	-750	53	-
<i>Sl.6, Sl.7</i>	<i>162-1</i>	Au	-150	0.51 ± 0.02	25.9 ± 0.12	1.15 ± 0.005	-4.35	2.45	-750	53	-
<i>Sl.6, Sl.7</i>	<i>162-2</i>	Au	-145	0.58 ± 0.03	29.7 ± 0.16	1.32 ± 0.007	-3.48	3.32	-750	53	-
<i>Sl.6, Sl.7</i>	<i>162-3</i>	Au	-140	0.69 ± 0.05	30.7 ± 0.14	1.38 ± 0.006	-3.66	1.82	-750	53	-
<i>Sl.6, Sl.7</i>	<i>162-4</i>	Au	-135	0.53 ± 0.03	31.6 ± 0.16	1.53 ± 0.008	-3.35	6.71	-750	53	-
<i>Sl.6, Sl.7</i>	<i>162-5</i>	Au	-130	0.69 ± 0.04	29.9 ± 0.15	1.34 ± 0.007	-2.95	3.91	-750	53	-
<i>Sl.6, Sl.7</i>	<i>162-6</i>	Au	-125	0.62 ± 0.04	28.4 ± 0.13	1.27 ± 0.006	-2.82	5.87	-750	53	-
<i>Sl.6, Sl.7</i>	<i>162-7</i>	Au	-140	0.67 ± 0.04	30.7 ± 0.15	1.38 ± 0.007	-2.98	2.24	-750	53	-
<i>Sl.6, Sl.7</i>	<i>163-2</i>	Ti	-360	1.29 ± 0.22	28.6 ± 0.19	1.39 ± 0.009	-1.15	5.98	-750	53	-
<i>Sl.6, Sl.7</i>	<i>163-3</i>	Ti	-385	0.90 ± 0.12	28.8 ± 0.16	1.53 ± 0.009	-2.03	2.33	-750	53	-
<i>Sl.6, Sl.7</i>	<i>163-6</i>	Ti	-330	0.89 ± 0.10	37.3 ± 0.22	1.74 ± 0.010	-0.44	9.74	-750	53	-
<i>Sl.6, Sl.7</i>	<i>163-8</i>	Ti	-340	0.58 ± 0.04	44.7 ± 0.40	2.24 ± 0.020	-0.47	2.46	-750	53	-
<i>Sl.6, Sl.7</i>	<i>163-9</i>	Ti	-370	0.72 ± 0.05	30.1 ± 0.25	1.59 ± 0.013	-1.39	1.84	-750	53	-
<i>Sl.6, Sl.7</i>	<i>163-10</i>	Ti	-390	0.66 ± 0.03	29.6 ± 0.16	1.55 ± 0.008	-1.73	1.62	-750	53	-

1.5 References

1. Sadtler, B.; Burgos, S. P.; Batara, N. A.; Beardslee, J. A.; Atwater, H. A.; Lewis, N. S., Phototropic growth control of nanoscale pattern formation in photoelectrodeposited Se-Te films. *Proc Natl Acad Sci U S A* **2013**, *110* (49), 19707-12.
2. Carim, A. I.; Batara, N. A.; Premkumar, A.; Atwater, H. A.; Lewis, N. S., Self-Optimizing Photoelectrochemical Growth of Nanopatterned Se-Te Films in Response to the Spectral Distribution of Incident Illumination. *Nano Lett* **2015**, *15* (10), 7071-7076.
3. Bhatnagar, A. K.; Srivastava, V.; Reddy, K. V., Te substitution in disordered dilute Se_{1-x}Te_x alloys. *Appl Phys Lett* **1998**, *73* (17), 2426-2428.
4. Reddy, K. V.; Bhatnagar, A. K., Electrical and optical studies on amorphous Se-Te alloys. *J Phys D Appl Phys* **1992**, *25* (12), 1810-1816.
5. Beyer, W.; Mell, H.; Stuke, J., Conductivity and thermoelectric power of trigonal Se₆Te_{1-x} single crystals. *phys status solidi (b)* **1971**, *45* (1), 153-162.
6. El-Korashy, A.; El-Zahed, H.; Zayed, H. A.; Kenawy, M. A., Effect of composition and structure on electrical conduction of Se(100-x)Te(x) films. *Solid State Commun* **1995**, *95* (5), 335-339.
7. Carim, A. I.; Hamann, K. R.; Batara, N. A.; Thompson, J. R.; Atwater, H. A.; Lewis, N. S., Template-free synthesis of periodic three-dimensional PbSe nanostructures via photoelectrodeposition. *J Am Chem Soc* **2018**, *140* (21), 6536-6539.
8. Carim, A. I.; Batara, N. A.; Premkumar, A.; Atwater, H. A.; Lewis, N. S., Polarization Control of Morphological Pattern Orientation During Light-Mediated Synthesis of Nanostructured Se-Te Films. *ACS Nano* **2016**, *10* (1), 102-11.
9. Carim, A. I.; Batara, N. A.; Premkumar, A.; May, R.; Atwater, H. A.; Lewis, N. S., Morphological Expression of the Coherence and Relative Phase of Optical Inputs to the Photoelectrodeposition of Nanopatterned Se-Te Films. *Nano Lett* **2016**, *16* (5), 2963-8.
10. Matthias, S.; Müller, F.; Jamois, C.; Wehrspohn, R. B.; Gösele, U., Large-Area Three-Dimensional Structuring by Electrochemical Etching and Lithography. *Adv Mater* **2004**, *16* (23-24), 2166-2170.
11. Lévy-Clément, C., Morphology of Porous n-Type Silicon Obtained by Photoelectrochemical Etching. *J Electrochem Soc* **1994**, *141* (4), 958.
12. Lehmann, V., Formation Mechanism and Properties of Electrochemically Etched Trenches in n-Type Silicon. *J Electrochem Soc* **1990**, *137* (2), 653.
13. Ogata, Y.; Kobayashi, K.; Motoyama, M., Electrochemical metal deposition on silicon. *Curr Opin Solid St M* **2006**, *10* (3-4), 163-172.
14. Dasog, M.; Carim, A. I.; Yalamanchili, S.; Atwater, H. A.; Lewis, N. S., Profiling Photoinduced Carrier Generation in Semiconductor Microwire Arrays via Photoelectrochemical Metal Deposition. *Nano Lett* **2016**, *16* (8), 5015-21.

15. Zhang, Z.; Yates, J. T., Jr., Band bending in semiconductors: chemical and physical consequences at surfaces and interfaces. *Chem Rev* **2012**, *112* (10), 5520-51.
16. Novikov, A., Experimental measurement of work function in doped silicon surfaces. *Solid-State Electronics* **2010**, *54* (1), 8-13.
17. Skriver, H. L.; Rosengard, N. M., Surface energy and work function of elemental metals. *Physical Review B* **1992**, *46* (11), 7157-7168.
18. Okuyama, K.; Tshako, J.; Kumagai, Y., Behavior of metal contacts to evaporated tellurium films. *Thin Solid Films* 1975, *30* (1), 119-126.
19. Lanyon, H. P. D.; Krambeck, R. M., Trapping Levels in Hexagonal Selenium. In *The Physics of Selenium and Tellurium*, 1st ed.; Cooper, W. C., Ed. Pergamon Press: 1969; pp 59-68.

CHAPTER II

Increased Spatial Randomness and Disorder of Nucleates in Dark-Phase Electrodeposition Lead to Increased Spatial Order and Pattern Fidelity in Phototropically Grown Se-Te Electrodeposits

Simonoff, E.; Van Munoz, L. X.; Lewis, N. S., Increased spatial randomness and disorder of nucleates in dark-phase electrodeposition lead to increased spatial order and pattern fidelity in phototropically grown Se-Te electrodeposits. *Nanoscale* 2020, 12 (44), 22478-22486. doi: 10.1039/d0nr07617a

2.1 Introduction

In conventional methods for surface patterning and 3-D morphology control, including optical lithography, holography, or direct write methods, the spatial fidelity of the resulting pattern is directly related to the spatial order and fidelity of the stimulus. For example, in optical lithography, dither of the optical beam or imprecise spatial definition in the edges of a mask deleteriously affect the fidelity of the resulting surface pattern.¹⁻⁵ Similarly, in direct write methods or scanning probe lithographic methods, vibrations of the tip introduce spatial disorder and reduce the fidelity of the resulting material or surface film.⁶⁻⁸ Spatial chemical disorder due to defects or impurities also may deleteriously affect the spatial fidelity of self-assembled, optically patterned, or electrodeposited surface films.⁹⁻¹³ We have recently described the phenomenon of inorganic phototropic growth, in which full 3-D control over the morphology of an electrodeposited film can be obtained by stimulating photoelectrodeposition of materials including PbSe and Se-Te alloys with an uncorrelated, unpatterned, low-intensity light beam, from an optically isotropic solution onto an optically isotropic electrode substrate.¹⁴⁻¹⁸ The growth process initially involves a dark film electrodeposition phase followed by an optically stimulated photoelectrodeposition phase, in which

intrinsic near-field optical scattering in the growing material shapes the internal optical field and, in an emergent property of the material, produces a dynamic feedback with the stimulating light beam that produces long-range order in the resulting electrode film structure. We show here that in inorganic phototropic growth, randomness in the initial electrodeposit is a prerequisite for — and directly leads to — high fidelity and spatial order in the resulting phototropically grown material.

2.2 Results and Discussion

A detailed experimental procedure is provided in the Supporting Information. Se-Te films were deposited potentiostatically from an aqueous solution containing 20 mM SeO₂, 10 mM TeO₂, and 1 M H₂SO₄. Samples were illuminated with vertically polarized light from a narrow-band light-emitting diode (LED) with an intensity-weighted-average wavelength of 927 nm and a power density of 53 mW cm⁻². Substrates were crystalline (111)-oriented Si with a miscut angle $\pm 0.5^\circ$, doped degenerately with either p- or n-type dopants, and the resistivities for both substrates were $< 0.005 \Omega\text{-cm}$.

Figure 2.1 shows scanning-electron-microscope (SEM) images of Se-Te deposits on p⁺-Si and n⁺-Si substrates during the nucleation phase of phototropic growth, i.e., after a charge density of -3.75 mC cm⁻² had been passed, corresponding to equivalent amounts of mass deposited for each sample. Images are shown for Se-Te deposited at two different applied potentials for each substrate; these applied deposition potentials correspond to representative conditions at the positive (Figure 2.1a and c) and negative (Figure 2.1b and d) extremes of the working potential range for phototropic Se-Te growth on each substrate. The insets to the panels in Figure 2.1 show 2D FTs of the respective SEM images. Large-area ($\sim 2000 \mu\text{m}^2$) images of the deposits on n⁺-Si are provided in Figure S2.1.

SEM images and analysis of reproducibility in phototropic films are provided in Figure S2.3.

Films deposited on p^+ -Si (Figure 2.1a and b) exhibited smaller nucleate spacings than films deposited on n^+ -Si (Figure 2.1c and d). For both substrates, the more negative applied potential resulted in smaller nucleate spacings when all other parameters were kept constant.

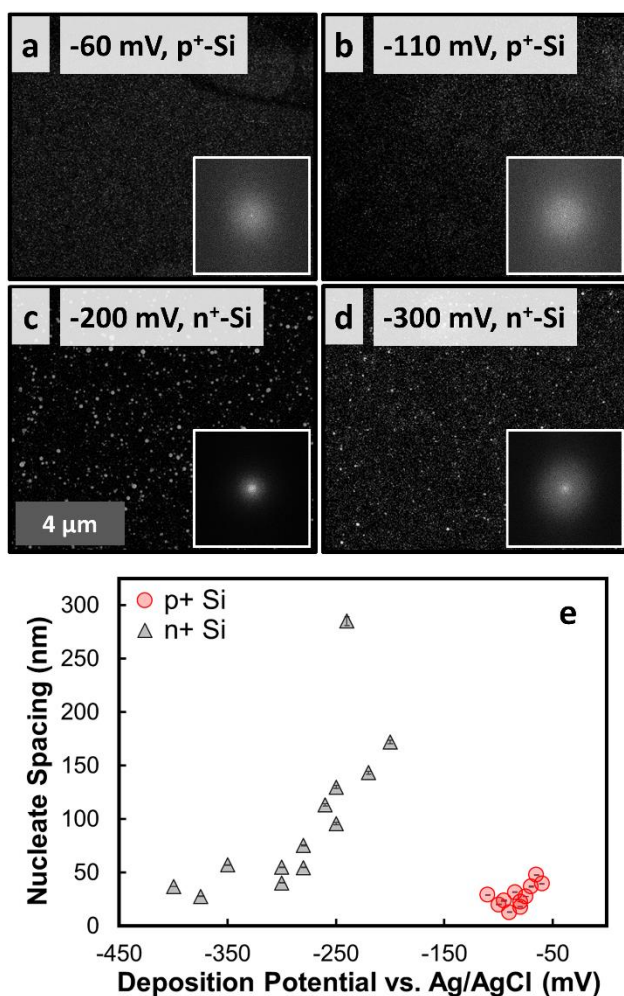


Figure 2.1. SEM images of Se-Te photoelectrodeposited at two different applied potentials on (a, b) p^+ -Si and (c, d) n^+ -Si. During the deposition, the substrates were illuminated by vertically polarized light from a narrow-band LED with $\lambda = 927 \text{ nm}$ at a power density of 53 mW cm^{-2} . For each image, the charge density passed was -3.75 mC cm^{-2} . The deposition potentials are referenced to Ag/AgCl. Insets to (a)-(d) are 2D FT of large-area images of the respective films, scale of inset side is $85.6 \mu\text{m}^{-1}$. (e) Dependence of average particle-to-particle spacing on deposition potential for various Se-Te films deposited on p^+ -Si and n^+ -Si substrates after passing a charge density of -3.75 mC cm^{-2} .

The 2D FT spectra for all the SEMs in Figure 2.1 consisted of a single, radially symmetric peak centered around the origin showing that, at this early stage of phototropic growth, the nucleates of the films were distributed isotropically. In the grayscale 2D FT spectra of the films, more white value farther from the origin corresponds to a higher frequency of nucleates in reciprocal space and thus to a larger contribution from smaller spacings in the real-space image. Wider peaks in the 2D FT spectra thus correspond to smaller nucleate spacings for the deposits. Pair-correlation function analysis (Figure S2.4) corroborated the 2D FT analysis and indicated more random dispersion of the nucleates on p^+ -Si than of the nucleates on n^+ -Si.

Figure 2.1e shows the relationship between the average nucleate spacing of deposits on p^+ -Si and n^+ -Si and the potential applied during the deposition. The nucleate spacing was defined as the inverse of the half width at half maximum (HWHM) of the isotropic peak centered around the origin in the 2D FT spectra. See Figure S2.5-S2.7 for a description of peak fitting in 2D FT spectra. In general, for each substrate, application of a more negative potential during the deposition resulted in smaller nucleate spacings. Conditions which might be hypothesized to produce larger nucleate spacings on p^+ -Si, i.e., relatively more positive applied potentials, resulted in no appreciable growth after several hours of attempted deposition. Other electrodeposited chalcogenide materials have also been observed to exhibit potential-dependent nucleation behavior. For example, the nucleation density of electrodeposited CdSe increases as the deposition potential is made more negative.¹⁹

Figure 2.2 shows the stages of development for Se-Te films grown phototropically on p^+ -Si and n^+ -Si substrates. Such complex three-dimensional structures spontaneously form on unpatterned substrates, with incoherent, unpatterned, low-intensity illumination, from optically isotropic aqueous solutions that do not contain any chemical-directing agents such as ligands or surfactants. The

deposited Se-Te material is p-type and photoactive; there is no requirement for substrate photoactivity. Phototropic growth has been demonstrated on Au, Ti, highly oriented pyrolytic graphite (HOPG), and degenerately doped Si substrates.¹⁷ Although electrodeposition of Se-Te in the dark yields granular films without any long-range order, electrodeposition under uniform, low-intensity polarized light results in highly ordered periodic structures with pitches determined by the intensity-weighted average wavelength of the light, and orientations determined by the direction of polarization. These phototropic lamellar nanostructures emerge from the scattering and interference of incident light at randomly distributed optical dipoles across the growth substrate. This collective response results in a feedback mechanism by which the near-field concentration of light results in preferential mass deposition at the tips of growing lamellae.¹⁵⁻¹⁸ See Figure S2.8-S2.9 for discussion and schemes that elucidate the role of optical dipole scattering and nucleation on the phototropic growth mechanism.

The development of lamellae in phototropic growth is accurately predicted by a two-step, iterative model involving Monte-Carlo mass addition weighted by the optical absorption profile of a simulated Se-Te film that predicts dark nucleation will spontaneously yield order when illuminated by light with a photon energy above the optical bandgap of the Se-Te film.¹⁵⁻¹⁸ An assumption of the growth model is that localized absorption leads directly to localized mass addition, suggesting that phototropic growth is a phenomenon general to semiconductors with short minority-carrier diffusion lengths that can be electrodeposited, as has been demonstrated previously with photoelectrodeposited PbSe and CdSe films.^{14, 20} Notably, Se-Te photoelectrodeposits align along the direction of optical polarization regardless of the orientation with respect to the substrate, and amorphous Se-Te films comprise the deposit itself.¹⁵⁻¹⁸ Hence the helical chain arrangement of Se

and Te atoms is not an important factor in determining the growth order or pattern fidelity of the photoelectrodeposit. Consistently, the mechanistic understanding and modeling of the process described herein that is in full agreement with the experimental observations only includes optical constants of the materials and Maxwell's equations, with no chemical or structural bias, directing agents, or chemically preferred or lattice-matched growth directions. Thus, under these conditions, phototropic growth is a generalizable and fundamental light-matter interaction, and is not dependent on the chemical bonding or structure of the deposited material (e.g., the helical chain arrangement of Se and Te atoms).²¹⁻²² Previous studies have demonstrated substantial amounts of amorphous material in phototropic Se-Te films; Debye-Scherrer analysis of X-ray diffraction (XRD) spectral features revealed the presence of nanocrystalline grains with dimensions on the order of tens of nanometers.¹⁷ Additionally, electron dispersive X-ray spectroscopy (EDS) compositional analysis indicated statistically equivalent Se:Te atomic ratios for phototropic Se-Te films deposited on p⁺-Si, n⁺-Si, and Au substrates (Figure S2.10).

The 2D FT spectra in Figure 2.2 show the transformation of isotropic peaks into anisotropic features in reciprocal space, as anisotropic lamellar structures emerge from the isotropically distributed nucleates. See Figure S2.11 for higher resolution 2D FT spectra and a detailed analysis of features observed in 2D FT spectra during phototropic Se-Te film development. Although after the first charge step (-0.75 mC cm⁻²) the distributions of nucleates were similar for p⁺-Si and n⁺-Si substrates, the distributions differed after the second charge step (-3.75 mC cm⁻²), with smaller nucleate spacings observed on p⁺-Si substrates than on n⁺-Si substrates. After a charge density of -22.5 mC cm⁻² was passed, the Se-Te deposited on n⁺-Si consisted of a relatively sparse distribution of fewer, but larger, discontinuous particles, whereas the Se-Te deposited on p⁺-Si formed a nearly

continuous thin film. As observed in the 2D FT, both films had a mostly isotropic distribution of mass at this stage of pattern formation.

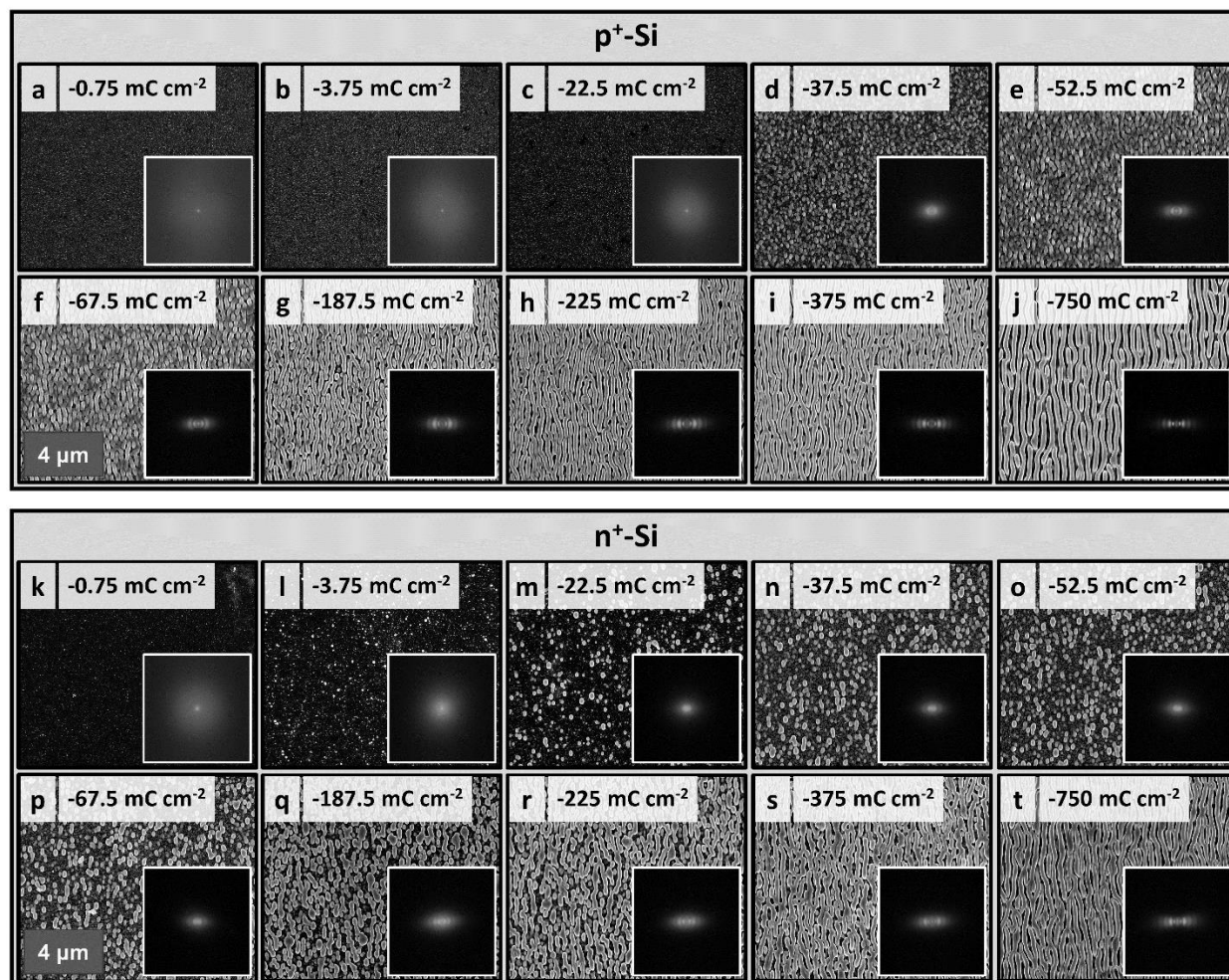


Figure 2.2. Series of SEM images demonstrating representative morphology of films deposited on (a)-(j) p⁺-Si at -80 mV vs. Ag/AgCl and (k)-(t) n⁺-Si at -250 mV vs. Ag/AgCl with characteristic amounts of charge passed (mass deposited) per unit area of: (a), (k) -0.75 mC cm⁻²; (b), (l) -3.75 mC cm⁻²; (c), (m) -22.5 mC cm⁻²; (d), (n) -37.5 mC cm⁻²; (e), (o) -52.5 mC cm⁻²; (f), (p) -67.5 mC cm⁻²; (g), (q) -187.5 mC cm⁻²; (h), (r) -225 mC cm⁻²; (i), (s) -375 mC cm⁻²; and (j), (t) -750 mC cm⁻². Insets to (a)-(t) are 2D FT of large-area images of the respective films, scale of inset side is 85.6 μm⁻¹.

After a charge density of -37.5 mC cm⁻² was passed, early formation of lamellar structures was observed for Se-Te deposited on both p⁺-Si and n⁺-Si substrates. The deposited particles adopted

an elliptical shape, elongated in the vertical direction, parallel to the axis of polarization. At this stage in the deposition, the elliptical particles were larger, more elongated, and more sparsely distributed on n^+ -Si than p^+ -Si. After charge densities of -52.5 and -67.5 mC cm^{-2} had been passed on n^+ -Si substrates, the Se-Te deposited still appeared as vertically oriented elliptical particles with narrower spacing in the horizontal than in the vertical direction, although the number and size of the particles increased as more charge was passed. In contrast, after -52.5 mC cm^{-2} of charge density had been passed on p^+ -Si, the Se-Te appeared as vertically oriented particles made of ellipses that had begun to merge along the vertical direction. The lamellar morphology was more fully formed after 67.5 mC cm^{-2} had been passed on p^+ -Si.

Although qualitatively similar lamellar structures ultimately formed on both p^+ -Si and n^+ -Si, key differences during the early stages of growth influenced the fidelity of the resulting structures. Substantial discontinuity in the Se-Te deposits was present on n^+ -Si at charge densities for which a continuous, thin layer of nucleates was observed on p^+ -Si. Discontinuity and larger nucleate spacings contributed to the “kinked” lamellar morphology observed on n^+ -Si, whereas smaller nucleate spacings contributed to the straighter lamellae and higher fidelity patterns observed on p^+ -Si. Low-magnification, wide-area SEM images of the films in Figure 2.2j and t are provided in Figure S2.2.

Figure 2.3 shows the relationship between the spacing of nucleates at an early stage in the deposition (-3.75 mC cm^{-2}) and both the period (Figure 2.3a) and fidelity (Figure 2.3b) of the lamellar pattern that developed in the films after a charge density of -750 mC cm^{-2} had been passed. The figure-of-merit used to describe the fidelity of the pattern was the vertical full width and half maximum (FWHM) in angular units of the primary peak in the 2D FT of the pattern. See Figure S2.7

and Equation S2.1 for a discussion of the conversion of 2D FT to radial coordinates and pattern fidelity.

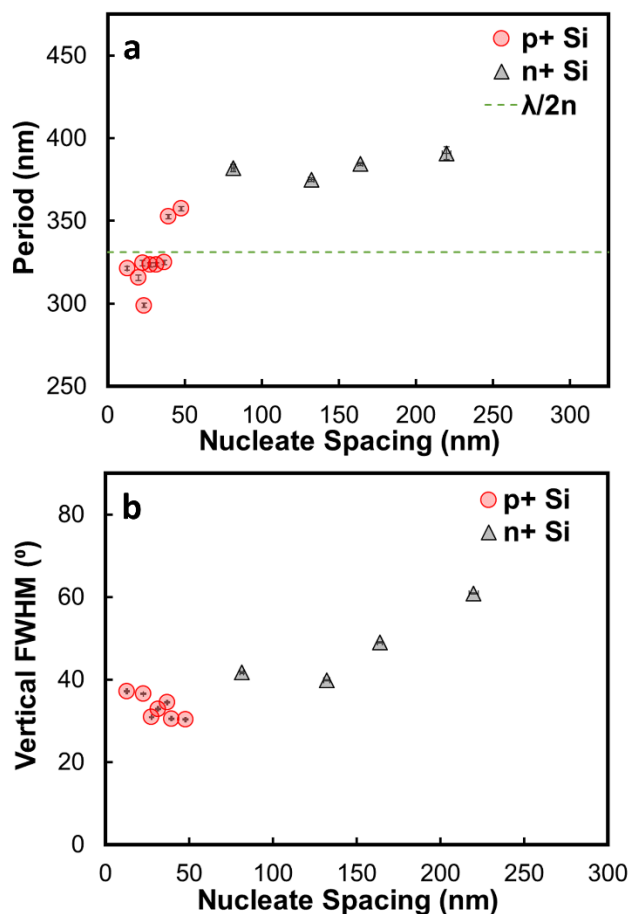


Figure 2.3. Relationship between the average particle-to-particle spacing of nucleated films at early levels of mass deposition (-3.75 mC cm^{-2}) and (a) the observed lamellar period and (b) pattern fidelity as described by the vertical (parallel to axis of polarization) FWHM of the primary peak in the 2D FT of imaged Se-Te films. The lamellar period predicted by an optical model and observed in prior results is $\lambda/2n$ and is indicated in (a). The variation in nucleate spacing for deposits on either p⁺-Si or n⁺-Si substrates was due to a difference in applied deposition potential, as shown in Figure 2.1. The films that were analyzed to obtain lamellar period and vertical FWHM values were deposited at a charge density of -750 mC cm^{-2} . Vertical FWHM and pattern period values are paired with corresponding particle spacing values that share applied deposition potentials ranging from -60 to $-100 \text{ mV vs. Ag/AgCl}$ for p⁺-Si and -200 to $-300 \text{ mV vs. Ag/AgCl}$ for n⁺-Si.

The lamellar period in phototropic Se-Te films illuminated with 927 nm light is predicted by our growth model¹⁵⁻¹⁸ to be 331 nm, and corresponds to $\lambda/2n$, where λ is the illumination wavelength and n is the index of refraction of the medium in which the phototropic growth occurs, equal to 1.4 (the index of refraction of the aqueous sulfuric acid solution). In Figure 2.3, small (≤ 50 nm) nucleate spacings were observed for depositions onto p⁺-Si substrates for all applied potentials tested, whereas the nucleate spacings observed for depositions onto n⁺-Si substrates were generally larger and were as high as ~ 225 nm. Smaller spacings between nucleates resulted in patterns with smaller periods that approached the predicted $\lambda/2n$ value. Smaller spacings between nucleates also resulted in patterns with higher fidelities. The observations of a smaller lamellar period and straighter lamellae for certain films suggest that more closely packed lamellae develop under conditions that produce closely spaced nucleates in the early stages of mass deposition.

Given the potential dependence of nucleation,²³⁻³⁰ potential-striking steps are often used to increase the quality of electrodeposited films. For instance, inclusion of a strike step reduces the porosity of electrodeposited gold films.³¹ Figure 2.4 shows SEM images and 2D FT spectra of Se-Te films that were phototropically grown on p⁺-Si (Figure 2.4a - e) and n⁺-Si (Figure 2.4f - j) using varied striking potentials for the first -3.75 mC cm⁻² of mass deposition (corresponding to 0.5% of the total mass deposited). Following the initial striking step, the remaining 99.5% of mass (-746.25 mC cm⁻²) was deposited at a relatively more positive potential (-80 mV on p⁺-Si and -200 mV on n⁺-Si). See Figure S2.12 for a graphical depiction of the striking potential experiments. As observed in Figure 2.1e, a wide range of nucleate spacing can be accessed for Se-Te films grown on n⁺-Si substrates by tuning the deposition potential. The striking step was performed using a more negative potential than the subsequent mass-addition step, and consistently, smaller nucleate spacings were

consequently produced on n^+ -Si substrates than would have been produced if the entire deposition were performed at the potentials used for the mass-addition step. When performed entirely at the potentials applied during striking steps, depositions on n^+ -Si do not result in purely phototropic Se-Te films. Rather, dark growth is a major contribution at later stages of mass-addition when applying these more negative potentials (Figure S2.13). The direct effects of nucleate spacing on the fidelity of lamellar patterns formed in Se-Te films were thus measured by varying the deposition potential during the earliest stage of mass deposition while using the same potential for deposition of the majority of the mass.

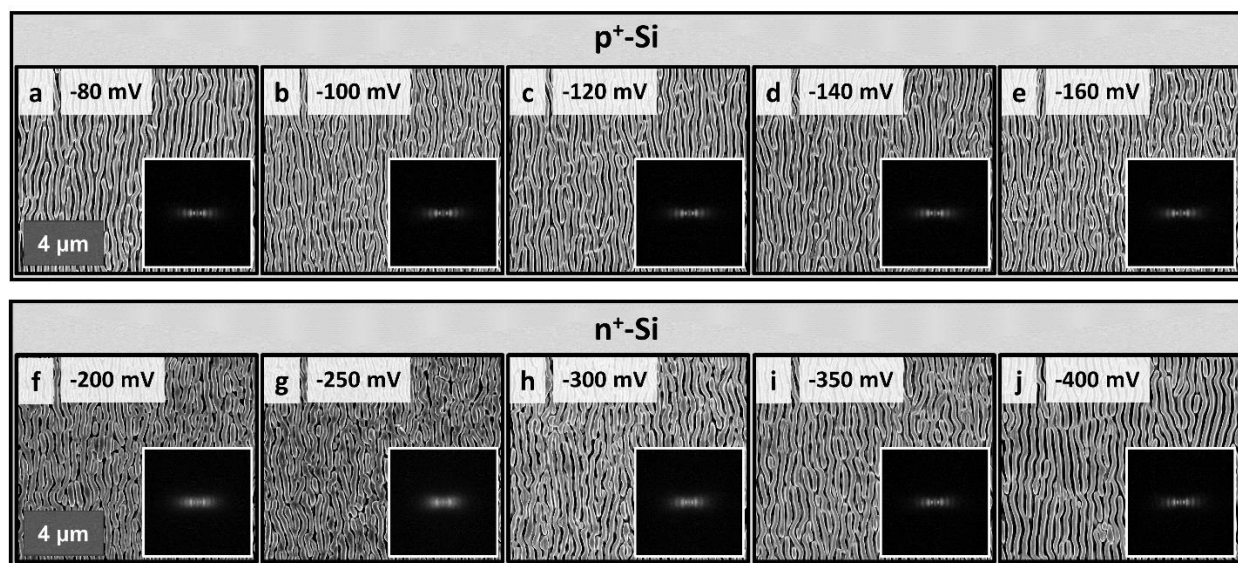


Figure 2.4. Series of SEM images demonstrating representative morphology of films deposited to a total of -750 mC cm^{-2} on (a)-(e) p^+ -Si at -80 mV vs. Ag/AgCl and (f)-(j) n^+ -Si at -200 mV vs. Ag/AgCl after depositing -3.75 mC cm^{-2} in an applied potential strike step. (a) control at -80 mV and striking potentials of (b) -100 mV , (c) -120 mV , (d) -140 mV , and (e) -160 mV vs. Ag/AgCl on p^+ -Si. (f) control at -200 mV and striking potentials of (g) -250 mV , (h) -300 mV , (i) -350 mV , and (j) -400 mV vs. Ag/AgCl on n^+ -Si. Insets to (a)-(t) are 2D FT of large-area images of the respective films, scale of inset side is $85.6 \mu\text{m}^{-1}$.

Films grown on p^+ -Si with a striking step (Figure 2.4b - e) were similar in appearance to the control sample (Figure 2.4a). Films grown on n^+ -Si, however, changed in appearance relative to the

n^+ -Si control when a striking step was added. The control sample on n^+ -Si (Figure 2.4f) exhibited short, discontinuous lamellae and pattern defects such as dislocations and interstitial features. Relative to the control sample on n^+ -Si, samples grown with a striking step (Figure 2.4g - j) exhibited straighter, more continuous lamellae and fewer pattern defects. This improved fidelity was also observed as sharpening of the peaks in the 2D FT as the striking potential was made more negative. As evident in both the 2D FT spectra and the SEM images, the fidelity of phototropic Se-Te films was strongly influenced by the morphology of the very earliest levels of mass addition.

Figure 2.5 shows the relationship between the striking potential and fidelity of phototropic Se-Te films, described by the vertical FWHM of the primary peak in the 2D FT. The trend observed in the SEM images and 2D FT spectra in Figure 2.4 is reflected in Figure 2.5, showing an improvement in the pattern fidelity of phototropic Se-Te films deposited on n^+ -Si as the striking potential was made more negative. Figure 2.5 also shows the effects of a longer striking step at 1.0% of total mass deposited (-7.5 mC cm^{-2}). When performing the striking step for 1.0% versus 0.5% of mass deposited, phototropic Se-Te films did not require as negative a striking potential to exhibit improved pattern fidelity, suggesting that nucleate spacing decreases with increasing amounts of deposition under these conditions. In contrast, phototropic Se-Te films on p^+ -Si showed no improvement over the control sample when the striking step was performed for either 1.0% or 0.5% of mass deposited. Furthermore, at the conditions tested, films on n^+ -Si reached an apparent upper limit of pattern fidelity near to what was observed on p^+ -Si, $\sim 30^\circ$ for the vertical FWHM. The limit of pattern fidelity in Se-Te films is also reflected in the average particle-to-particle spacing data in Figure 2.1e, which shows nucleate spacing values for n^+ -Si approaching values observed on p^+ -Si as the applied deposition potential is made more negative. Both observations suggest that below a

critical level of nucleate spacing, ~ 50 nm, no further contribution to improved pattern fidelity is obtained for the conditions tested.

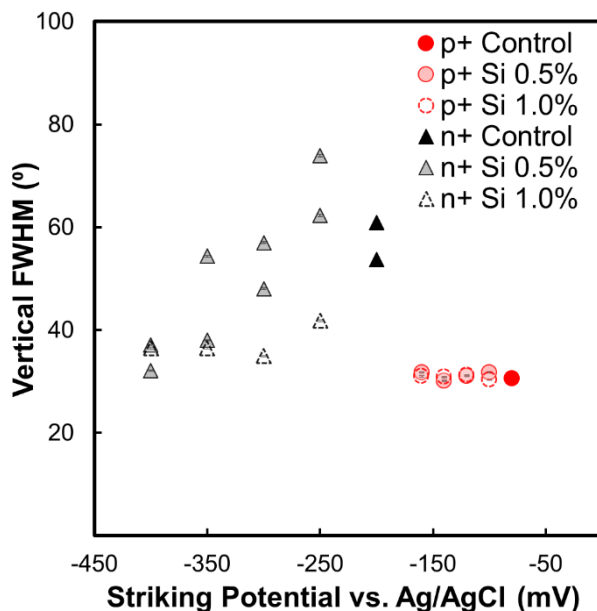


Figure 2.5. Relationship between striking potential and pattern fidelity as described by the vertical (parallel to axis of polarization) FWHM of the primary peak in the 2D FT of imaged Se-Te films. The striking-potential step was performed on p⁺-Si and n⁺-Si substrates until a charge density of either -3.75 mC cm^{-2} (0.5%) or -7.5 mC cm^{-2} (1.0%) had been passed. The remainder of the charge density (to -750 mC cm^{-2}) was passed at -80 mV (p⁺-Si) and -200 mV (n⁺-Si) vs. Ag/AgCl. Control experiments are Se-Te films deposited without any striking-potential step.

The results suggest that the deposition of Se-Te on n⁺-Si follows a progressive nucleation mechanism, rather than an instantaneous nucleation mechanism.³² Progressive nucleation mechanisms, such as the Volmer-Weber mechanism, are characterized by 3D island growth, which has also been observed in the electrodeposition of other chalcogenide materials, such as PbTe on n-Si.³³ In an electrochemical system exhibiting instantaneous nucleation, all electrochemically active sites are nucleated during the initial stages of mass addition, and the nucleation density does not change substantially with the amount of mass deposited.³⁴ No substantial change was observed in

the Se-Te nucleate spacings on p^+ -Si at different applied deposition potentials nor was a change in the fidelity of phototropic Se-Te films on p^+ -Si observed when a striking step was included, so the results are consistent with either an instantaneous nucleation mechanism or a relatively higher rate of progressive nucleation during Se-Te nucleation on p^+ -Si. The nucleate spacings on n^+ -Si substrates decreased as the applied potential was increased negatively, suggesting that the nucleation mechanism is potential-dependent. Thus, progressive nucleation on n^+ -Si demonstrated increased nucleation rates as the applied deposition potential was made more negative, potentially approaching an instantaneous nucleation mechanism.

Although electrochemical nucleation is widely known to exhibit a substantial potential dependence due to the mass transport and diffusion of charged species in a solution to the surface of a working electrode,²³⁻³⁰ the effect of various nucleation morphologies on photoelectrochemical deposition and *in-situ* synthesis of semiconductors onto non-photoactive substrates³⁵⁻³⁹ is not well-elucidated or understood mechanistically at present. The long-range order of phototropically grown Se-Te films, as measured using Fourier-transform analysis, varies for growths on different substrates.⁴⁰ We observed previously through 2D Fourier-transform (2D FT) analysis that, under nominally identical illumination conditions, the lamellar pattern fidelity was higher when Se-Te films were deposited on crystalline (111)-oriented Si degenerately doped with p-type dopants (p^+ -Si) than with n-type dopants (n^+ -Si). A more highly ordered lamellar morphology was also observed on p^+ -Si under conditions that resulted in dark and light current densities nominally identical to those measured on n^+ -Si. We attributed the variations in pattern fidelity to effects of the type of junction formed between the substrate and the growing Se-Te film. Consistently, higher fidelity patterns were observed on substrates forming ohmic contacts to Se-Te (i.e., p^+ -Si and Au) whereas patterns on

substrates forming non-ohmic contacts to Se-Te (i.e., n⁺-Si and Ti) consistently exhibited defects and lower pattern fidelity. The data herein confirm the hypothesis that the electrical contact differences between Se-Te films and n-Si or p-Si substrates primarily serve to produce different levels of disorder in the dark growth phase of the material, and the resulting differences in disorder between the dark electroplated films inherently and inevitably produce different amounts of spatial order in the resulting phototropically grown Se-Te overlayers.

The interaction of light with semiconducting electrodes can produce films with three-dimensional morphologies that are not accessible through other materials-processing techniques. For example, illumination of p-Si microwires during the electrodeposition of metals results in rings of metal nanoparticles at positions that are determined by the wavelength of illumination,⁴¹ and illumination of Cu₂O microcrystals during electrochemical etching results in facet-selective deposition of metallic Cu shells.⁴² Moreover, depending on the work function of the metal, illuminating macroporous p-type silicon during metal electrodeposition can spatially direct mass to deposit in patterns that are not accessible by dark depositions.⁴³

Other structures have been fabricated with periodic morphologies determined by the wavelength and direction of polarization of incident light. For example, sub-micron scale periodic structures have been observed to form in azo-dye polymer films when illuminated with light near the dye's absorption band due to the *cis-trans* isomerization and subsequent structural reorientation of azo-dye molecules inside the polymer film.⁴⁴ Another phenomenon, laser-induced periodic surface structures (LIPSS), has been used to produce sub-wavelength features as small as $\lambda/10$.⁴⁵ Both of these phenomena have only been observed when using a coherent illumination source, i.e., a laser. In addition, LIPSS requires high-power illumination near the ablation threshold of the

material being patterned, often in the kW cm^{-2} or MW cm^{-2} range. In contrast, phototropic growth of Se-Te lamellae has no requirement for illumination coherency and can be performed under illumination intensities of $< 10 \text{ mW cm}^{-2}$.

Phototropically grown films adopt morphologies similar to the lamellar structures observed in biological systems (e.g., butterfly wings) in which they often demonstrate structural coloration and anisotropic de-wetting useful for self-cleaning.⁴⁶⁻⁴⁸ As a proof of concept, materials engineered via LIPSS with similar morphologies to butterfly wings have demonstrated both structural coloration and especially large ($>150^\circ$) contact angles for water.⁴⁹⁻⁵⁰ As a bottom-up, solution-based fabrication method, phototropic growth presents an inexpensive, scalable, and highly tunable alternative to fabrication of these biomimetic structures. Improvements in the long-range order of phototropically grown films will result in increased levels of lamellar anisotropy and will likely improve the usefulness of the patterned structures in various applications, including self-cleaning surfaces and structural coloration elements.

2.3 Conclusion

In inorganic phototropic growth, an initially isotropic dark nucleation spontaneously yields anisotropic spatially ordered nanostructures. Though principally an optically driven process, the phototropic growth model predicts that random variation in the dark electrodeposition process produces sites of surface roughness that scatter incoming illumination. As the deposition progresses, a subset of the initially random distribution of nucleates is selected where absorption “hot-spots” occur due to scattered light from nearby sites. These optically selected sites exhibit increased rates of mass addition due to the surface photovoltaic effect, leading to the observation and persistence of

lamellar nanostructures. The distribution of Se-Te nucleates during the early stages of photoelectrodeposition depends on the applied deposition potential and substrate. Due to electrical junction effects,⁴⁰ Se-Te deposition on p⁺-Si substrates produces smaller nucleate spacings than on n⁺-Si substrates. However, nucleate spacings on n⁺-Si were decreased considerably, and the resulting Se-Te pattern fidelities improved, by adjusting the applied deposition potential during an initial potential-striking step. In general, pattern fidelities were high when nucleate spacings were small. Small nucleation spacings also resulted in phototropic Se-Te films with lamellar patterns with periods that strongly agreed with a predicted trend of $\lambda/2n$.

Perhaps enigmatically, our results show that higher pattern fidelity and longer-range order in phototropically grown Se-Te films requires initial conditions of more disorder, or randomness, in the initial dispersion of scattering sites (nucleates). Contrary to previous phototropic growth studies (Table S2.1), this study demonstrates that the early distribution of nucleates is fundamental in determining pattern fidelity in phototropic films. For instance, phototropic growth of Se-Te films on Au substrates follows the observed trend of increased pattern fidelity at smaller nucleate spacings (Figure S2.14-S2.15). Given that the photo-driven mass deposition can only occur where light is absorbed, a more uniform nucleation layer allows the developing film to adopt a morphology that is primarily influenced by local light absorption, maximizing the contribution from the self-optimized scattering and absorption feedback mechanism. Conversely, a less uniform nucleation layer with larger spacings between nucleates results in a growth process in which the pattern fidelity is the result of the convolution of the local field intensity and a non-uniform layer of mass. Thus, the distribution of the first nucleated particles deposited can strongly influence the resulting pattern fidelity in

phototropic Se-Te films after ~200 times more mass has been deposited than in the initial dark nucleation process.

2.4 Supporting Information

2.4.1 Experimental methods and materials

Unless otherwise noted, all experiments were performed following nominally identical procedures from our previously reported work.⁴⁰ This included chemicals and materials used, equipment used, electrode fabrication procedures, electrochemical configuration, optical configuration, sample preparation, and image acquisition as was described in Section 2.4.2 of the Supporting Information.

2.4.2 Examples of low-magnification images

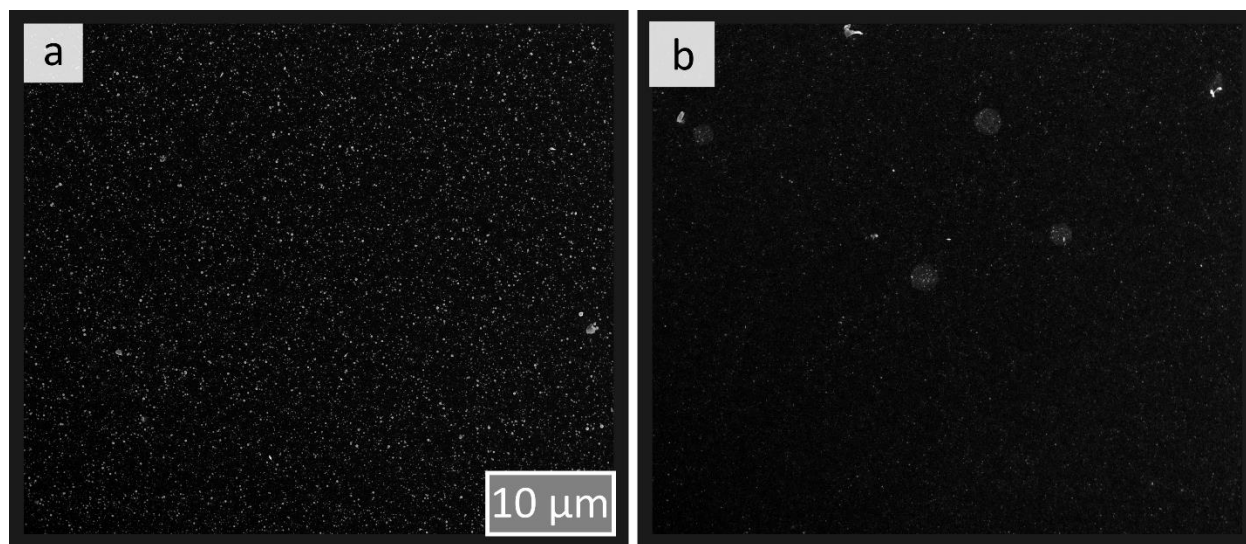
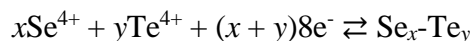


Figure S2.1: Low-magnification SEM images of photoelectrodeposited Se-Te films shown in Figure 2.1 grown on n^+ -Si at a charge density of -3.75 mC cm^{-2} using vertically polarized $\lambda = 927 \text{ nm}$ illumination at a power density of 53 mW cm^{-2} . (a) deposited at relatively more positive deposition potential, (b) deposited at relatively more negative deposition potentials vs. Ag/AgCl. These SEM images were obtained at a magnification of 6250 X and a resolution of 4096 x 3536 pixels, which

corresponded to ~ 85.8 pixels μm^{-1} . The applied deposition potentials are reported versus a reference potential rather than as an overpotential to the reversible potential. The reversible potential is not known for the following reaction:



The solid-liquid interface changes dramatically during deposition of the Se-Te alloy producing an accompanying response in the open-circuit potential (OCP), complicating the reporting of an overpotential to the reversible potential for this reaction. Additionally, the OCP is observed to depend on substrate choice and the solid-solid or solid-liquid junctions formed. Accordingly, we prefer reporting the applied deposition potential (used in a potentiostatic deposition experiment) versus a reference potential.

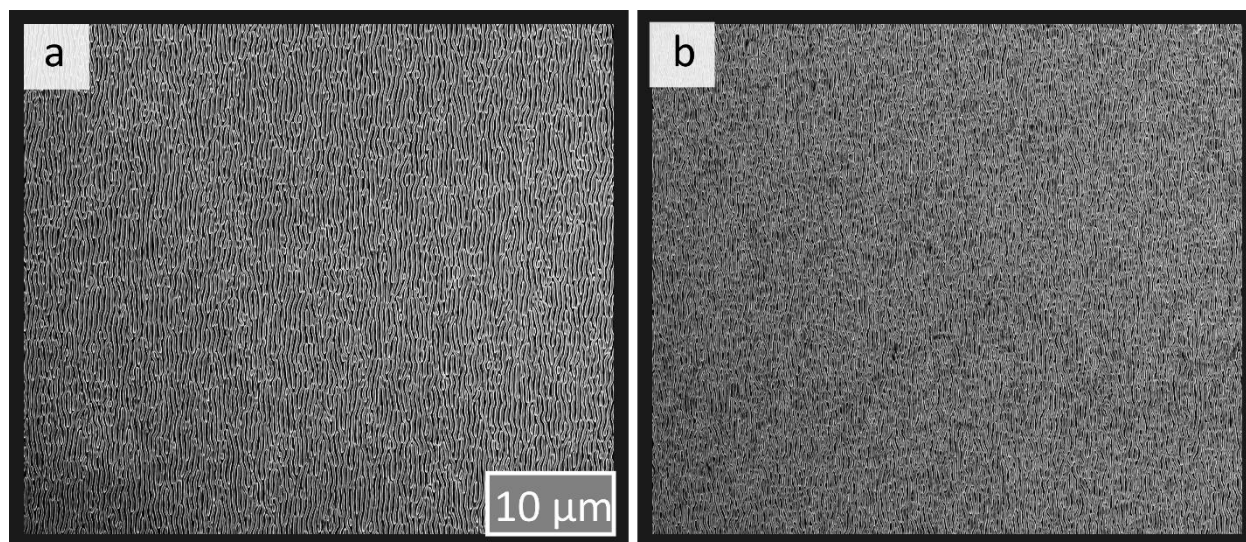
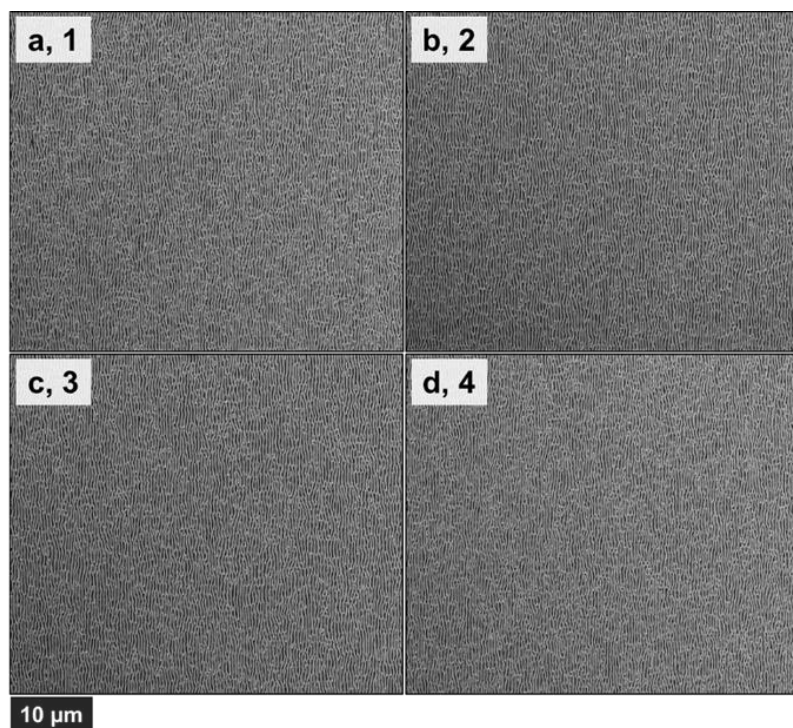
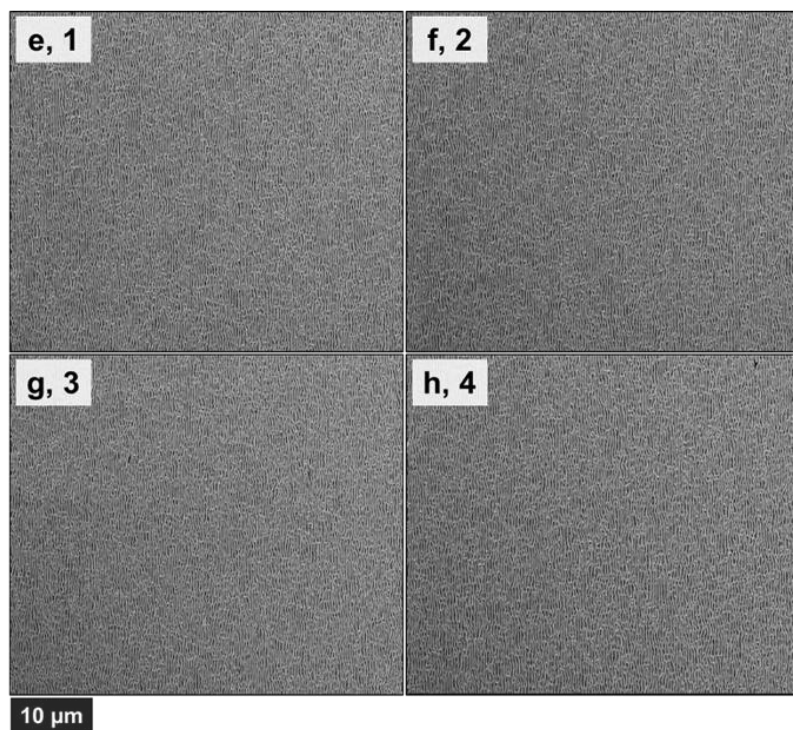


Figure S2.2: Low-magnification SEM images of photoelectrodeposited Se-Te films that were deposited at a charge density of -750 mC cm^{-2} using vertically polarized $\lambda = 927$ nm illumination at a power density of 53 mW cm^{-2} on (a) p^+ -Si and (b) n^+ -Si, corresponding to Figure 2.2j and t, respectively. These SEM images were obtained at a magnification of 6250 X and a resolution of 4096×3536 pixels, which corresponded to ~ 85.8 pixels μm^{-1} .

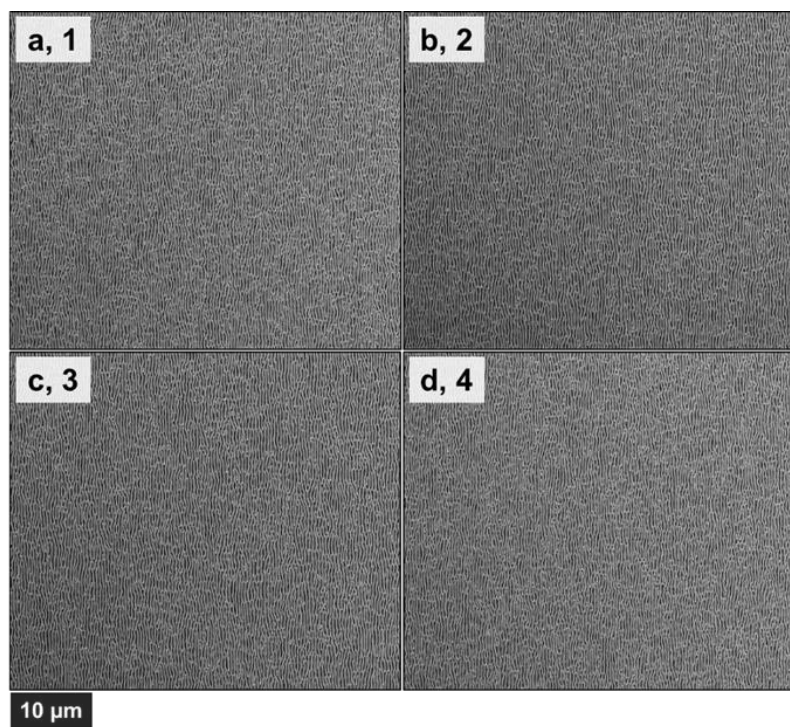
2.4.3 Reproducibility



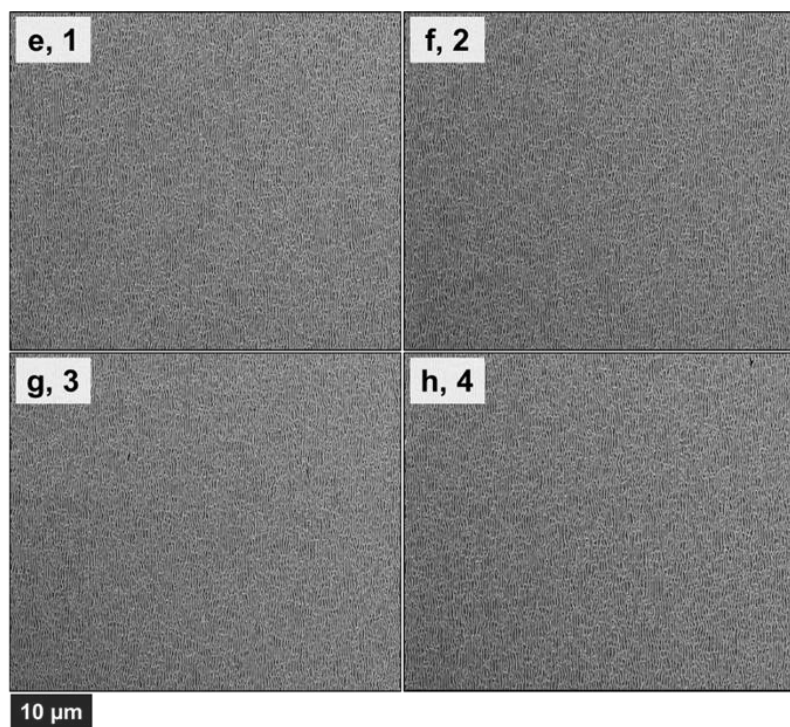
Spot #	Period (nm)	Vertical FWHM (°)
1	370.4	31.7
2	367.1	28.0
3	371.3	29.6
4	357.1	30.4



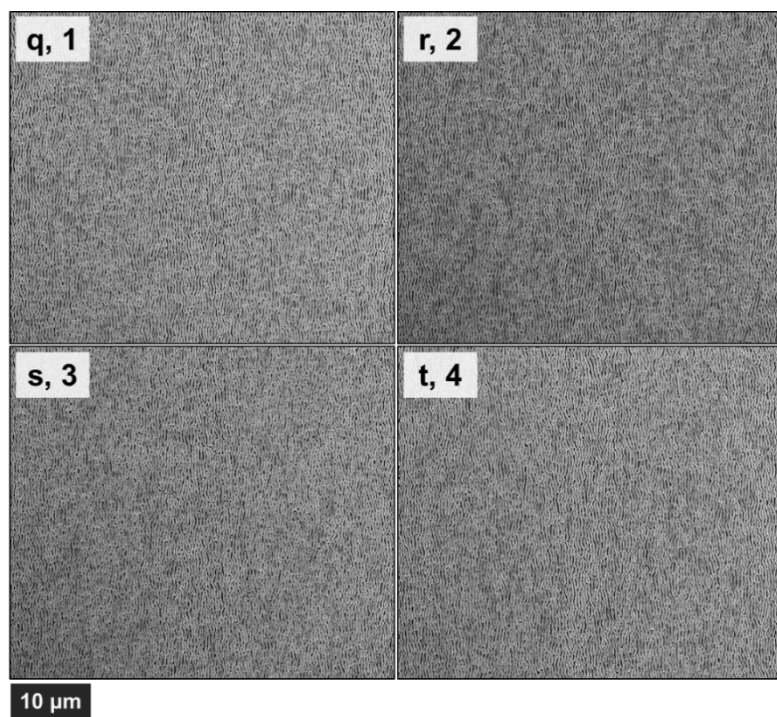
Spot #	Period (nm)	Vertical FWHM (°)
1	322.8	33.7
2	328.5	33.0
3	323.8	34.6
4	332.8	32.9



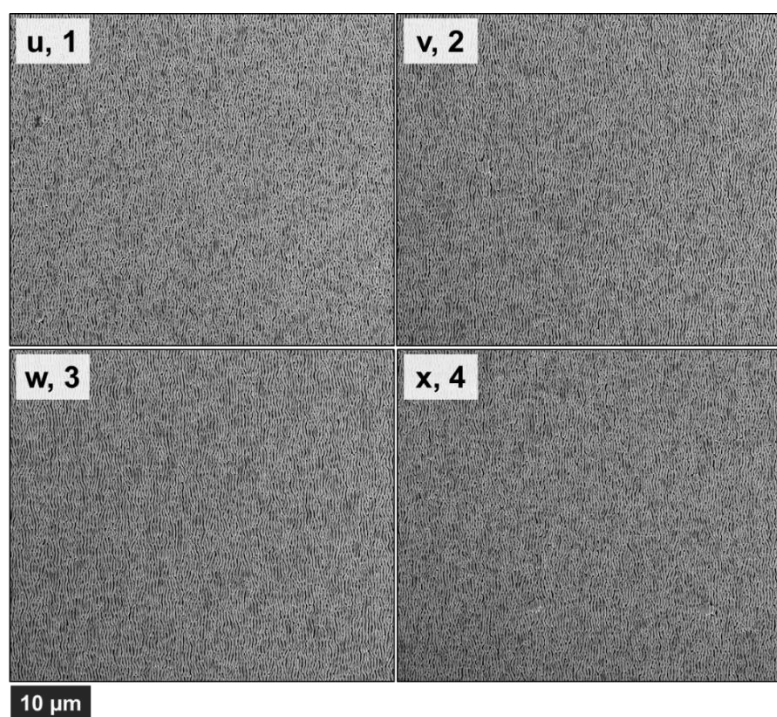
Spot #	Period (nm)	Vertical FWHM (°)
1	370.4	31.7
2	367.1	28.0
3	371.3	29.6
4	357.1	30.4



Spot #	Period (nm)	Vertical FWHM (°)
1	322.8	33.7
2	328.5	33.0
3	323.8	34.6
4	332.8	32.9



Spot #	Period (nm)	Vertical FWHM (°)
1	368.6	41.6
2	373.8	41.8
3	368.3	47.1
4	373.1	42.4



Spot #	Period (nm)	Vertical FWHM (°)
1	360.8	46.7
2	372.0	42.6
3	372.2	41.2
4	367.1	47.3

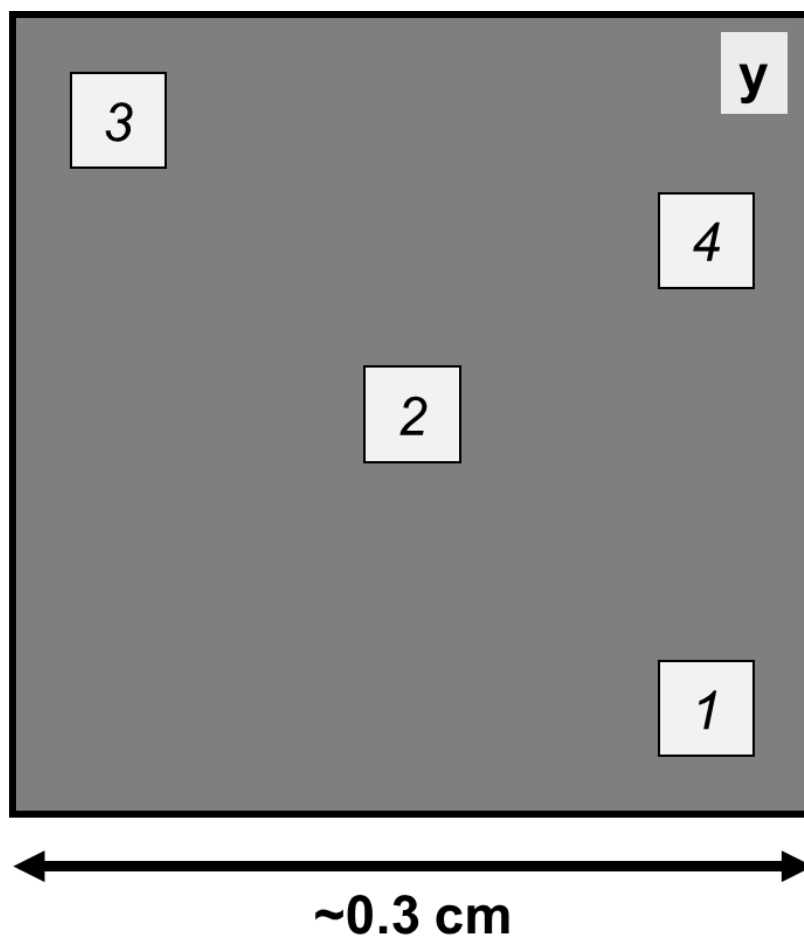


Figure S2.3: Low-magnification SEM images of Se-Te films that were photoelectrodeposited at a charge density of -750 mC cm^{-2} using vertically polarized $\lambda = 927 \text{ nm}$ illumination at a power density of 53 mW cm^{-2} on (a-l) $\text{p}^+\text{-Si}$ and (m-x) $\text{n}^+\text{-Si}$. These SEM images were obtained at a magnification of 6250 X and a resolution of 4096×3536 pixels, which corresponded to $\sim 85.8 \text{ pixels } \mu\text{m}^{-1}$. Each set of four images (a-d, e-h, etc.) corresponds to various spots on a single phototropic Se-Te film; approximate locations of 1, 2, 3, or 4 are noted in (y). Pattern fidelity information is given in adjacent tables, showing that patterns generally displayed excellent reproducibility across macroscopic length scales.

2.4.4 Pair-correlation function (PCF) examples

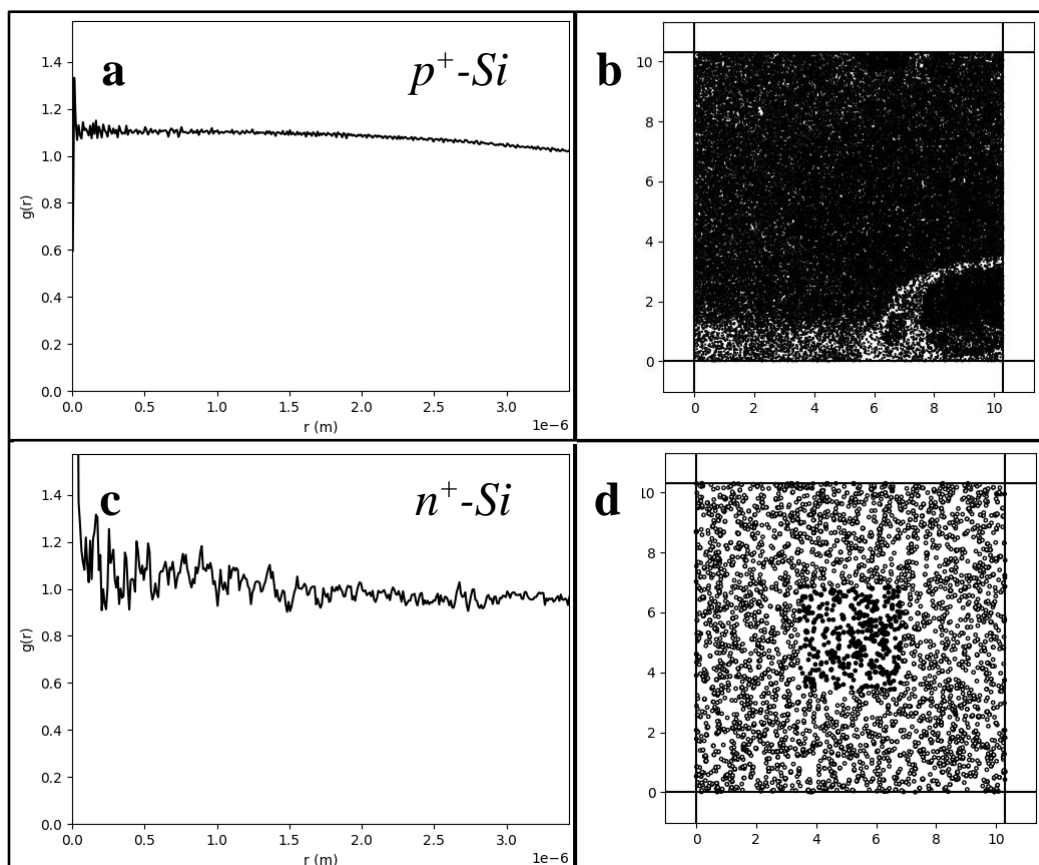


Figure S2.4: Results of a pair-correlation function (PCF) analysis performed on data obtained from the images in (a), (b) Figure 2.1a and (c), (d) Figure 2.1c, corresponding to Se-Te nucleates on p^+ -Si and n^+ -Si, respectively. PCF plots in (a), (c) were obtained via a pair-correlation Python script⁵¹ provided via GNU General Public License v3.0. Particle coordinate data in (b), (d) were obtained using grain analysis in the Gwyddion software package (www.gwyddion.net). Axis units in (b), (d) are in μm ; test points used in PCF analysis are confined to a central square region comprising $1/9^{\text{th}}$ of the total area. The PCF analysis of nucleates on p^+ -Si shows a higher degree of randomness in the distribution of particles, as observed in the smooth and isotropic plot. Conversely, the PCF analysis of nucleates on n^+ -Si shows more disorder in the PCF plot, corresponding to less randomly distributed particles. PCF analysis weights all particles equally through a binary input of coordinate data either containing or not containing nucleates. FT analysis provides a gradient of weighting based on white value in the imaged nucleates. We believe that FT analysis is a more robust method for characterizing certain film morphologies in which exact nucleate coordinates are not obvious or easily recognized. For instance, in many of the p^+ -Si nucleates, film morphologies are closer to thin films than distributions of distinct particles, thus making PCF analysis difficult and prone to error generated during the grain analysis step. Given its broader applicability, FT is our preferred method of analysis for assessing the distribution of Se-Te nucleates on all substrates.

2.4.5 Peak-fitting methodologies

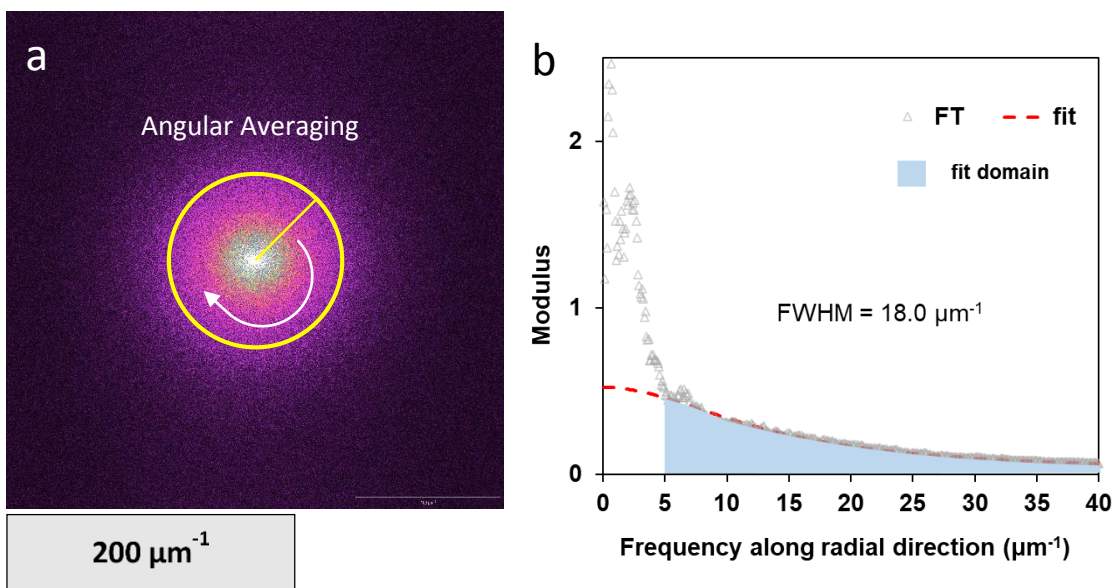


Figure S2.5: To determine the nucleate spacing, SEM images were obtained of samples deposited at a charge density of -3.75 mC cm^{-2} at 50 k magnification and at a resolution of 2048×1768 pixels, which corresponded to $\sim 171.6 \text{ pixels } \mu\text{m}^{-1}$. As a representative example, (a) shows a 2D FT spectrum of one of these images. To obtain the nucleate spacing, the 2D FT was angularly averaged around the origin to obtain the radial spectrum shown in (b). To minimize overlap from the centroid DC peak of the 2D FT spectrum, the decay of the radial spectrum was fit using a Lorentzian function in which the mean of the distribution was fixed to the origin and the fit domain range was fixed between $5 \mu\text{m}^{-1}$ and $100 \mu\text{m}^{-1}$. The peak half-width at half maximum (HWHM) of the resulting fit was inverted to obtain the nucleate spacing used as a figure-of-merit as reported in the main text. Larger HWHM values indicated smaller nucleate spacing.

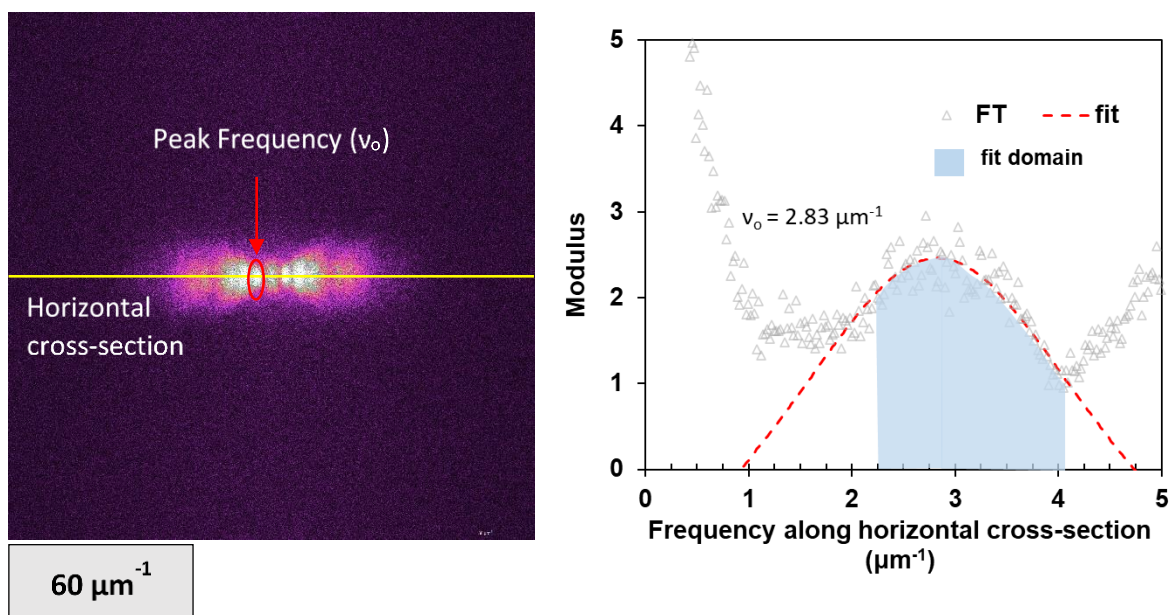


Figure S2.6: 2D FT spectra of large-area SEM images, such as those in Figure S2.2, were used to obtain the average pattern period measurements reported in Figure 2.3 of the main text. An example is provided in (a), showing symmetric lobes along the horizontal axis, perpendicular to the axis of polarization. A horizontal cross section through the origin, integrated over 30 pixels vertically, gave the profile in (b). A Lorentzian function was fit to the primary peak in the obtained spectrum. The domain of the fit was chosen to minimize the residual between the fit and the data. The center frequency of the peak, ν_o , was recorded. The inverse of ν_o corresponded to the average primary pattern period.

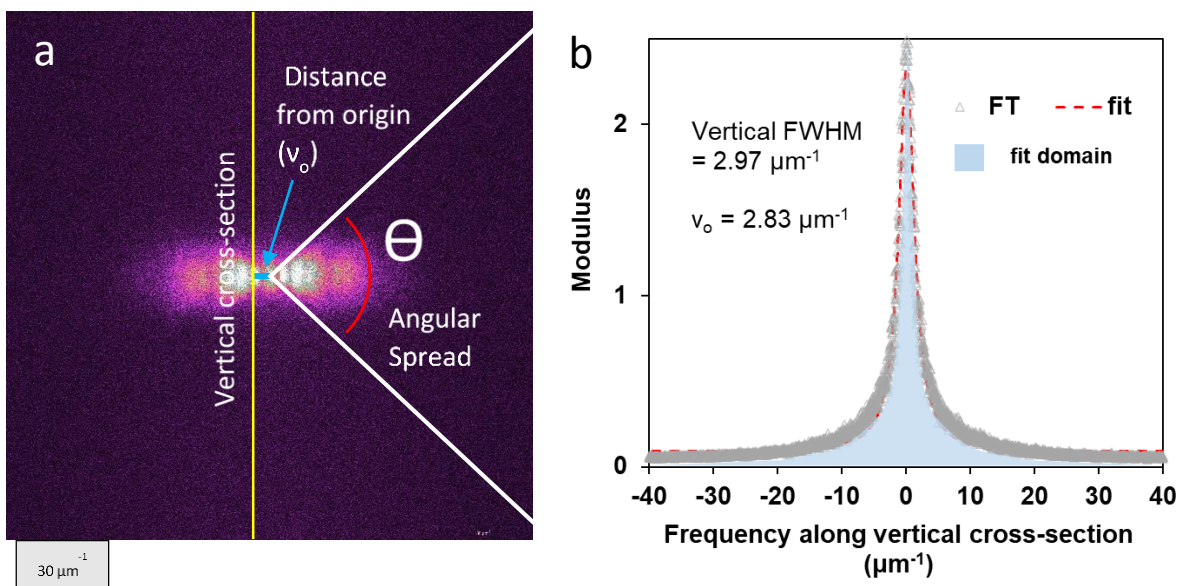


Figure S2.7: 2D FT spectra of large-area SEM images, such as those in Figure S2.2, were used to obtain the angular FWHM measurements reported in Figure 2.3 of the main text. An example is provided in (a). A vertical cross section through v_o as obtained in Figure S2.6, integrated over 30 pixels horizontally, gave the profile in (b). A Lorentzian function was fit to this peak in the obtained spectrum, with the entire profile included in the fit domain. The peak full-width at half maximum (FWHM) was obtained, in μm^{-1} , and converted to radial coordinates using the formula in Equation S2.1. Narrower FWHM corresponded to higher pattern fidelity.

$$\text{Equation S2.1} \quad \text{Vertical FWHM } (^{\circ}) = 2 \tan^{-1} \left(\frac{\text{Vertical FWHM}}{2 \cdot v_o} \right)$$

2.4.6 Schemes for phototropic growth mechanism

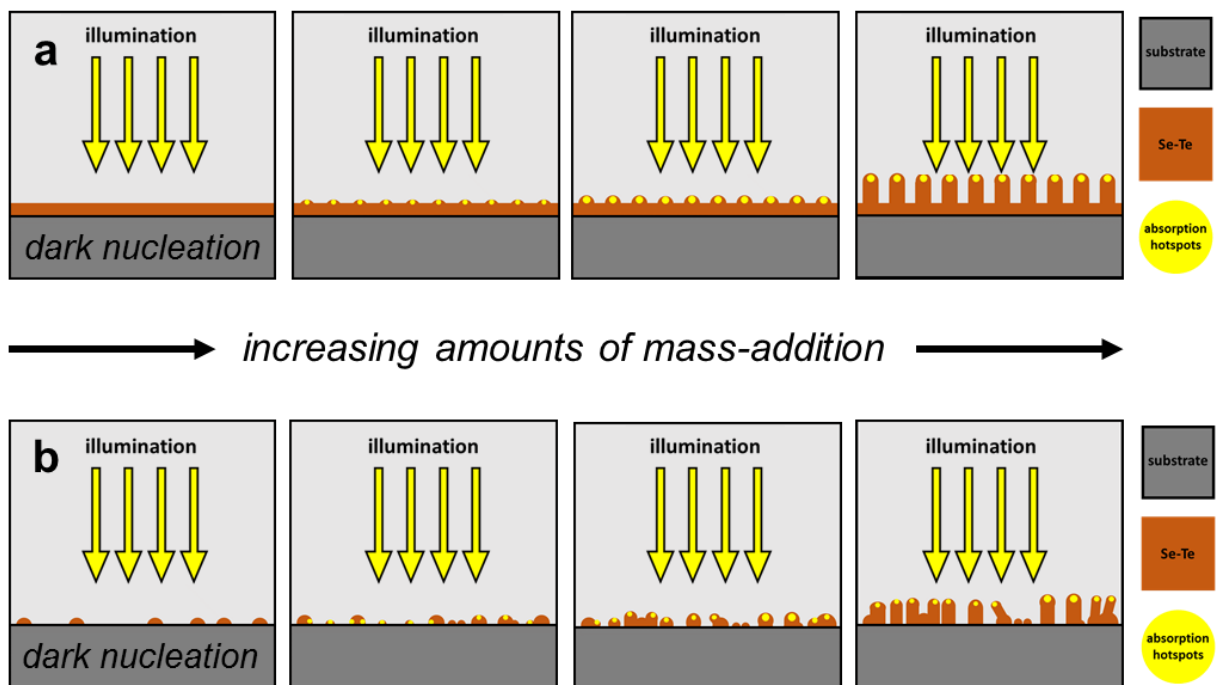


Figure S2.8: Schemes showing the process by which an initially dark Se-Te nucleation results in highly ordered, periodic lamellae when illuminated with polarized light with a photon energy above the optical bandgap of Se-Te. Scheme in (a) demonstrates phototropic growth wherein dark phase nucleation resembles a thin, continuous film of Se-Te material. The panels in Scheme (b) depict phototropic growth wherein dark phase nucleation is slow, progressive, and discontinuous. A more random and continuous distribution of optical dipole scatterers, i.e., nucleated Se-Te particles or surface roughness on a thin Se-Te film (Scheme a), results in higher fidelity pattern formation regardless of the direction or wavelength of the incident light beam. This property derives from maximization of mass addition due to local light absorption over the duration of pattern formation. In contrast, a discontinuous or sparse distribution of optical dipole scatterers results in a delay and misregistry in phototropically grown pattern formation. Dislocations in the phototropically grown film thus result from discontinuity in the nucleation morphology. Conversely, discontinuity in nucleated films directly results in pattern defects.

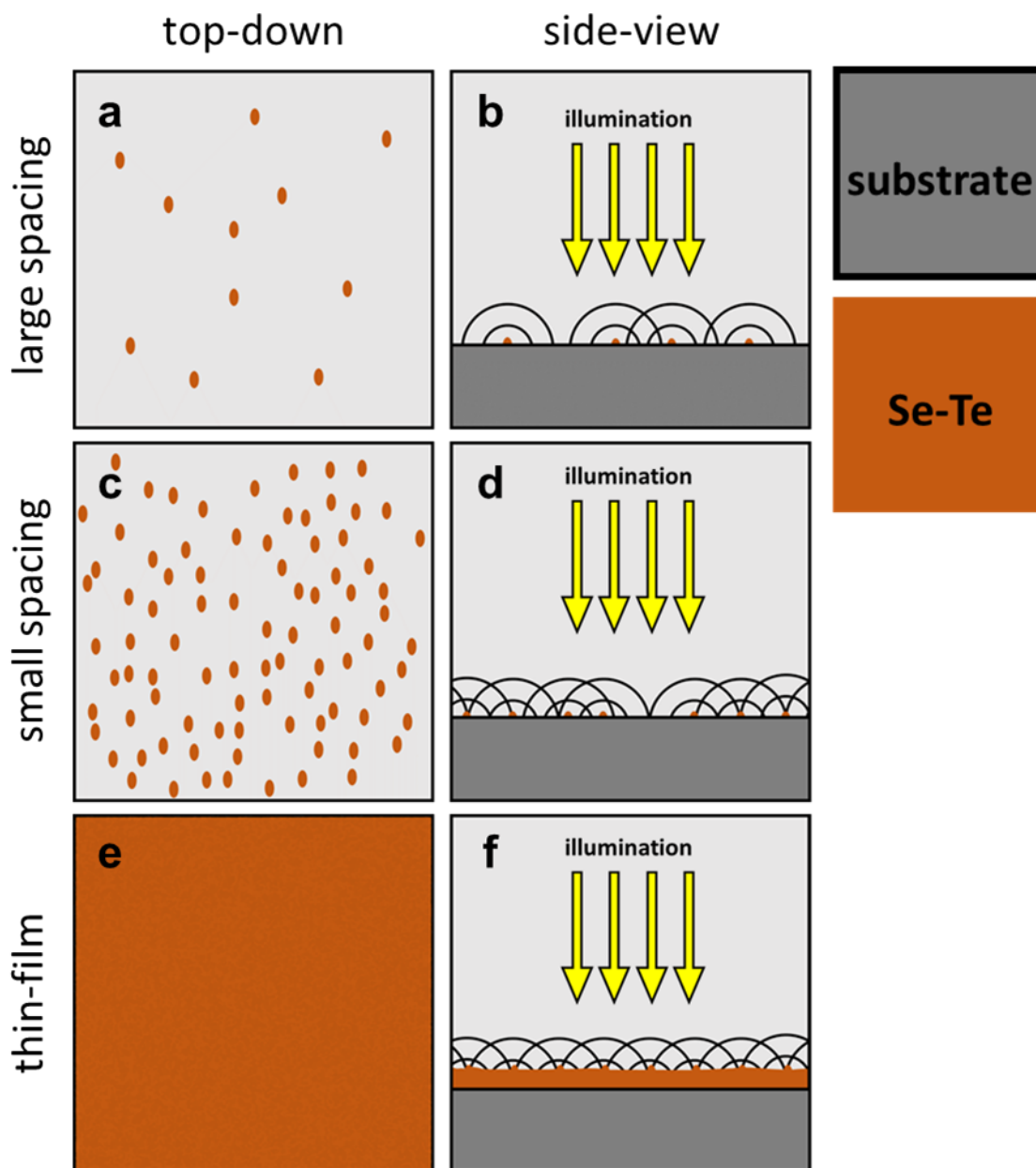


Figure S2.9: Schemes showing the interaction of scattered light waves with nucleated Se-Te optical dipole scatterers. Diagrams in (a), (b) show an initial Se-Te nucleation morphology characterized by large nucleate spacing; diagrams in (c), (d) show an initial Se-Te nucleation morphology characterized by small nucleate spacing; diagrams in (e), (f) show an initially thin-film Se-Te nucleation morphology. In the case of (e), (f), a thin-film nucleation results in the highest tolerance for overlap between mass availability and scattered-wave intensity. In the case of (c), (d), gaps in nucleation spacing can lead to conditions in which optical dipole scatterers are not in collective resonance. In the case of (a), (b), larger nucleation spacing further increases the chances of dipole-scatterers being out of collective resonance for a given excitation wavelength and direction of optical

incidence. The coincidence of mass and scattered-wave intensity is a prerequisite for a corresponding coincidence of scattered-wave intensity and local light absorption. Furthermore, local light absorption is proportional to mass addition in phototropic growth, hence the conditions that produce better overlap between mass and scattered-wave intensity maximize light-directed growth, consequently producing higher anisotropy — and higher fidelity — in phototropic films.

2.4.7 Electron dispersive X-ray spectroscopy (EDS) compositional analysis

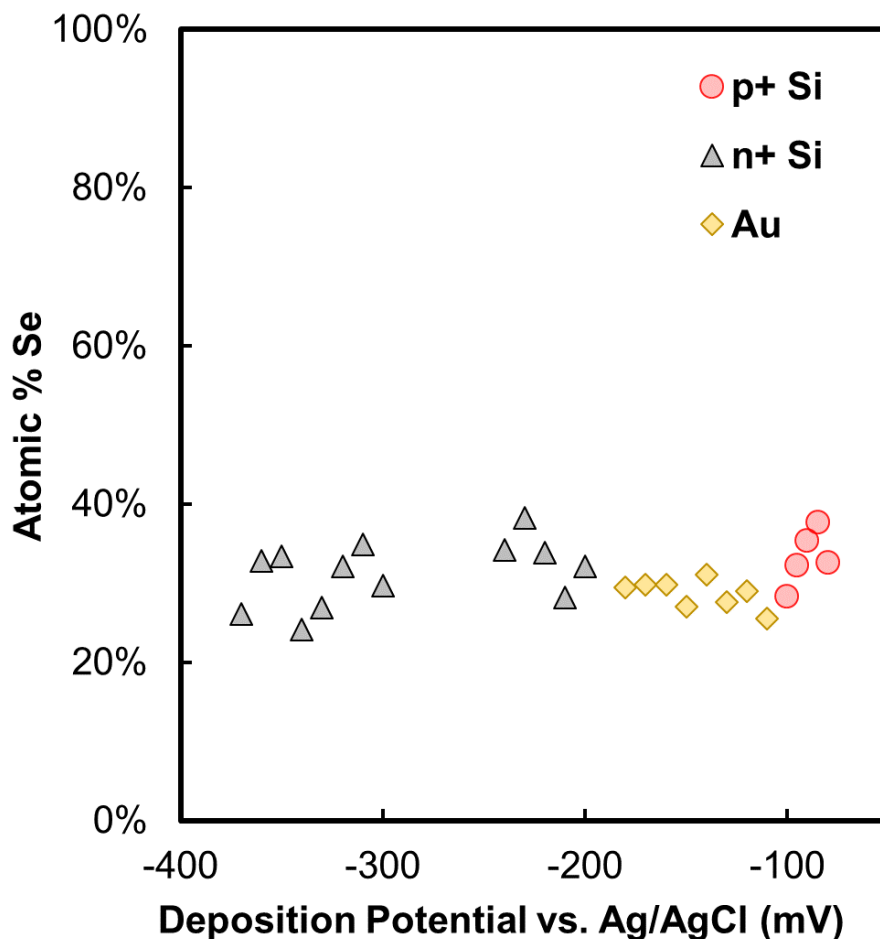
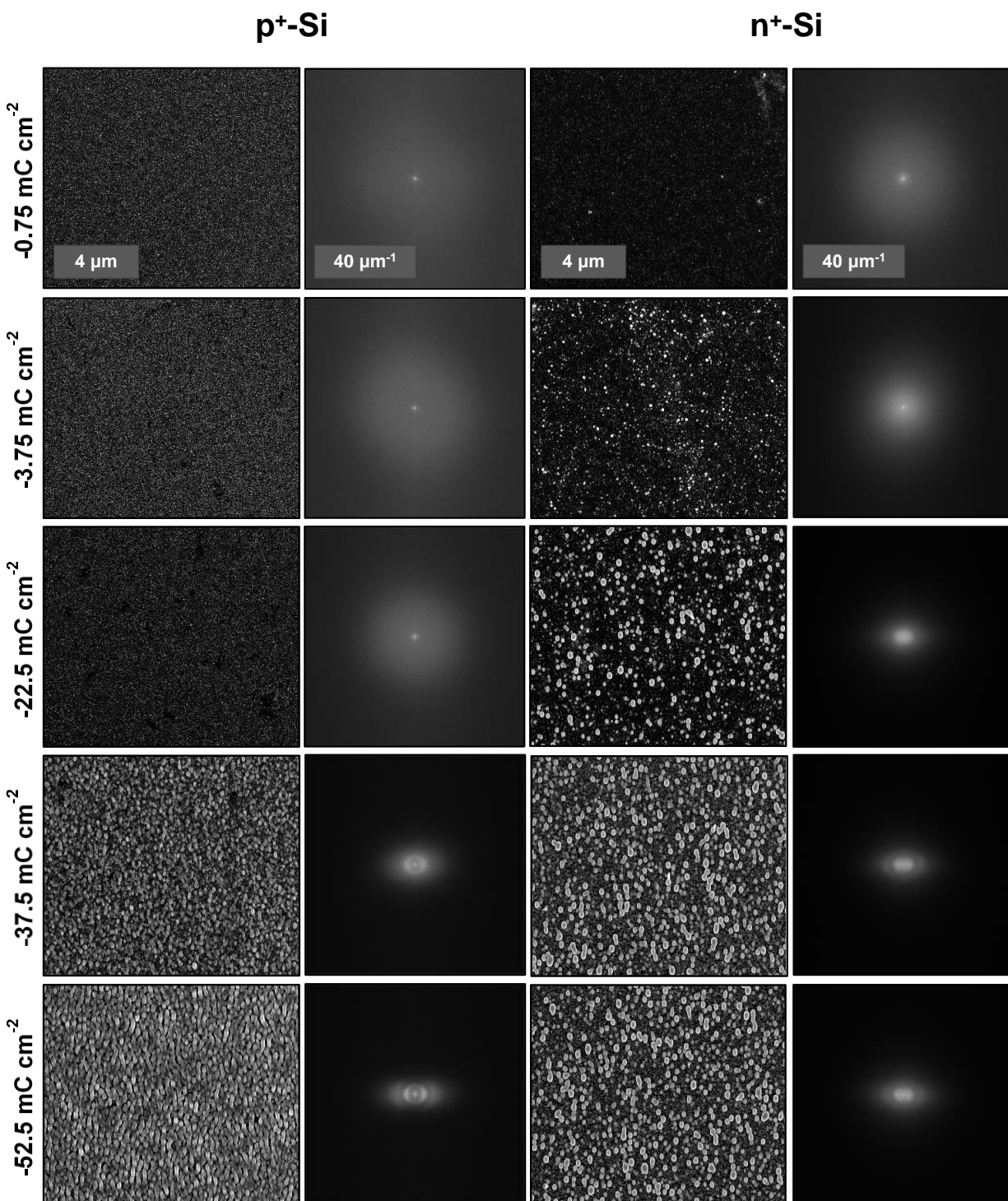


Figure S2.10: Compositional data for phototropic Se-Te films deposited on p⁺-Si, n⁺-Si, and Au substrates obtained via an electron dispersive X-ray spectroscopy (EDS) module installed on a FEI Nova NanoSEM 450 scanning electron microscope (SEM). The atomic percentage of Se was calculated from the measured Se and Te relative abundance. Average Se atomic percentages for Se-Te deposited on each of the substrates were: p⁺-Si, 33.2 ± 3.5 ; n⁺-Si, 31.3 ± 4.0 ; Au, 28.7 ± 1.8 . The differences in observed Se-Te composition on the various tested substrates were not statistically significant.

2.4.8 Extended discussion of Fourier transforms and SEM images in Figure 2.2



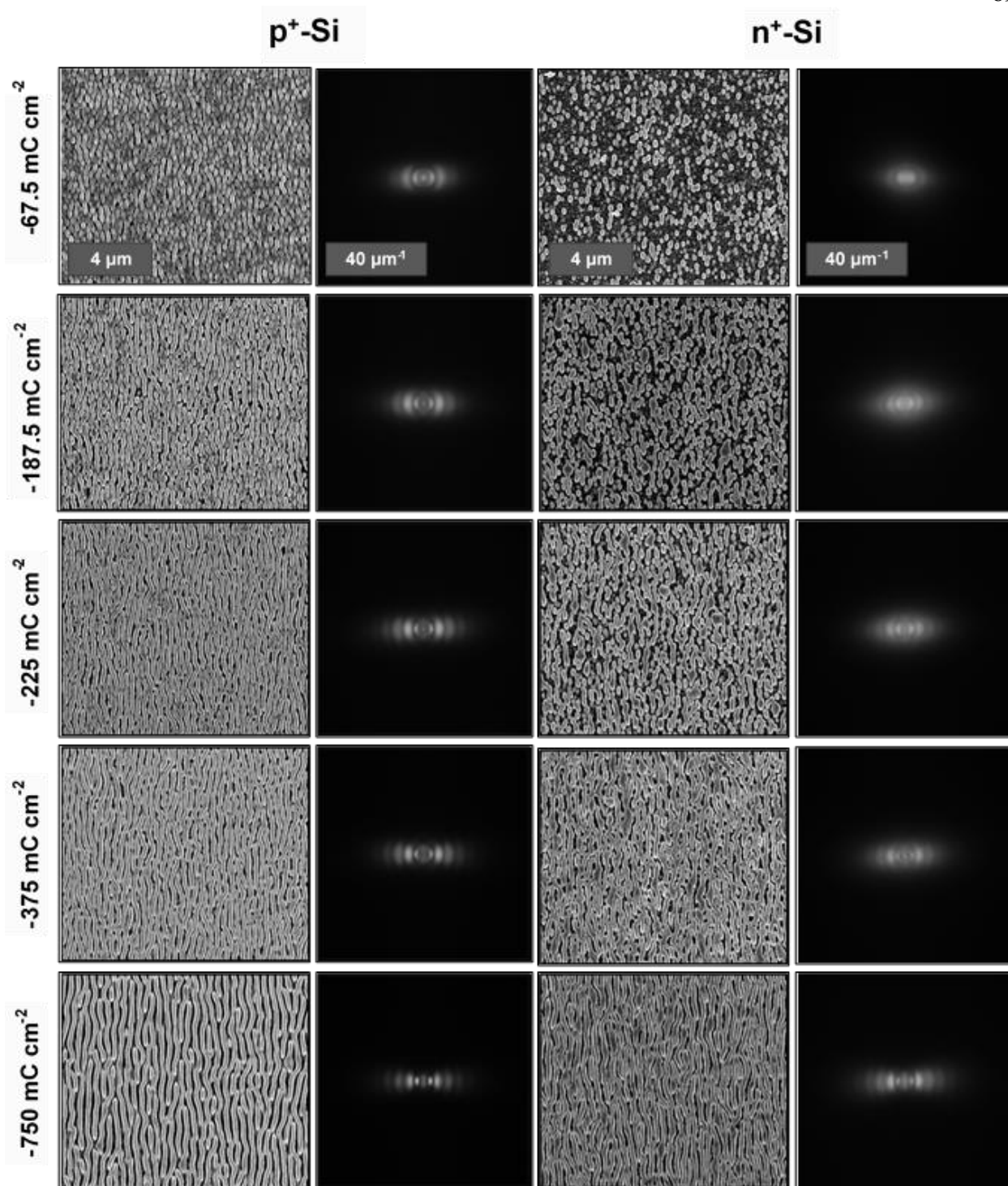


Figure S2.11: SEM images and FT spectra with a higher resolution than those in Figure 2.2 are provided here with additional discussion. After a charge density of -37.5 mC cm^{-2} was passed on p^+-Si and -22.5 mC cm^{-2} was passed on n^+-Si , the nucleates adopted a shape that was elongated in the vertical direction, parallel to the axis of polarization. Though the shape of the nucleates was slightly

anisotropic, the distribution of nucleates was isotropic. In the FT spectra, the isotropic distribution was indicated by a relatively bright symmetric ring of intensity close to the origin, whereas the elliptical shape of the particles was indicated by an ellipse of intensity, elongated in the horizontal direction, i.e., perpendicular to the axis of polarization. This ellipse of intensity in the FT spectra was observed at relatively higher frequencies in reciprocal space than the features representing the distribution of nucleates. Thus, nucleate dimensions were smaller than the average nucleate spacing at this stage of mass addition on both p⁺-Si and n⁺-Si substrates, with relatively smaller nucleate dimensions and spacings observed on p⁺-Si vs. n⁺-Si. The elliptical features in the FT spectra were observed for Se-Te deposits on n⁺-Si until much later stages of mass addition, whereas symmetric horizontal lobes perpendicular to the axis of polarization were observed in FT spectra for deposits on p⁺-Si at earlier levels of mass addition (starting at -53.5 mC cm⁻²), indicating a more fully formed lamellar morphology. At later stages of mass addition on n⁺-Si (-37.5 mC cm⁻² to -187.5 mC cm⁻²), vertical spacing between elliptical nucleates was smaller and nucleates converged into longer lamellae. The smaller vertical nucleate spacing was indicated by a progressively higher frequency response in the FT spectra along the axis of polarization at increased levels of mass addition. At the final stage of mass addition (-750 mC cm⁻²), FT spectra for Se-Te films on p⁺-Si and n⁺-Si were similar, though the lower fidelity in films on n⁺-Si was indicated by broader features with less definition in the FT spectra relative to p⁺-Si which displayed narrower peaks and more defined high-frequency overtones.

2.4.9 Graphical representation of striking potential

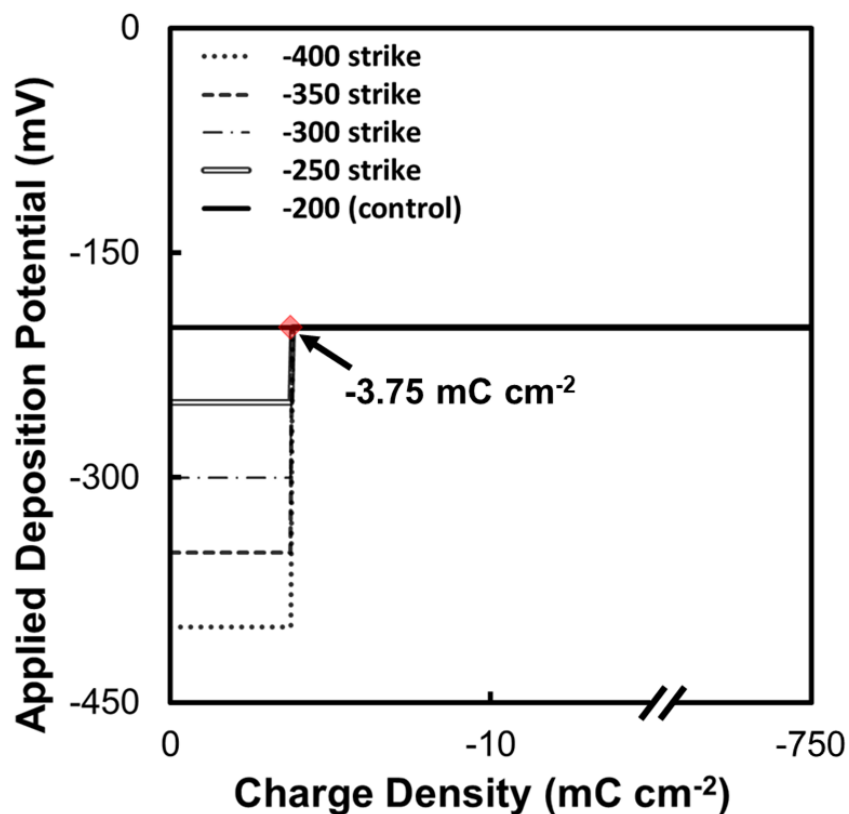


Figure S2.12: Graphical depiction of the experiments in Figure 2.4-2.5 demonstrating the procedure followed during variable-potential depositions performed on n⁺-Si. Over a total charge density passed of -750 mC cm⁻², the initial -3.75 mC cm⁻² of charge was passed under relatively more negatively applied deposition potentials. For n⁺-Si, these “striking” potentials were -400, -350, -300, or -250 mV vs. Ag/AgCl. A control experiment was also performed on n⁺-Si in which the entirety of the -750 mC cm⁻² of charge was passed at -200 mV vs. Ag/AgCl.

2.4.10 Dark growth during Se-Te electrodeposition on n⁺-Si

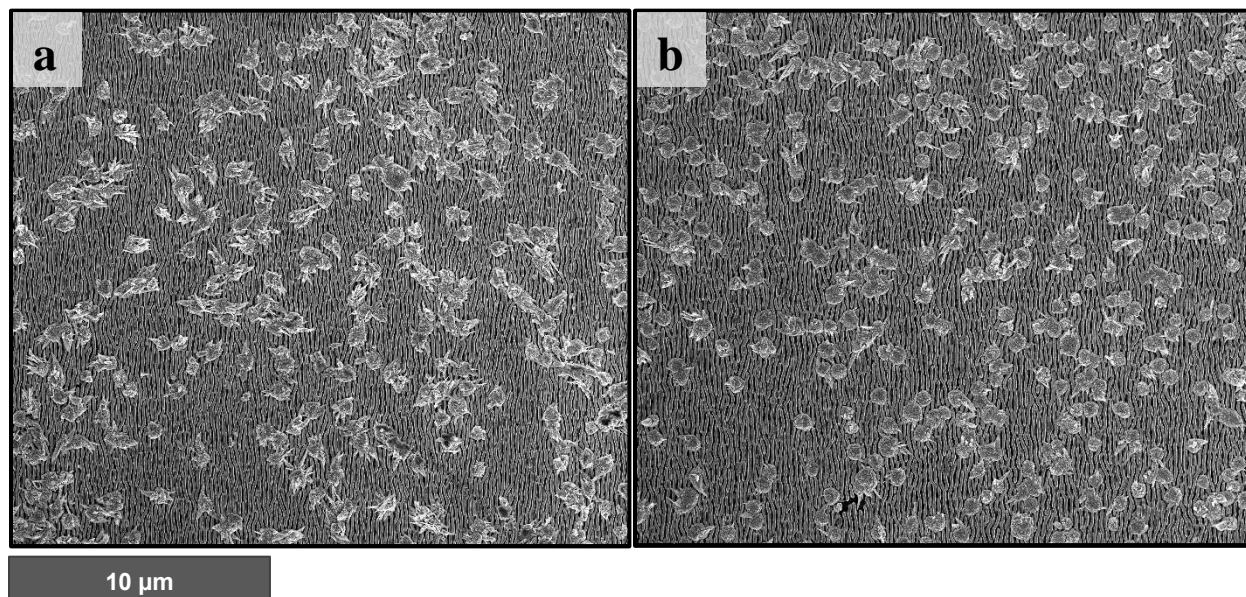


Figure S2.13: Low-magnification SEM images of photoelectrodeposited Se-Te films grown on n⁺-Si at (a) -350 mV and (b) -300 mV vs. Ag/AgCl at a charge density of -750 mC cm⁻² using vertically polarized $\lambda = 927$ nm illumination at a power density of 53 mW cm⁻² at a charge density of -3.75 mC cm⁻². At these deposition potentials, dark growth was a substantial contribution to the deposited film. These SEM images were obtained at a magnification of 6250 X and a resolution of 4096 x 3536 pixels, which corresponded to ~ 85.8 pixels μm^{-1} .

2.4.11 Summary of previous phototropic growth studies

Table S2.1: Summary of selected publications relating to the phototropic growth of Se-Te

Publication	Summary
<p>Sadtler, B.; Burgos, S. P.; Batara, N. A.; Beardslee, J. A.; Atwater, H. A.; Lewis, N. S., Phototropic growth control of nanoscale pattern formation in photoelectrodeposited Se-Te films. <i>Proc Natl Acad Sci U S A</i> 2013, <i>110</i> (49), 19707-12.</p>	<ul style="list-style-type: none"> • Summary of initial findings, introducing the phenomenon of phototropic growth and the optical growth model showing highly anisotropic lamellar morphology in Se-Te electrodeposits when films are deposited under constant illumination from light with a photon energy larger than the optical bandgap of the Se-Te alloy • Descriptions of the relationships of incident illumination's polarization, wavelength, and incident angle to Se-Te photoelectrodeposit morphology, period, and lamellar alignment
<p>Carim, A. I.; Batara, N. A.; Premkumar, A.; Atwater, H. A.; Lewis, N. S., Self-Optimizing Photoelectrochemical Growth of Nanopatterned Se-Te Films in Response to the Spectral Distribution of Incident Illumination. <i>Nano Lett</i> 2015, <i>15</i> (10), 7071-6.</p>	<ul style="list-style-type: none"> • Series of experiments in which two illumination sources with mutually different wavelengths expand on the relationship between spectral input and resulting lamellar period • Se-Te lamellar period is insensitive to illumination source bandwidth • Se-Te lamellar period is determined entirely by intensity-weighted average wavelength of illumination source, as was determined through dual-beam experiments and substantiated by simulation
<p>Carim, A. I.; Batara, N. A.; Premkumar, A.; Atwater, H. A.; Lewis, N. S., Polarization Control of Morphological Pattern Orientation During Light-Mediated Synthesis of Nanostructured Se-Te Films. <i>ACS Nano</i> 2016, <i>10</i> (1), 102-11.</p>	<ul style="list-style-type: none"> • Series of experiments in which two illumination sources with mutually different linear polarizations expand on the relationship between polarization input and resulting lamellar orientation • Lamellar orientation is dependent on the intensity of each illumination sources in dual-beam experiments, substantiated by simulation
<p>Carim, A. I.; Batara, N. A.; Premkumar, A.; May, R.; Atwater, H. A.; Lewis, N. S., Morphological Expression of the Coherence and Relative Phase of Optical Inputs to the Photoelectrodeposition of Nanopatterned Se-Te Films. <i>Nano Lett</i> 2016, <i>16</i> (5), 2963-8.</p>	<ul style="list-style-type: none"> • For Se-Te films deposited under illumination from two sources with mutually orthogonal (or near-orthogonal) linear polarizations, Se-Te photoelectrodeposit morphology depends on relative phase differences, either coherent or incoherent, over relevant coherence length scales • With coherent illumination between both sources, lamellar morphology oriented along the intensity-weighted axis of polarization (combination of both illumination sources' polarization vectors) is observed • With incoherent illumination between both sources, a mesh-type pattern is observed, similar to

	the Se-Te photoelectrodeposit morphology for films deposited under unpolarized illumination
Simonoff, E.; Lichterman, M. F.; Papadantonakis, K. M.; Lewis, N. S., Influence of Substrates on the Long-Range Order of Photoelectrodeposited Se-Te Nanostructures. <i>Nano Lett</i> 2019 , <i>19</i> (2), 1295-1300.	<ul style="list-style-type: none"> • Long range order in Se-Te photoelectrodeposits is dependent on growth substrate (p^+-Si or n^+-Si) • Se-Te work function alignment with different substrates creates interfacial electrical junctions with different current-voltage behaviors • Straighter, less defective lamellar patterns are observed in Se-Te films photoelectrodeposited on substrates exhibiting a linear, ohmic current-voltage behavior (i.e., p^+-Si) while less straight, more defective lamellar patterns are observed in Se-Te films photoelectrodeposited on substrates exhibiting non-linear current-voltage behavior (i.e., n^+-Si)

2.4.12 Se-Te on Au substrates

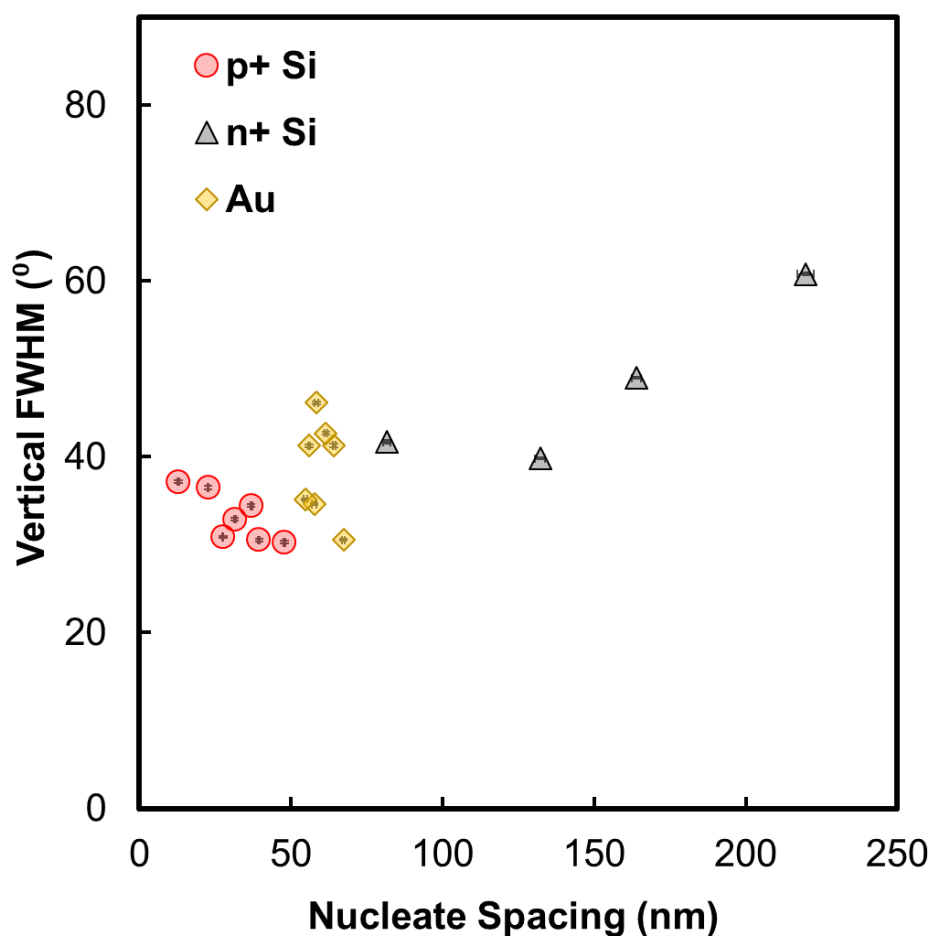


Figure S2.14: Plot showing the pattern fidelity of phototropically grown Se-Te films described by the vertical (parallel to the axis of polarization) FWHM of the primary peak in the 2D FT of imaged Se-Te films (y-axis) at conditions which produced a given nucleate spacing (x-axis). Points in this plot for p^+ -Si and n^+ -Si are identical to Figure 2.3 in the main text; this plot also includes points for phototropic Se-Te films deposited on Au substrates. Similar to Figure 2.3, the films that were analyzed to obtain values for the lamellar period and vertical FWHM were deposited at a charge density of -750 mC cm^{-2} . Vertical FWHM values are paired with corresponding particle spacing values that share applied deposition potentials ranging from -110 to $-170 \text{ mV vs. Ag/AgCl}$ for Se-Te films deposited on Au substrates. The average fidelity of phototropic Se-Te films on Au substrates generally agrees with the expected trend of increased fidelity resulting from smaller nucleate spacings.

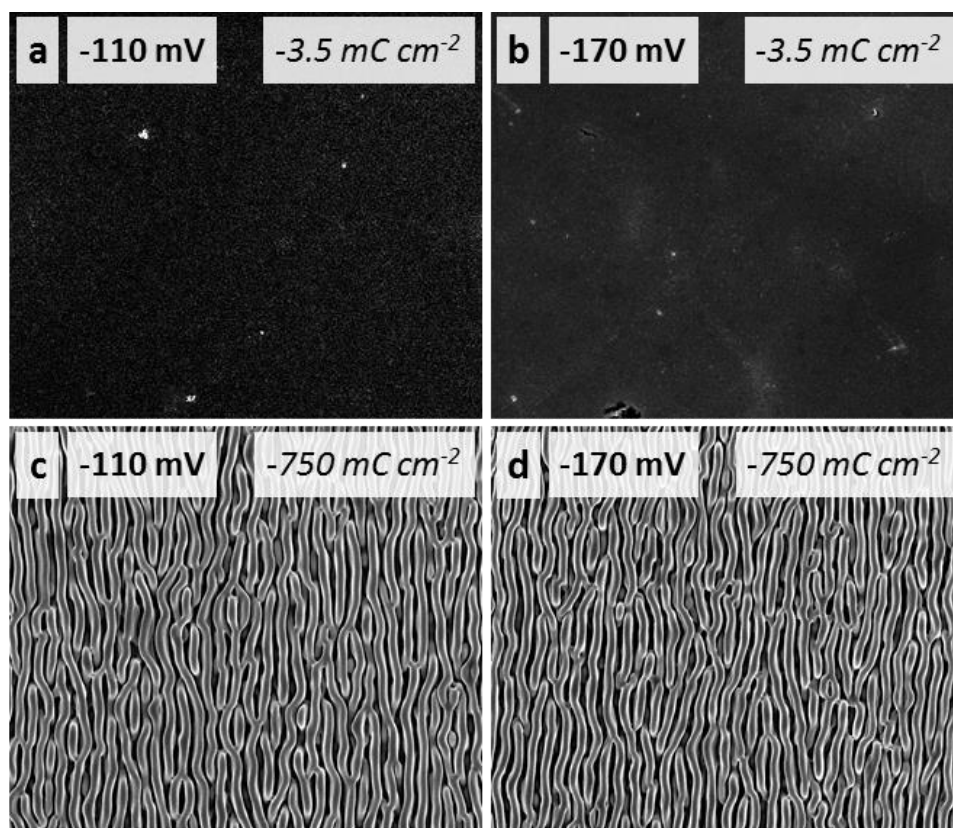


Figure S2.15: SEM images demonstrating representative phototropic Se-Te films grown on Au substrates at a charge density of (a), (b) -3.5 mC cm^{-2} and (c), (d) -750 mC cm^{-2} . During the deposition, the Au substrates were illuminated by vertically polarized light from a narrow-band LED with $\lambda = 927 \text{ nm}$ at a power density of 53 mW cm^{-2} . Samples in (a), (c) were deposited at $-110 \text{ mV vs. Ag/AgCl}$ and samples in (b), (d) were deposited at $-170 \text{ mV vs. Ag/AgCl}$. The potentials applied constitute the range of the applied deposition potentials in which stable phototropic growth is accessible on Au substrates at the conditions tested. The morphology of Se-Te nucleates is best

described as a smooth, thin film. No substantial potential dependence was observed for Se-Te nucleate spacing on Au substrates, as can be observed visually in (a) and (b). Similarly, the results of Fourier analysis of nucleated Se-Te films on Au exhibited a relatively small range of nucleate spacings, as observed in Figure S2.14.

2.5 References

1. Ito, T.; Okazaki, S., Pushing the limits of lithography. *Nature* **2000**, *406* (6799), 1027-31.
2. Martinsson, H., Current status of optical maskless lithography. *Journal of Micro/Nanolithography, MEMS, and MOEMS* **2005**, *4* (1), 011003.
3. Van den Hove, L.; Wong, A. K. K.; Ferguson, R. A.; Liebmann, L. W.; Mansfield, S. M.; Molless, A. F.; Neisser, M. O., Lithographic effects of mask critical dimension error. **1998**, *3334*, 106.
4. Postnikov, S.; Hector, S.; Garza, C.; Peters, R.; Ivin, V., Critical dimension control in optical lithography. *Microelectronic Engineering* **2003**, *69* (2-4), 452-458.
5. Groves, T. R., Statistics of pattern placement errors in lithography. *Journal of Vacuum Science & Technology B: Microelectronics and Nanometer Structures* **1991**, *9* (6), 3555.
6. Soh, H. T.; Guarini, K. W.; Quate, C. F., Introduction to Scanning Probe Lithography. **2001**, *7*, 1-22.
7. Wang, Z.; Tan, J.; Zou, Q.; Jiang, W., Mechanical-plowing-based high-speed patterning on hard material via advanced-control and ultrasonic probe vibration. *Rev Sci Instrum* **2013**, *84* (11), 113704.
8. Gordon, C. G., Generic criteria for vibration-sensitive equipment. *Proc. SPIE* **1992**, *1619*, 71-85.
9. Khoo, I.-C.; Chigrinov, V. G.; Kwok, H.; Yip, W. C.; Kozenkov, V. M.; Prudnikova, E. K.; Tang, B. Z.; Salhi, F., New photo-aligning and photo-patterning technology: superthin internal polarizers, retarders, and aligning layers. *Proc. SPIE* **2001**, *4463*, 117.
10. Song, X.; Fu, D.; Shah, S.; Reif, J., UV-Micropatterned Miniaturization: Rapid In Situ Photopatterning and Miniaturization of Microscale Features on Shrinkable Thermoplastics. *Advanced Materials Technologies* **2020**, 2000146.
11. Schmuki, P.; Erickson, L. E., Selective high-resolution electrodeposition on semiconductor defect patterns. *Phys Rev Lett* **2000**, *85* (14), 2985-8.
12. Bera, D.; Kuiry, S. C.; Seal, S., Synthesis of nanostructured materials using template-assisted electrodeposition. *Jom* **2004**, *56* (1), 49-53.
13. Liu, J.; Wernette, D. P.; Lu, Y., Proofreading and error removal in a nanomaterial assembly. *Angew Chem Int Ed Engl* **2005**, *44* (44), 7290-3.
14. Carim, A. I.; Hamann, K. R.; Batara, N. A.; Thompson, J. R.; Atwater, H. A.; Lewis, N. S., Template-free synthesis of periodic three-dimensional PbSe nanostructures via photoelectrodeposition. *J Am Chem Soc* **2018**, *140* (21), 6536-6539.

15. Carim, A. I.; Batara, N. A.; Premkumar, A.; Atwater, H. A.; Lewis, N. S., Self-Optimizing Photoelectrochemical Growth of Nanopatterned Se-Te Films in Response to the Spectral Distribution of Incident Illumination. *Nano Lett* **2015**, *15* (10), 7071-6.
16. Carim, A. I.; Batara, N. A.; Premkumar, A.; Atwater, H. A.; Lewis, N. S., Polarization Control of Morphological Pattern Orientation During Light-Mediated Synthesis of Nanostructured Se-Te Films. *ACS Nano* **2016**, *10* (1), 102-11.
17. Sadtler, B.; Burgos, S. P.; Batara, N. A.; Beardslee, J. A.; Atwater, H. A.; Lewis, N. S., Phototropic growth control of nanoscale pattern formation in photoelectrodeposited Se-Te films. *Proc Natl Acad Sci U S A* **2013**, *110* (49), 19707-12.
18. Carim, A. I.; Batara, N. A.; Premkumar, A.; May, R.; Atwater, H. A.; Lewis, N. S., Morphological Expression of the Coherence and Relative Phase of Optical Inputs to the Photoelectrodeposition of Nanopatterned Se-Te Films. *Nano Lett* **2016**, *16* (5), 2963-8.
19. Majidi, H.; Van, K. T.; Baxter, J. B., Nucleation and Growth of Extremely Thin CdSe Films Electrodeposited from Near-Neutral Electrolytes. *Journal of The Electrochemical Society* **2012**, *159* (10), D605-D610.
20. Hamann, K. R.; Carim, A. I.; Meier, M. C.; Thompson, J. R.; Batara, N. A.; Yermolenko, I. S.; Atwater, H. A.; Lewis, N. S., Optically tunable mesoscale CdSe morphologies via inorganic phototropic growth. *Journal of Materials Chemistry C* **2020**.
21. Yi, S.; Zhu, Z.; Cai, X.; Jia, Y.; Cho, J. H., The Nature of Bonding in Bulk Tellurium Composed of One-Dimensional Helical Chains. *Inorg Chem* **2018**, *57* (9), 5083-5088.
22. Springborg, M.; Jones, R. O., Sulfur and selenium helices: Structure and electronic properties. *The Journal of Chemical Physics* **1988**, *88* (4), 2652-2658.
23. Scharifker, B.; Hills, G., Theoretical and experimental studies of multiple nucleation. *Electrochimica Acta* **1983**, *28* (7), 879-889.
24. Morin, S.; Lachenwitzer, A.; Magnussen, O. M.; Behm, R. J., Potential-Controlled Step Flow to 3D Step Decoration Transition: Ni Electrodeposition on Ag(111). *Physical Review Letters* **1999**, *83* (24), 5066-5069.
25. Oskam, G.; Long, J. G.; Natarajan, A.; Searson, P. C., Electrochemical deposition of metals onto silicon. *Journal of Physics D: Applied Physics* **1998**, *31* (16), 1927-1949.
26. Paunovic, M., Electrochemical Deposition. In *Encyclopedia of Electrochemistry*, Bard, A. J.; Stratmann, M., Eds. Wiley-VCH Verlag GmbH & Co. KGaA: Weinheim, 2007.
27. Radisic, A.; Vereecken, P. M.; Searson, P. C.; Ross, F. M., The morphology and nucleation kinetics of copper islands during electrodeposition. *Surface Science* **2006**, *600* (9), 1817-1826.
28. Guo, L.; Searson, P. C., On the influence of the nucleation overpotential on island growth in electrodeposition. *Electrochimica Acta* **2010**, *55* (13), 4086-4091.
29. Palomar-Pardavé, M.; Scharifker, B. R.; Arce, E. M.; Romero-Romo, M., Nucleation and diffusion-controlled growth of electroactive centers. *Electrochimica Acta* **2005**, *50* (24), 4736-4745.

30. Krumm, R.; Guel, B.; Schmitz, C.; Staikov, G., Nucleation and growth in electrodeposition of metals on n-Si(111). *Electrochimica Acta* **2000**, *45* (20), 3255-3262.
31. Sharma, A. K., Electrodeposition of gold on magnesium-lithium alloys. *Metal Finishing* **1988**, *86* (12), 33-34.
32. Bewick, A.; Fleischmann, M.; Thirsk, H. R., Kinetics of the electrocrystallization of thin films of calomel. *Transactions of the Faraday Society* **1962**, *58*, 2200.
33. Ivanova, Y. A.; Ivanou, D. K.; Streltsov, E. A., Electrochemical deposition of PbTe onto n-Si(100) wafers. *Electrochemistry Communications* **2007**, *9* (4), 599-604.
34. Bijani, S.; Schreiber, R.; Dalchiele, E. A.; Gabas, M.; Martinez, L.; Ramos-Barrado, J. R., Study of the Nucleation and Growth Mechanisms in the Electrodeposition of Micro- and Nanostructured Cu₂O Thin Films. *J Phys Chem C* **2011**, *115* (43), 21373-21382.
35. Phillips, R. J.; Shane, M. J.; Switzer, J. A., Electrochemical and photoelectrochemical deposition of thallium(III) oxide thin films. *Journal of Materials Research* **2011**, *4* (4), 923-929.
36. Tan, C.; Qin, C.; Sadtler, B., Light-directed growth of metal and semiconductor nanostructures. *Journal of Materials Chemistry C* **2017**, *5* (23), 5628-5642.
37. Lowe, James M.; Yan, Q.; Benamara, M.; Coridan, R. H., Direct photolithographic patterning of cuprous oxide thin films via photoelectrodeposition. *J. Mater. Chem. A* **2017**, *5* (41), 21765-21772.
38. Lancaster, M.; Mow, R.; Liu, J.; Cheek, Q.; MacInnes, M. M.; Al-Jassim, M. M.; Deutsch, T. G.; Young, J. L.; Maldonado, S., Protection of GaInP₂ Photocathodes by Direct Photoelectrodeposition of MoS_x Thin Films. *ACS Appl Mater Interfaces* **2019**, *11* (28), 25115-25122.
39. Windheim, J. v.; Darkowski, A.; Cocivera, M., Photoelectrochemical deposition and properties of thin-film cadmium telluride. *Canadian Journal of Physics* **1987**, *65* (8), 1053-1059.
40. Simonoff, E.; Lichterman, M. F.; Papadantonakis, K. M.; Lewis, N. S., Influence of Substrates on the Long-Range Order of Photoelectrodeposited Se-Te Nanostructures. *Nano Lett* **2019**, *19* (2), 1295-1300.
41. Dasog, M.; Carim, A. I.; Yalamanchili, S.; Atwater, H. A.; Lewis, N. S., Profiling Photoinduced Carrier Generation in Semiconductor Microwire Arrays via Photoelectrochemical Metal Deposition. *Nano Lett* **2016**, *16* (8), 5015-21.
42. Qin, C.; Campbell, B. M.; Shen, M.; Zhao, T.; Sadtler, B., Light-Driven, Facet-Selective Transformation of Cuprous Oxide Microcrystals to Hollow Copper Nanoshells. *Chemistry of Materials* **2019**, *31* (19), 8000-8011.
43. Ogata, Y.; Kobayashi, K.; Motoyama, M., Electrochemical metal deposition on silicon. *Current Opinion in Solid State and Materials Science* **2006**, *10* (3-4), 163-172.

44. Hubert, C.; Fiorini-Debuisschert, C.; Maurin, I.; Nunzi, J. M.; Raimond, P., Spontaneous Patterning of Hexagonal Structures in an Azo-Polymer Using Light-Controlled Mass Transport. *Advanced Materials* **2002**, *14* (10), 729.
45. Bonse, J.; Krüger, J.; Höhm, S.; Rosenfeld, A., Femtosecond laser-induced periodic surface structures. *Journal of Laser Applications* **2012**, *24* (4), 042006.
46. Chen, G.; Cong, Q.; Feng, Y.; Ren, L., Study on the wettability and self-cleaning of butterfly wing surfaces. In *Design and Nature II*, Collins, M. W.; Brebbia, C. A., Eds. WIT Press: Southampton (United Kingdom) and Billerica (Massachusetts), 2004; pp 245-251.
47. Sun, G.; Fang, Y.; Cong, Q.; Ren, L.-q., Anisotropism of the Non-Smooth Surface of Butterfly Wing. *Journal of Bionic Engineering* **2009**, *6* (1), 71-76.
48. Kinoshita, S.; Yoshioka, S.; Fujii, Y.; Okamoto, N., Photophysics of structural color in the Morpho butterflies. *Forma* **2002**, *17*, 103-121.
49. Martínez-Calderon, M.; Rodríguez, A.; Dias-Ponte, A.; Morant-Miñana, M. C.; Gómez-Aranzadi, M.; Olaizola, S. M., Femtosecond laser fabrication of highly hydrophobic stainless steel surface with hierarchical structures fabricated by combining ordered microstructures and LIPSS. *Applied Surface Science* **2016**, *374*, 81-89.
50. Long, J.; Fan, P.; Zhong, M.; Zhang, H.; Xie, Y.; Lin, C., Superhydrophobic and colorful copper surfaces fabricated by picosecond laser induced periodic nanostructures. *Applied Surface Science* **2014**, *311*, 461-467.
51. Finch, C.; Shocksolution_Examples, (2020), GitHub repository, https://github.com/cfinch/Shocksolution_Examples

CHAPTER III

Pre-seeded Optical Scatterers as a Template for Phototropic Growth

Simonoff, E.; Thompson, J. R.; Meier, M. C.; Kennedy, K.; Hamann, K. R.; Lewis, N.S., *Manuscript in Preparation*.

3.1 Introduction

Selective and directed growth of materials can be enabled through physical or chemical templating to yield anisotropy in morphology and function. For instance, in a process similar to nanosphere lithography,¹ selective through-pore electrodeposition of zirconia can be accomplished by physically blocking electrolyte contact at an otherwise conductive working electrode surface via a colloidal monolayer of polystyrene beads.² Chemical functionalization can also provide a means for variation in conductivity and reactivity across a substrate, able to be achieved through soft lithography³ or microcontact printing.⁴ In contrast to physically blocked or chemically modified surfaces, electrodeposition of metals can be directed selectively onto silicon microstructures as a result of work function, band conduction, and illumination conditions.⁵ Similarly, nickel electrical contacts can be selectively electrodeposited onto silicon nanowires, seeded by Au electrodes.⁶

Pre-seeding growth substrates can also improve performance or ensure proper development of deposited films. Epitaxial growth of GaN requires pre-seeding aluminum on silicon prior to nitriding⁷⁻⁸ and epitaxial growth of PbTiO₃ on LaAlO₃ is much improved by pre-seeding with Pb-Ti double alkoxide.⁹ Diamond films formed on silicon substrates via microwave plasma chemical vapor deposition (MPCVD) demonstrate improved emission current when substrates are pre-seeded with

nanoscale diamond powder.¹⁰ Solar cell conversion efficiency for multi-crystalline silicon (mc-Si) cells was improved when ingots were grown with mc-Si seeds.¹¹ In chemical vapor deposition (CVD) of silicon, a crystalline silicon substrate acts as a template for crystalline growth, directed by the placement of metal catalysts, as in the vapor-liquid-solid (VLS) process by which crystalline (111)-oriented silicon microwires are grown.¹² A similar, solution-based technique produces TiO₂ nanowires, seeded by ceria nanoparticles dispersed in a solution containing Ti(SO₄)₂.¹³

Furthermore, templating can contribute to increased levels of anisotropy in grown materials. In a mild hydrothermal process, pre-seeding substrates with ZnO particles led to an increase in the aspect ratio of epitaxially grown ZnO nanorods.¹⁴⁻¹⁶ Development of anisotropy in a material can also be controlled by chemical templating which can achieve facet-selective growth or etching, especially in crystalline material. In contrast to the nanowires normally obtained in the template-assisted electrodeposition of nickel, inclusion of boric acid leads to formation of nickel nanotubes.¹⁷ In the presence of chemical additives such as sodium dodecyl sulfate (SDS) or copper nitrate, electrodeposited cuprous oxide exhibits facet selective growth during bottom-up synthesis.¹⁸ In a top-down etching procedure, Au microcrystals can be selectively etched in either the (100) or (111) direction with silver tetraoctylammonium bromide (AgToABr) or Cu(Cl)₂, respectively.¹⁹

Mass availability,²⁰⁻²¹ pH,²² growth kinetics,²³ heat flux,²⁴ local light absorption,²⁵⁻²⁶ applied deposition potential during electrodeposition,^{18, 27} and other conditions can also produce anisotropy in developing materials. We recently described the phototropic growth phenomenon, in which highly anisotropic lamellae are formed from Se-Te,²⁸⁻³³ PbTe,³⁴ and CdSe³⁵ as a result of local light absorption during photoelectrochemical deposition. Phototropic growth of these semiconducting materials occurs via a single-step process that involves no chemical or physical templating;

nanostructured films are grown from an optically isotropic solution onto an optically isotropic electrode substrate. The lamellar morphology is formed spontaneously and there is no requirement for coherency of the optical input. Optical modeling and simulations of the phototropic growth process have demonstrated that the high aspect ratio lamellae formed in phototropically grown films are a result of a feedback loop initiated by incident light scattered off of an initially dark and isotropic distribution of nucleated particles. This optical dipole scattering results in localized light absorption in the tips of the emerging lamellae, leading to an equilibrium lamellar morphology.

As previously specified, this process requires no templating in order to achieve the highly anisotropic, high aspect ratio features. Nevertheless, phototropically grown films can demonstrate low pattern fidelities and an apparent limit to the “straightness” of lamellar features.³² Herein we explore the effect of pre-seeded optical scatterers (in the form of a physically templated substrate) on the phototropic growth process and the fidelity, period, and orientation of the resulting patterns.

3.2 Results and Discussion

Figure 3.1a shows a representative scanning electron microscope (SEM) image of a phototropically grown Se-Te film deposited potentiostatically onto a Pt substrate. All films (including the film shown in Figure 3.1a) were deposited under normally incident vertically polarized light from a narrow-band LED with $\lambda_{\text{avg}} = 630 \text{ nm}$ at a power density of 50 mW cm^{-2} . Applied deposition potential was $-100 \text{ mV vs. Ag/AgCl}$ and depositions were carried out until a charge density of -750 mC cm^{-2} had been reached. Figure 3.1b shows a section of a 2D Fourier transform (2D FT) spectrum of a large-area SEM image of the film in Figure 3.1a.

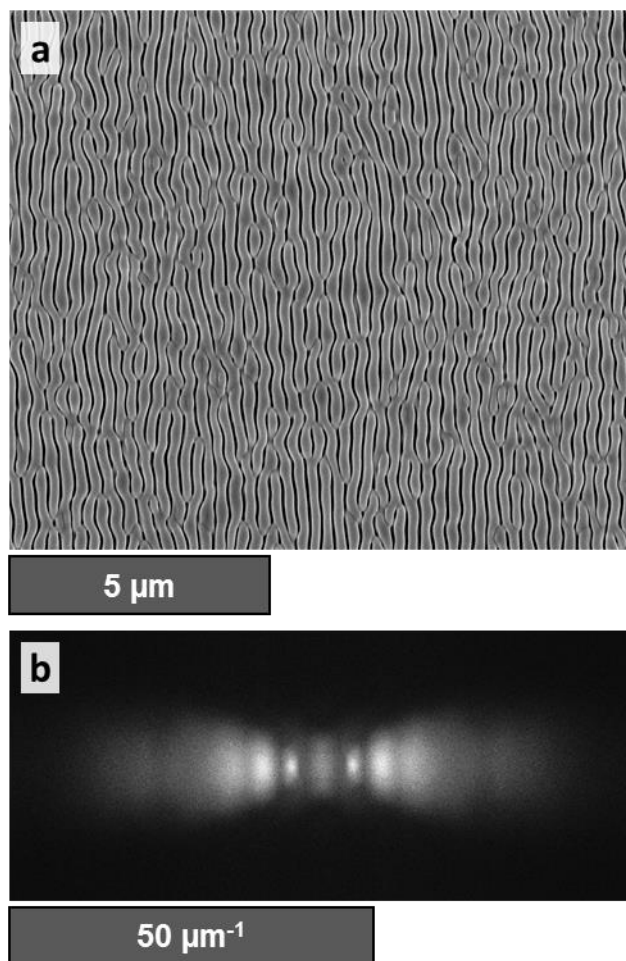


Figure 3.1. (a) Representative SEM image of phototropically grown Se-Te film deposited on Pt-coated n⁺-Si substrate with Ti interlayer. (b) 2D FT spectrum generated from large-area SEM image of film in (a).

In a 2D FT spectrum, a real-space image is converted to frequency (reciprocal) space. Phase information may be preserved but is not obvious or straightforward to represent. The 2D FT spectra in this study are used solely in the analysis of frequency so phase information is not considered. The features in the 2D FT spectra correspond to the frequency of white value in the real-space images obtained. The white value is assumed to be representative of mass and z-height in the SEM images and thus, features in the 2D FT spectra can be analyzed to understand how mass is arranged in real space. In a 2D FT spectrum, the distance between the origin (center of the spectrum) and intensity

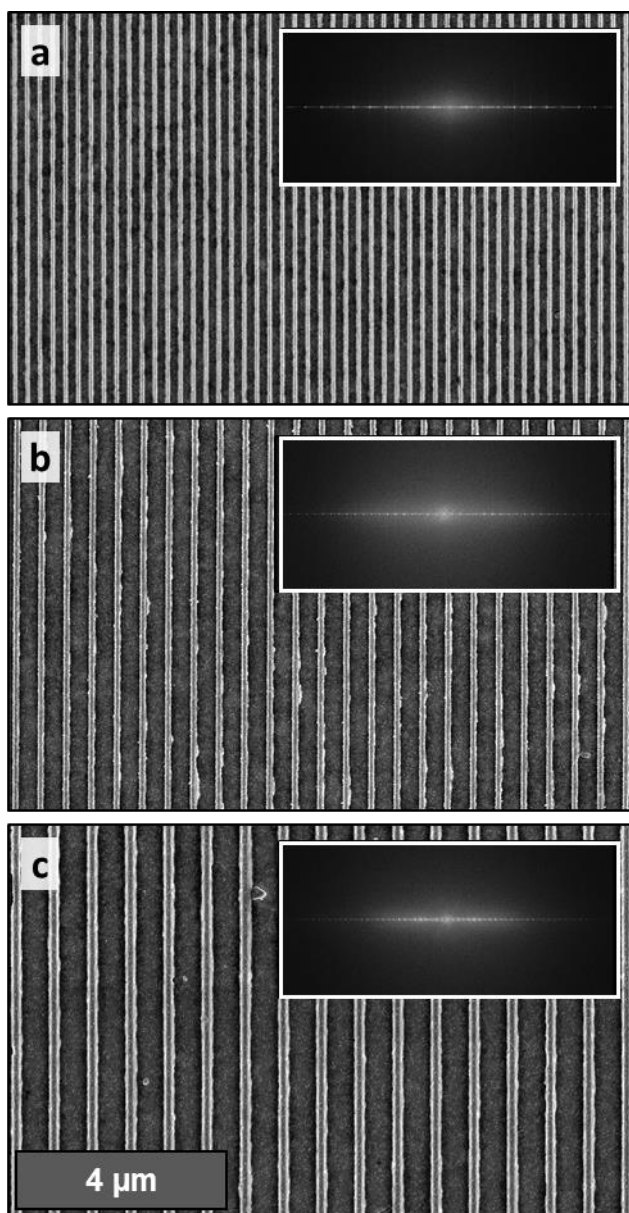


Figure 3.2. SEM images of templated substrates demonstrating ~ 100 nm wide platinum ridges spaced at (a) 242 nm, (b) 484 nm, and (c) 726 nm. Inset images correspond to 2D FT of large-area images of substrates in (a), (b), and (c), respectively. Inset width is $85 \mu\text{m}^{-1}$.

at an arbitrary point is inversely proportional to distance in the real-space image. The vector between the origin and that intensity corresponds to the orientation of spacing present in the real-space image.

Thus, in Figure 3.1b, features in the 2D FT spectrum correspond to both orientation and period of

the patterns present in Figure 3.1a. Lorentzian fits to surface profiles of the primary peaks in 2D FT spectra can be used to determine pattern fidelity (straightness) and period (average spacing).

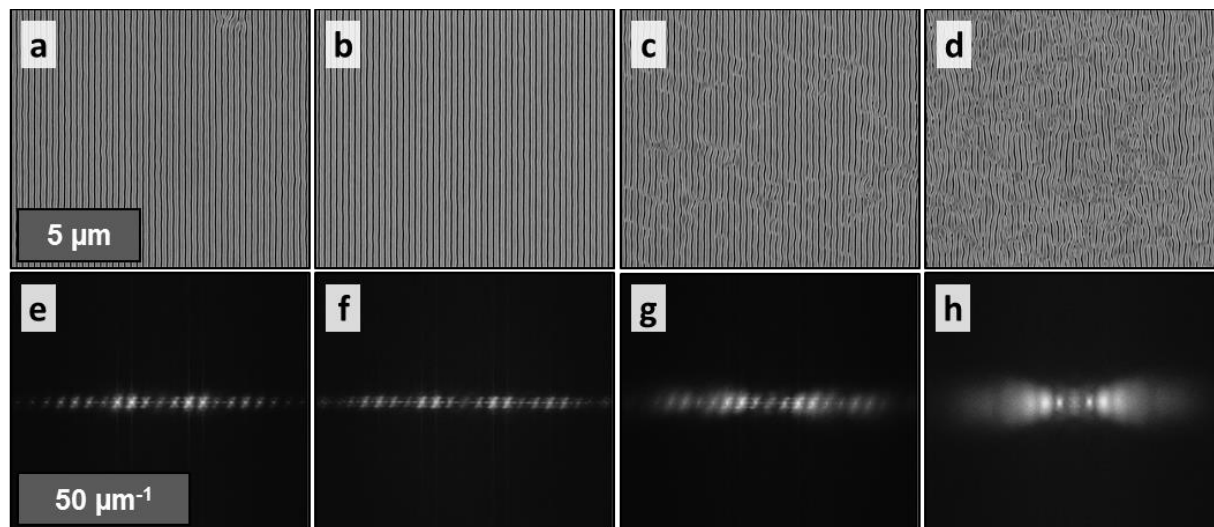


Figure 3.3. Representative SEM images of phototropically grown Se-Te films deposited on templated substrates with a platinum ridge spacing of (a) 242 nm, (b) 484 nm, and (c) 726 nm. Se-Te film in (d) is deposited on Pt with no templating. 2D FT spectra in (e)-(h) are generated from large-area SEM images of the films in (a)-(d), respectively.

Figure 3.2 shows SEM images of templated substrates. The vertically oriented features are Pt ridges on a Pt-coated n^+ -Si substrate with a Ti interlayer fabricated via electron beam lithography and electron beam evaporation. The ridges are approximately 100 nm wide by 100 nm tall and are spaced at 242 nm (Figure 3.2a), 484 nm (Figure 3.2b), and 726 nm (Figure 3.2c). The spacing of platinum ridges corresponds to 1x, 2x, and 3x the expected period for phototropic growth of Se-Te lamellae grown with 630 nm illumination using an index of refraction, n , of ~ 1.3 for the deposition solution and growth medium (corresponding to the theoretical and observed trend of period = $\lambda/2n$).²⁸⁻³¹ Inset images in Figure 3.2 are sections of 2D FT spectra of large-area SEM images of the respective films. In contrast to Figure 3.1b, features in the 2D FT in Figure 3.2 are confined vertically, indicative of the more vertically aligned and much straighter features on the templated

substrates. The discontinuity and regular undulation of the lamellar morphology in Figure 3.1a contribute to substantial broadening of features in the 2D FT in Figure 3.1b.

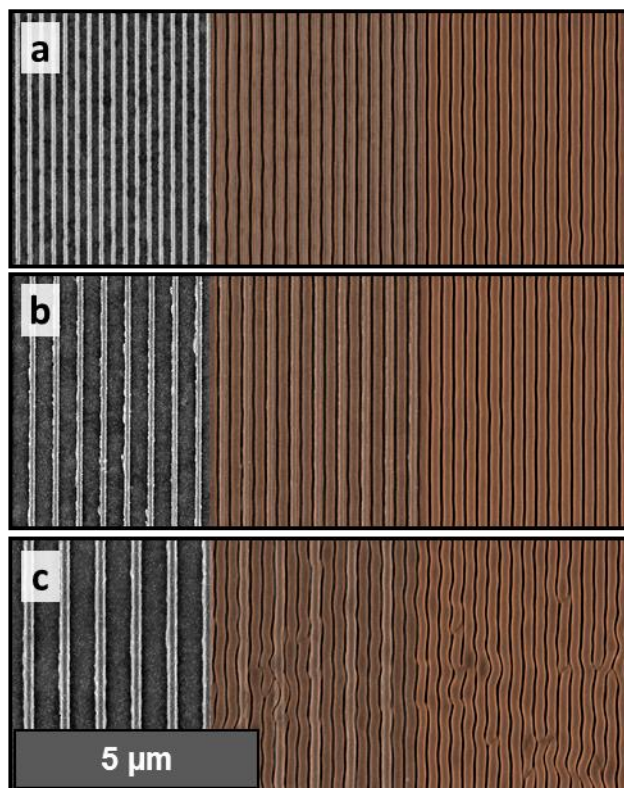


Figure 3.4. SEM images of templated substrates (left panels) and resulting templated phototropic growth (in orange, right panels). Center panels are overlaid portions of the left and right panels, demonstrating the effect and spacing of the underlying templates. Spacing of platinum ridges on the templated substrates is (a) 242 nm, (b) 484 nm, and (c) 726 nm.

Figure 3.3 shows SEM images of representative regions of Se-Te films deposited on templated substrates with the same spacing as those in Figure 3.2. The films shown in Figure 3.3 were all deposited on one sample that had several patterned and unpatterned regions. Thus, the films were deposited under nominally and locally identical conditions. The film shown in the SEM image in Figure 3.3d corresponds to an unpatterned region optically isolated (spacing $\gg 10 \lambda$) and

physically far from the patterned regions imaged in Figure 3.3a-c. 2D FT spectra in Figure 3.3e-h were generated from large-area SEM images of the films in Figure 3.3a-d, respectively.

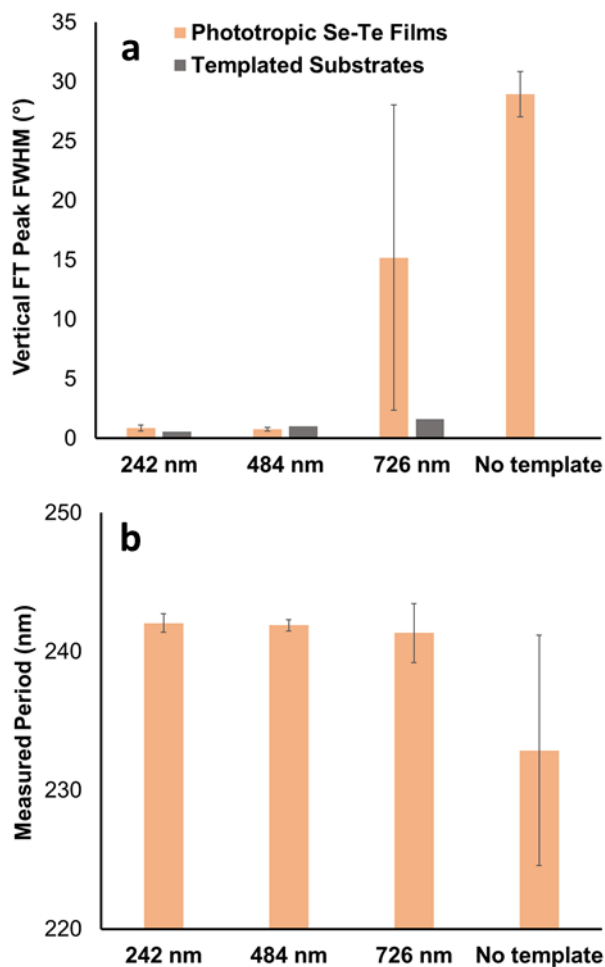


Figure 3.5. Charts showing (a) pattern fidelity and (b) measured period of templated and non-templated phototropically grown Se-Te films. Pattern fidelity in (a) is calculated as the angular FWHM of the primary peak in the 2D FT spectra generated from large-area images of the respective films. Pattern period in (b) is calculated from the primary peak position in the respective 2D FT spectra.

The SEM images and 2D FT spectra in Figure 3.3 illustrate the increased pattern fidelity physically templated substrates impart on phototropically grown Se-Te films relative to non-templated substrates. In particular, the films in Figure 3.3a and b show little or no defects and display

excellent vertical alignment. The films' high fidelity is also demonstrated by the extremely sharp features in the 2D FT spectra in Figure 3.3e and f. The film in Figure 3.3c is slightly defective with some discontinuity and branching of the lamellar morphology. The defective nature of the film is also revealed in the broadening and lower definition of features in the 2D FT spectrum in Figure 3.3g. Nonetheless, all of the templated phototropically grown films demonstrated improved fidelity compared to the non-templated film in Figure 3.3d. The 2D FT spectra of the templated films also demonstrated highly defined and localized features compared to the relatively broad peaks observed in Figure 3.3h.

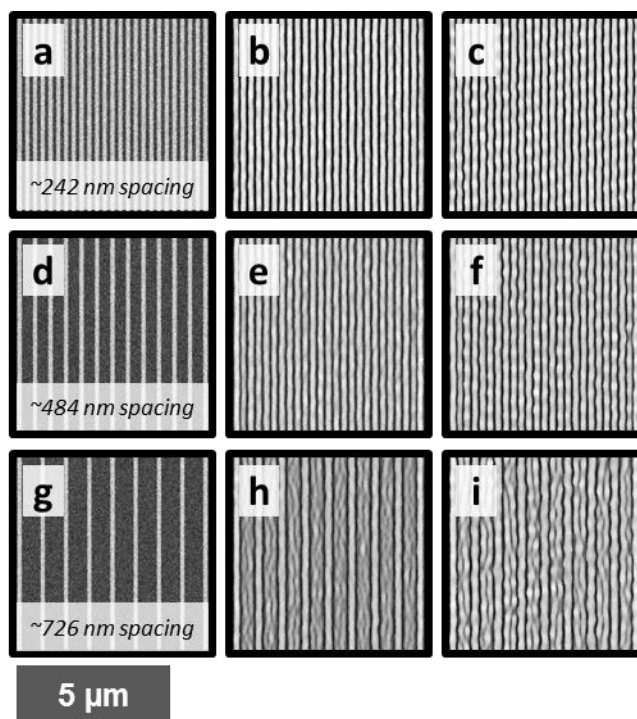


Figure 3.6. Simulated phototropic growth on templated and substrates with vertically polarized illumination with $\lambda = 630$ nm. Simulations were performed with periodic boundary conditions. Substrates have templates with (a)-(c) ~ 242 nm spacing, (d)-(f) ~ 484 nm spacing, or (g)-(i) ~ 727 nm spacing. Panels show (a), (d), (g), initial nucleation step; (b), (e), (h), intermediate stage of growth; and (c), (f), (i), final stage of growth.

Figure 3.4 shows overlapping images from Figure 3.2 and 3.3, highlighting the relationship between the spacing of phototropically grown lamellae and the underlying templated platinum ridges. As expected, the spacing of the Pt templates corresponds exactly to either every lamella (Figure 3.4a, 242 nm spacing), every other lamella (Figure 3.4b, 484 nm spacing), or every two lamellae (Figure 3.4c, 726 nm spacing).

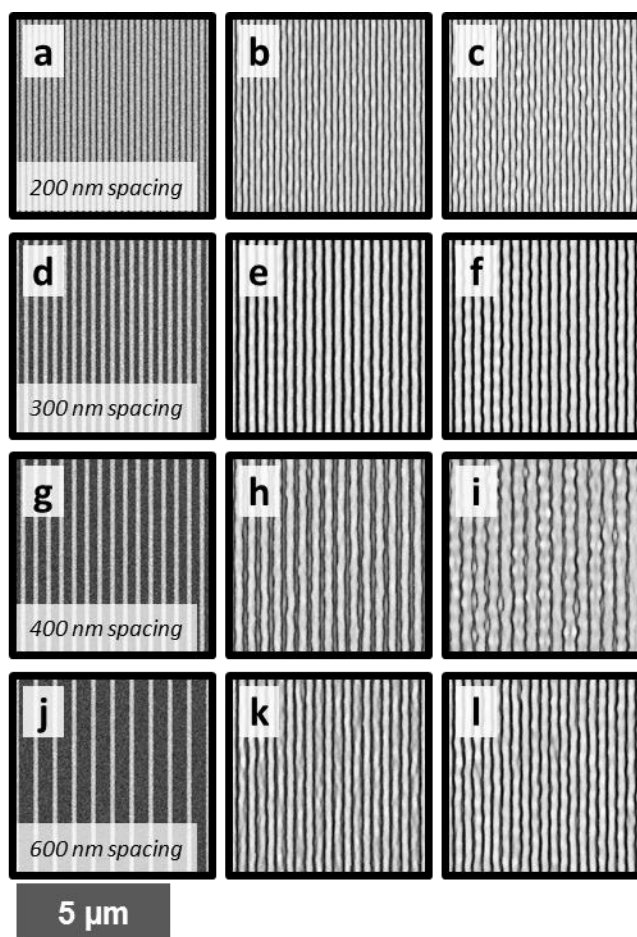


Figure 3.7. Simulated phototropic growth on templated Pt substrates with vertically polarized illumination with $\lambda = 630$ nm. Simulations were performed with periodic boundary conditions. Substrates have 100 nm tall x 100 nm wide Pt ridges with (a)-(c) 200 nm spacing, (d)-(f) 300 nm spacing, (g)-(i) 400 nm spacing, or (j)-(l) 600 nm spacing. Panels show (a), (d), (g), (j) initial nucleation step; (b), (e), (h), (k) intermediate stage of growth; and (c), (f), (i), (l) final stage of growth.

The results of 2D FT analysis performed on phototropically grown films deposited on templated and non-templated substrates, including those shown in Figure 3.2 and 3.3, are given in Figure 3.5. Figure 3.5a gives the average measured vertical full width at half maximum (FWHM) for the primary peak in 2D FT spectra of phototropically grown films deposited on templated and non-templated substrates. The vertical FWHM is reported in degrees and was generated by converting the 2D FT spectra from Cartesian to polar coordinates. This angular value is a figure-of-merit for the pattern fidelity in which smaller values correspond to a relatively higher pattern fidelity and straighter lamellae (lower angular spread). The data show that relative to films deposited on substrates with no template (vertical FWHM of $\sim 30^\circ$), pattern fidelity was greatly improved for phototropically grown films deposited on templates with spacings at 1x (242 nm) or 2x (484 nm) the pattern period, exhibiting a vertical FWHM of $< 1^\circ$. For phototropically grown films deposited on templates with a spacing of 3x the pattern period (726 nm), the results are less reproducible, but range from a similar level of improvement as the results for 1x and 2x template spacing ($\sim 1^\circ$) to marginal improvement over films deposited without templates ($\sim 20\text{-}25^\circ$).

Figure 3.5a also gives the vertical FWHM for the template substrates themselves. Because the templated substrates were lithographically patterned, the only defects present were due to errors in the fabrication process. Thus, there was no expected branching or undulation of the pattern and the templates consisted solely of multiple and mutually parallel lines. Vertical FWHM for the templated substrates were predictably low, corresponding to high pattern fidelities. Furthermore, especially for substrates with a template spacing of 242 nm or 484 nm, the relatively high pattern fidelities were reproduced by the phototropically grown films, as demonstrated by their nominally equivalent vertical FWHM values.

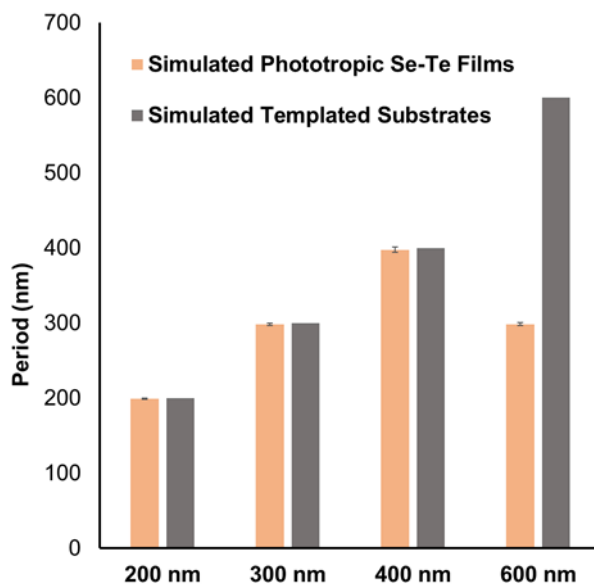


Figure 3.8. Chart showing the periods of simulated templates and phototropically grown structures in Figure 7. Measured periods for the simulated phototropically grown films were 199 ± 1 , 299 ± 2 , 398 ± 3 , and 299 ± 2 nm for the 200, 300, 400, and 600 nm templated substrates, respectively.

Figure 3.5b gives the average measured period for phototropically grown films deposited on templated and non-templated substrates. Pattern period was defined as the centroid frequency of the primary peak in the 2D FT spectra. For films on templated substrates, pattern period was confined to 242 nm. Standard deviations were relatively low, with values of ~ 0.5 nm for a template spacing of 242 nm or 484 nm and a standard deviation of ~ 2 nm for a template spacing of 726 nm. For films on non-templated substrates, the pattern period exhibited a relatively larger range of values with a standard deviation of ~ 8 nm. The data suggest that templated substrates were able to enforce or confine the period of phototropically grown films to a relatively more precise range of values than what was observed for phototropically grown films on non-templated substrates. This effect was observed to be stronger when templates with smaller spacing were used (i.e., 242 nm vs. 726 nm).

This phenomenon is also illustrated by the alignment of the templated substrates and resulting films as shown in Figure 3.4.

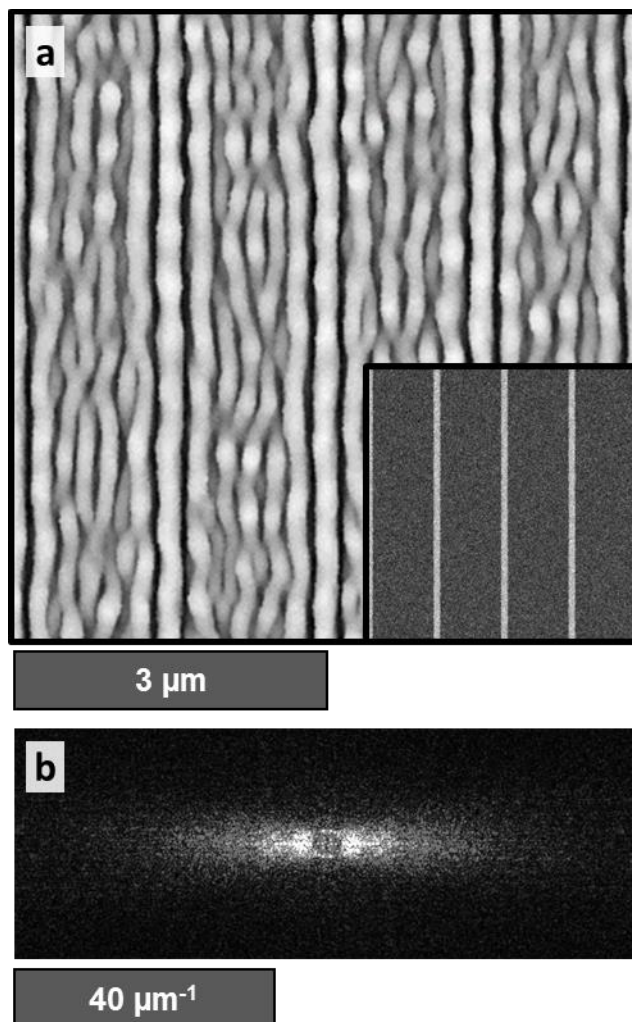


Figure 3.9. (a) Simulated phototropic growth on templated substrate with vertically polarized illumination with $\lambda = 630$ nm. Simulations were performed with periodic boundary conditions. Substrate has 100 nm tall x 100 nm wide Pt ridges with 1.5 μm spacing. Inset in (a) shows simulated substrate; inset side is 6 μm . (b) 2D FT of image in (a).

Figure 3.6 shows the early, intermediate, and resulting simulated phototropic growth of Se-Te on Pt substrates with templated Pt ridges spaced at either ~ 242 nm (Figure 3.6a-c), ~ 484 nm (Figure 3.6d-f), or ~ 726 nm (Figure 3.6g-i). Similar to what was demonstrated experimentally in

Figure 3.3-3.5, templates demonstrate improved fidelity and straighter features in the phototropically grown films. Furthermore, as was observed experimentally, the best improvements are observed when templates are either in perfect registry with lamellae (i.e., ~242 nm spacing in Figure 3.3a and 3.6c) or spaced to every other lamella (i.e., ~484 nm spacing in Figure 3.3b and 3.6f). Though pattern fidelity is still improved over non-templated substrates, significant pattern defects are observed when templates are spaced to every two lamellae (i.e., ~726 nm spacing in Figure 3.3c and 3.6i).

In order to determine the extent to which templated substrates enforced phototropically grown film periods, a set of phototropic growth simulations on templated substrates with spacings out of resonance with the natural period (~242 nm) was performed, the various stages of which are provided in Figure 3.7. The substrates onto which phototropic growth simulations were performed included templated substrates with 100 nm x 100 nm Pt ridges with spacings of 200 nm (Figure 3.7a-c), 300 nm (Figure 3.7d-f), 400 nm (Figure 3.7g-i), and 600 nm (Figure 3.7j-l). Figure 3.8 gives the measured periods of the templated substrates and phototropic growth simulations in Figure 3.7. The measured periods of the phototropic grown simulations were 199 ± 1 , 299 ± 2 , 398 ± 3 , and 299 ± 2 nm for the 200 nm, 300 nm, 400 nm, and 600 nm spaced templates, respectively. The results in Figure 3.8 suggest that the templates can confine the optical scattering and/or enforce pattern period over a wide range of spacings. In particular, for the 200 nm, 300 nm, and 400 nm templates, the period is enforced to exactly the spacing of the templates themselves. For the 600 nm templates, the period is instead enforced to ~1/2 the template spacing, matching that of the 300 nm templates. All periods observed on the templated substrates in Figure 3.7 are substantially different to the natural lamellar period at these conditions on a non-templated substrate (~242 nm).

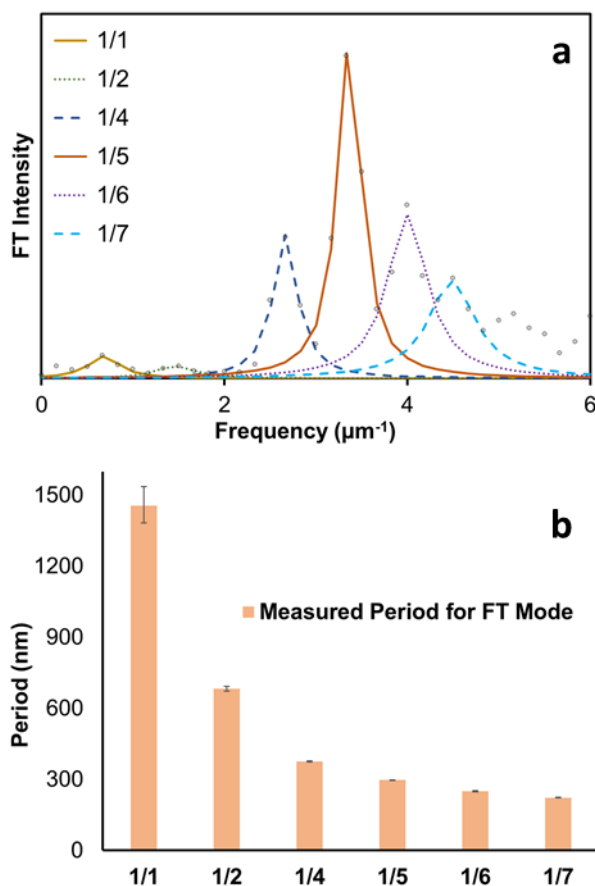


Figure 3.10. (a) Plot showing different frequency modes present in the FT spectra in Figure 3.9b. (b) Chart showing the pattern period measured from the frequencies observed in the plot in (a). Notated and observed FT modes correspond to approximately 1x, 2x, 4x, 5x, 6x, and 7x the frequency of the Pt ridges. Similarly, measured pattern periods at 1383-1528, 673-694, 372-378, 296-298, 248-252, and 222-224 nm correspond to approximately 1x, 1/2, 1/4, 1/5, 1/6, and 1/7 the period of the templated ridges.

Furthermore, given that the 200 nm templates yielded lamellae with a nominal period of 200 nm and that the 600 nm templates were observed to yield lamellae at 1/2 their nominal spacing, it is notable that the 400 nm templates did not produce lamellae with a period of 200 nm. This observation suggests that the generation of periods substantially smaller than the natural lamellar period at a

given set of illumination conditions may require perfect registry of templates at the desired period in order to optically confine pattern formation to those metastable modes.

Figure 3.9a shows a simulated phototropically grown Se-Te film deposited on a templated Pt substrate with Pt ridges at a spacing of 1.5 μm . A 2DFT spectrum of the image in Figure 3.9a is provided in Figure 3.9b. Substantial straightening is observed in the features on and immediately adjacent to the Pt ridges. In the region between the ridges, the pattern demonstrates little, if any, straightening. Figure 3.10a shows a plot of the horizontal cross-section of the 2DFT in Figure 3.9b. There are many frequencies and pattern modes shown in this plot, all of which are fit to Lorentzian functions. Figure 3.10b shows the real space periods as calculated from the frequency peak fits in Figure 3.10a. The observed real-space period modes correspond to approximately 1x, 1/2, 1/4, 1/5, 1/6, and 1/7 the templated ridge spacing (1500 nm). In contrast to the relatively simple patterns in Figure 3.7, the simulated film in Figure 3.9 includes a much more complex set of inter-lamellar spacings, comprising nearly a full harmonic series, though notably omitting the 3x frequency (1/3 the pattern period). This may be due to the fact that the 1/3 pattern period would be at ~ 500 nm, which is very close to 2x the natural period (~ 242 nm) and may not be physically accessible. Thus, the 3x frequency mode may collapse into either the natural period or at twice the 3x frequency in the mode assigned to the 6x frequency mode.

Figure 3.11 shows an SEM image and corresponding 2D FT of a phototropically grown film near the edge of a templated region on the growth substrate. In this sample, there is an angular offset of about 10° between the angle of polarization for the incident illumination and the orientation of the templates on the substrate, as indicated by the yellow lines in Figure 3.11a. In addition to the enforcement of period as suggested by the data in Figure 3.5-3.10, the templated substrates were also

observed to enforce the orientation of the phototropically grown patterns. This enforcement can also be measured and observed in the 2D FT spectrum in Figure 3.11b as a superposition of the two sets of patterns corresponding to the orientation-enforced pattern on the left and the optically-enforced pattern on the right side of Figure 3.11a, also at $\sim 10^\circ$.

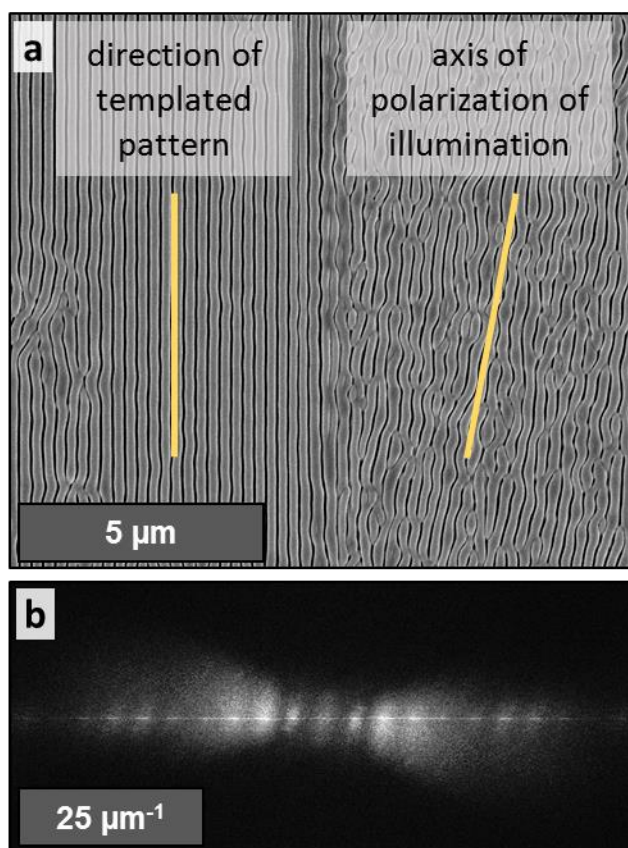


Figure 3.11. (a) SEM image and (b) 2D FT spectrum of phototropically grown Se-Te showing detail at the edge of a templated pattern. Yellow lines correspond to the orientation of the template (left) and axis of polarization of the incident illumination during the deposition (right).

In order to determine the extent to which templated substrates enforced the orientation of phototropically grown films, a set of phototropic growth simulations on templated substrates was performed in which the axis of polarization of the illumination during the simulated growth was varied. Figure 3.12 shows these simulated phototropically grown Se-Te films at the aligned condition

(Figure 3.12a), 20° offset (Figure 3.12b), 40° offset (Figure 3.12c), 45° offset (Figure 3.12d), and 50° offset (Figure 3.12e). Figure 3.12a and b demonstrate no significant difference between film morphology when the axis of polarization is aligned to the template vs. when the axis of polarization is 20° offset. The enforcement of pattern orientation by the template persists with little or no change to film morphology up until ~40° offset. Between 40° and 50° offsets, there is a superposition of patterns both aligned with the template and aligned with the axis of polarization. At and above 50° offsets, the major component of the pattern is aligned with the axis of polarization and the template no longer strongly enforces the orientation of lamellae.

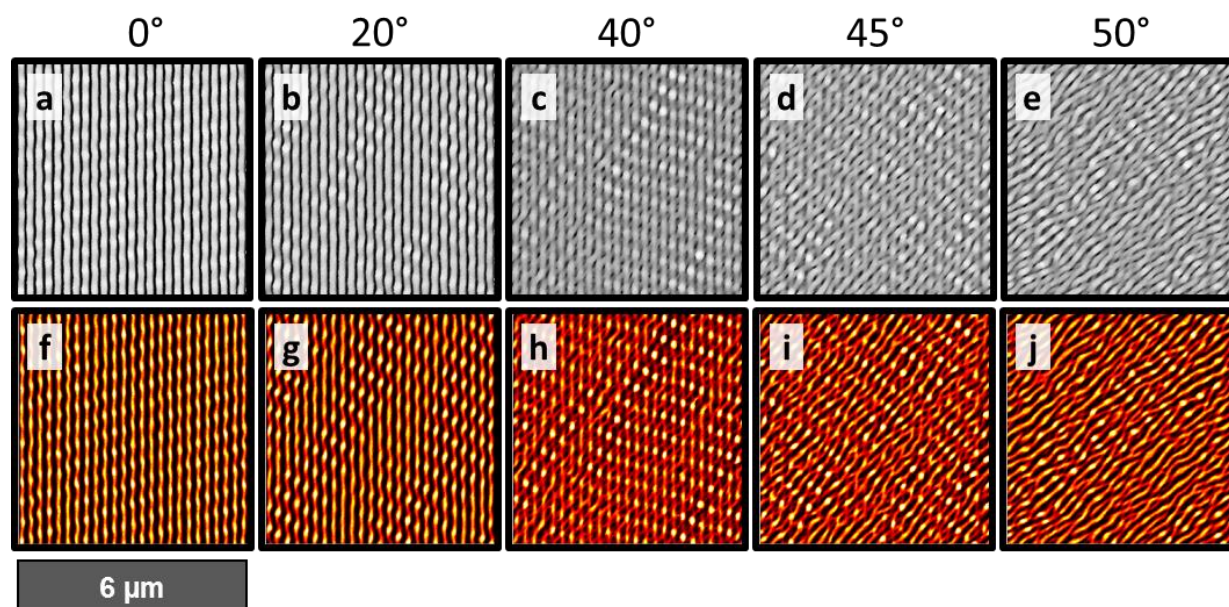


Figure 3.12. Simulated phototropic growth on templated Pt substrates. Simulations were performed with periodic boundary conditions. Substrates have 100 nm tall x 100 nm wide Pt ridges with ~242 nm spacing. Illumination wavelength was $\lambda = 630$ nm with polarizations at (a) 0°, (b) 20°, (c) 40°, (d) 45°, or (e) 50°. Images in (f)-(j) show light absorption profiles for the simulated films in (a)-(e), respectively.

Figure 3.12f-j show the calculated absorption profiles of the films in the Figure 3.12a-e, respectively. Between 0° and 40°, the peak absorption in the tips of the lamellae is observed to

decrease as the axis of polarization moves farther out of alignment with the templates (and pattern orientation). Notably, for some of the higher polarization offsets (i.e., 40° and 45°), the component of the films' patterns aligned with the axis of polarization was more emphasized in the absorption profiles (Figure 3.12h and i) than in the simulated images (Figure 3.12c and d), demonstrating the contribution to pattern orientation by the illumination polarization axis and its competition with the pattern orientation enforced by the templates. For the simulated film at a 50° offset, the absorption profile (Figure 3.12j) demonstrated increased peak absorption (relative to films at a 40° or 45° offset) in the tips of the lamellae. Though the pattern in Figure 3.12e showed no substantial influence by or competition with the underlying template, the absorption intensity observed in Figure 12j was lower than what was observed in Figure 3.12f or g. This is likely due to the lower pattern fidelity associated decrease in resonance between scattered illumination intensity and absorbing material.

3.3 Conclusion

Phototropic growth of Se-Te demonstrates spontaneous and self-optimizing pattern formation directed by both illumination wavelength and polarization, though pattern fidelities are generally low. Using extrinsic optical scatterers as templates for phototropic growth, Se-Te films can demonstrate pattern fidelities not normally accessible on non-templated substrates. Furthermore, both experiments illustrate the ability of templated substrates to enforce both pattern period and pattern orientation in phototropically grown Se-Te films. Templates act simultaneously as oriented nucleation and oriented scattering sites, leading to high fidelity structures, as well as expanding the range of periods and pattern orientations accessible to phototropically grown films under a given set of illumination conditions. Simulations confirm the ability of templates to enforce pattern orientation

and pattern periods. For example, phototropically grown films on templated substrates can demonstrate periods at least ~80-165% of the natural period under a given set of illumination conditions. Similarly, the orientation of phototropically grown films on templated substrates can be enforced with an up to ~40° offset in the axis of polarization to the template orientation. In summary, the use of optical scatterers as templates during phototropic growth demonstrates high pattern fidelity and complex morphological modes otherwise inaccessible in the phototropic growth process.

3.4 Experimental Methods and Materials

Materials and Chemicals

SeO₂ (Aldrich, 99.999% trace metals basis), TeO₂ (Aldrich, 99.995% trace metals basis), Buffer HF Improved (BHF) (Transene, Ammonium Hydrogen Difluoride Solution), H₂SO₄ (J.T. Baker, 90-100%), Ga (Alfa Aesar, 6mm diameter pellets, 99.9999% trace metals basis), In (ESPI Metals, shot, 99.9999%), Ti (Kurt J. Lesker, 1/8" Diameter x 1/8" Long, 99.995% Pure), Pt (Kurt J. Lesker, 1/8" Diameter x 1/8" Long, 99.99% Pure), Acetone (BDH, ACS Grade, 99.5% min.), Isopropyl Alcohol (BDH, ACS Grade, 99.5% min. and VWR, 99.5%), poly(methyl methacrylate) (PMMA) (MicroChem 950 PMMA A3), methyl isobutyl ketone (J.T. Baker, >90%), and Ir wire (Alfa Products, 1mm dia., 99.9%) were used as received. H₂O (Barnstead Nanopure Infinity Ultrapure Water System, $\rho = 18.3 \text{ M}\Omega\text{-cm}$) was used throughout.

For working electrodes, n⁺-silicon (Addison Engineering Inc., As-doped, $\rho = 0.001\text{-}0.004 \text{ }\Omega\text{-cm}$, [111], $525 \pm 25 \text{ }\mu\text{m}$ thick, SSP) was used. For electrode construction, Loctite 1C Hysol Epoxy Adhesive, Conductive Silver Paint (SPI Supplies), Clear Nail Polish (Sally Hansen "Hard as Nails

Xtreme Wear”), tinned Cu wire (AWG 22), and glass tubing (7740 Borosilicate Pyrex, 9mm OD x 1.0mm wall thickness) were used.

Preparation of Pt Substrates

Pt-coated n⁺-Si substrates used as working electrodes in the deposition of Se-Te were fabricated via electron beam evaporation of target metals onto n⁺-Si wafers. Before being loaded into the electron beam evaporator’s vacuum chamber, n⁺-Si wafers were etched in BHF for a minimum of 20 s to remove the native silicon oxides. In order to make ohmic contact to the n⁺-Si, 15 nm Ti was evaporated onto the top (polished) side of the n⁺-Si wafers. Following this, and without breaking vacuum, 100 nm Pt was evaporated onto the Ti-coated n⁺-Si wafers.

Preparation of Templated Substrates

E-beam resist (PMMA) was spin-coated onto Pt substrates at 3000 rpm for 1 minute to obtain an 100 nm thick layer, which was then cured for 5 minutes at 180 °C. Patterns consisting of 100 nm wide lines with center-to-center distances of 187.5, 242, 375, 484, 726, 750, and 1500 nm were made in AutoCAD and fractured in Layout BEAMER. A Raith Electron Beam Pattern Generator (EBPG) 5000+ was used to write the patterns, with a 5 nA beam and 900 μC/cm² dose, at 100 kV. After patterning, the resist was developed by immersion for 50 seconds in a solution of 1:3 ratio by volume of methyl isobutyl ketone to isopropyl alcohol. Development was stopped by immersion in isopropyl alcohol, and the substrate was dried with a nitrogen gun and cleaved into small (~0.1-0.2 cm²) chips.

Following patterning via electron beam lithography, 50 nm Ti was deposited onto patterned substrates via electron beam evaporation. Liftoff was performed by sonicating in acetone for 30

minutes. Following liftoff, an additional 70 nm Pt was deposited via electron beam evaporation to yield the templated substrates.

Working Electrode Fabrication

The unpolished side of templated and non-templated Pt wafer chips were scratched with prepared Ga-In eutectic (75.5 wt. % gallium, 24.5 wt. % indium) using a carbide-tipped scribe. Electrode mounts were fabricated from tinned copper wire affixed to borosilicate glass tubes with inert epoxy. Wafer chips were then attached to the exposed wire of the electrode mounts with silver paint. After a minimum of 30 minutes, electrodes were sealed and electrically insulated with clear nitrocellulose nail polish.

Iridium Wire Electrode Fabrication

A piece of Ir wire (~30 mm) was soldered to a segment of tinned copper wire and placed in a borosilicate glass tube. The soldered contact and glass tube opening were insulated with inert epoxy.

Photoelectrochemical Depositions

All electrochemical experiments were performed using a Biologic VMP3 Potentiostat, controlled via EC Lab for Windows. Light intensity was measured using a calibrated Si photodiode (Thorlabs FDS100). A three-port Pyrex glass electrochemical cell with an optical glass window was utilized for all photoelectrochemical depositions.

For electrochemical experiments, a three-electrode configuration was used with an Ir wire counter electrode and a Ag/AgCl (3M NaCl, BASi RE-5B) reference electrode. Working electrodes were Pt and templated substrates. The electrodeposition bath was an aqueous solution of 1 M H₂SO₄, 0.020 M SeO₂, and 0.010 M TeO₂. Before deposition, electrodes were rinsed with H₂O. Films were deposited until a charge density of -750 mC cm⁻² had been passed. Applied deposition potential was -100 mV vs. Ag/AgCl. The light source used during all depositions was a red Thorlabs LED (Thorlabs M625L4). The LED had an intensity weighted average wavelength of 630 nm, and a spectral bandwidth of 17 nm, and was powered by an LED driver and power supply (Thorlabs LEDD1B and KPS101). The output from the LED was passed through a linear polarizer (Thorlabs LPVISE200-A) and collected with an aspheric condenser lens (Edmund Optics, Ø = 75 mm, f = 50 mm). A 600 grit diffuser (Thorlabs DG20) was placed in front of the window of the electrochemical cell to produce illumination of uniform intensity incident on the working electrodes. An illumination power density of 50 mW cm⁻² was used during the photoelectrochemical deposition.

Sample Preparation and Image Acquisition

After electrodeposition, a razor blade was used to remove samples from their electrode mounts. An acetone bath was used to remove residual nitrocellulose nail polish and silver paint. All scanning electron microscopy was performed using an FEI Nova NanoSEM 450 with an accelerating voltage of 5 kV. A through-lens (immersion) secondary electron detector was utilized at a working distance of 5 mm. Compositional analysis was performed using an electron dispersive X-ray spectroscopy (EDS) module. Images were either obtained at a magnification of 6250 X or 25 kX.

Image resolution was either 4096 or 2048 pixels wide, respectively. Gwyddion (gwyddion.net) was used to perform Fourier analysis on the large-area images (obtained at 6250 X).

Optical Modeling and Growth Simulation

The growths of the photoelectrochemically deposited films were simulated with an iterative growth model in which electromagnetic simulations were first used to calculate the local photocarrier-generation rates at the film surface. Then, mass addition was simulated via a Monte Carlo method wherein the local photocarrier-generation rate weighted the local rate of mass addition along the film surface.

Growth simulations began with a semi-infinite planar platinum substrate patterned with 100 nm wide platinum ridges spaced 200 nm, 242.5 nm, 300 nm, 400 nm, 485 nm, 600 nm, and 727.5 nm apart. In the first step, the light-absorption profile under a linearly polarized, plane-wave illumination source was calculated using full-wave finite-difference time-domain (FDTD) simulations (“FDTD Solutions” software package, Lumerical) with periodic boundary conditions along the substrate interface. In the second step, a Monte Carlo simulation was performed in which an amount of mass, equaling that of a 15 nm planar layer covering the simulation area, was added to the upper surface of the structure with a probability F :

$$F(G) = G \prod_{i=1}^3 \frac{x_i}{r_i} \quad (\text{Equation 1})$$

where G is the spatially dependent photocarrier-generation rate at the deposit/solution interface, x_i is the fraction of i^{th} nearest neighbors occupied in the cubic lattice, and r_i is the distance to the i^{th} nearest neighbor. The multiplicative sum in the definition of this probability (Equation 1)

serves to reduce the surface roughness of the film so as to mimic the experimentally observed surface roughness. A value of $n = 1.33$ was used as the refractive index of the growth solution, regardless of wavelength.³⁶ Simulations of the film morphology utilized the intensity-weighted average wavelengths, λ_{avg} , of the experimental sources. The electric-field vector of the illumination was oriented at 0° , 20° , 40° , 45° , and 50° off normal with respect to the orientation of the templated pattern. A two-dimensional square mesh with a lattice constant of 10 nm was used for the simulations. After the initial Monte Carlo simulation, the absorbance of the new, structured film was then calculated in the same manner as for the initial planar film, and an additional Monte Carlo simulation of mass addition was performed. This process of absorbance calculation and mass addition was repeated for a total of 15 iterations.

3.5 References

1. Hulteen, J. C.; Van Duyne, R. P., Nanosphere lithography: A materials general fabrication process for periodic particle array surfaces. *Journal of Vacuum Science & Technology A: Vacuum, Surfaces, and Films* **1995**, *13* (3), 1553-1558.
2. Sun, F.; Cai, W. P.; Li, Y.; Cao, B.; Lu, F.; Duan, G.; Zhang, L., Morphology Control and Transferability of Ordered Through-Pore Arrays Based on the Electrodeposition of a Colloidal Monolayer. *Advanced Materials* **2004**, *16* (13), 1116-1121.
3. Xia, Y.; Whitesides, G. M., Soft Lithography. *Angewandte Chemie International Edition* **1998**, *37* (5), 550-575.
4. Soolaman, D. M.; Yu, H.-Z., Monolayer-Directed Electrodeposition of Oxide Thin Films: Surface Morphology versus Chemical Modification. *The Journal of Physical Chemistry C* **2007**, *111* (38), 14157-14164.
5. Ogata, Y.; Kobayashi, K.; Motoyama, M., Electrochemical metal deposition on silicon. *Curr Opin Solid St M* **2006**, *10* (3-4), 163-172.
6. Ingole, S.; Aella, P.; Hearne, S. J.; Picraux, S. T., Directed assembly of nanowire contacts using electrodeposition. *Applied Physics Letters* **2007**, *91* (3), 033106.

7. Chen, P.; Zhang, R.; Zhao, Z. M.; Xi, D. J.; Shen, B.; Chen, Z. Z.; Zhou, Y. G.; Xie, S. Y.; Lu, W. F.; Zheng, Y. D., Growth of high quality GaN layers with AlN buffer on Si(111) substrates. *Journal of Crystal Growth* **2001**, 225 (2-4), 150-154.
8. Chang, J. R.; Yang, T. H.; Ku, J. T.; Shen, S. G.; Chen, Y. C.; Wong, Y. Y.; Chang, C. Y., GaN Growth on Si(111) Using Simultaneous AlN/ α -Si₃N₄ Buffer Structure. *Japanese Journal of Applied Physics* **2008**, 47 (7), 5572-5575.
9. Kim, J. H.; Lange, F. F., Seeded Epitaxial Growth of PbTiO₃ Thin Films on (001) LaAlO₃ using the Chemical Solution Deposition Method. *Journal of Materials Research* **2011**, 14 (4), 1626-1633.
10. Gu, C. Z., Enhanced electron emission from diamond film deposited on pre-seeded Si substrate with nanosized diamond power. *Applied Surface Science* **2005**, 251 (1-4), 225-229.
11. Zhu, D.; Ming, L.; Huang, M.; Zhang, Z.; Huang, X., Seed-assisted growth of high-quality multi-crystalline silicon in directional solidification. *Journal of Crystal Growth* **2014**, 386, 52-56.
12. Tamboli, A. C.; Chen, C. T.; Warren, E. L.; Turner-Evans, D. B.; Kelzenberg, M. D.; Lewis, N. S.; Atwater, H. A., Wafer-Scale Growth of Silicon Microwire Arrays for Photovoltaics and Solar Fuel Generation. *IEEE Journal of Photovoltaics* **2012**, 2 (3), 294-297.
13. Yue, L.; Gao, W.; Zhang, D.; Guo, X.; Ding, W.; Chen, Y., Colloids seeded deposition: growth of titania nanotubes in solution. *J Am Chem Soc* **2006**, 128 (34), 11042-3.
14. Sugunan, A.; Warad, H. C.; Boman, M.; Dutta, J., Zinc oxide nanowires in chemical bath on seeded substrates: Role of hexamine. *Journal of Sol-Gel Science and Technology* **2006**, 39 (1), 49-56.
15. Baruah, S.; Dutta, J., Hydrothermal growth of ZnO nanostructures. *Sci Technol Adv Mater* **2009**, 10 (1), 013001.
16. Chen, H.-G.; Li, Z.-W.; Lian, H.-D., Control of epitaxial growth orientation in ZnO nanorods on c-plane sapphire substrates. *Thin Solid Films* **2010**, 518 (19), 5520-5524.
17. Graham, L. M.; Cho, S.; Kim, S. K.; Noked, M.; Lee, S. B., Role of boric acid in nickel nanotube electrodeposition: a surface-directed growth mechanism. *Chem Commun (Camb)* **2014**, 50 (5), 527-9.
18. Choi, K. S., Shape control of inorganic materials via electrodeposition. *Dalton Trans* **2008**, (40), 5432-8.
19. Mettela, G.; Kulkarni, G. U., Facet selective etching of Au microcrystallites. *Nano Research* **2015**, 8 (9), 2925-2934.
20. Boercker, J. E.; Schmidt, J. B.; Aydil, E. S., Transport Limited Growth of Zinc Oxide Nanowires. *Crystal Growth & Design* **2009**, 9 (6), 2783-2789.
21. Li, H. F.; Kar, A. K.; Parker, T.; Wang, G. C.; Lu, T. M., The morphology and texture of Cu nanorod films grown by controlling the directional flux in physical vapor deposition. *Nanotechnology* **2008**, 19 (33), 335708.

22. Baruah, S.; Dutta, J., pH-dependent growth of zinc oxide nanorods. *Journal of Crystal Growth* **2009**, *311* (8), 2549-2554.
23. Lymperakis, L.; Neugebauer, J., Large anisotropic adatom kinetics on nonpolar GaN surfaces: Consequences for surface morphologies and nanowire growth. *Physical Review B* **2009**, *79* (24).
24. Krauskopf, A. A.; Jimenez, A. M.; Lewis, E. A.; Vogt, B. D.; Muller, A. J.; Kumar, S. K., Mechanisms of Directional Polymer Crystallization. *ACS Macro Lett* **2020**, *9* (7), 1007-1012.
25. Dasog, M.; Carim, A. I.; Yalamanchili, S.; Atwater, H. A.; Lewis, N. S., Profiling Photoinduced Carrier Generation in Semiconductor Microwire Arrays via Photoelectrochemical Metal Deposition. *Nano Lett* **2016**, *16* (8), 5015-21.
26. Qin, C.; Campbell, B. M.; Shen, M.; Zhao, T.; Sadtler, B., Light-Driven, Facet-Selective Transformation of Cuprous Oxide Microcrystals to Hollow Copper Nanoshells. *Chemistry of Materials* **2019**, *31* (19), 8000-8011.
27. Yoo, B.; Xiao, F.; Bozhilov, K. N.; Herman, J.; Ryan, M. A.; Myung, N. V., Electrodeposition of Thermoelectric Superlattice Nanowires. *Advanced Materials* **2007**, *19* (2), 296-299.
28. Sadtler, B.; Burgos, S. P.; Batara, N. A.; Beardslee, J. A.; Atwater, H. A.; Lewis, N. S., Phototropic growth control of nanoscale pattern formation in photoelectrodeposited Se-Te films. *Proc Natl Acad Sci U S A* **2013**, *110* (49), 19707-12.
29. Carim, A. I.; Batara, N. A.; Premkumar, A.; Atwater, H. A.; Lewis, N. S., Self-Optimizing Photoelectrochemical Growth of Nanopatterned Se-Te Films in Response to the Spectral Distribution of Incident Illumination. *Nano Lett* **2015**, *15* (10), 7071-7076.
30. Carim, A. I.; Batara, N. A.; Premkumar, A.; Atwater, H. A.; Lewis, N. S., Polarization Control of Morphological Pattern Orientation During Light-Mediated Synthesis of Nanostructured Se-Te Films. *ACS Nano* **2016**, *10* (1), 102-11.
31. Carim, A. I.; Batara, N. A.; Premkumar, A.; May, R.; Atwater, H. A.; Lewis, N. S., Morphological Expression of the Coherence and Relative Phase of Optical Inputs to the Photoelectrodeposition of Nanopatterned Se-Te Films. *Nano Lett* **2016**, *16* (5), 2963-8.
32. Simonoff, E.; Lichterman, M. F.; Papadantonakis, K. M.; Lewis, N. S., Influence of Substrates on the Long-Range Order of Photoelectrodeposited Se-Te Nanostructures. *Nano Lett* **2019**, *19* (2), 1295-1300.
33. Simonoff, E.; Van Munoz, L. X.; Lewis, N. S., Increased spatial randomness and disorder of nucleates in dark-phase electrodeposition lead to increased spatial order and pattern fidelity in phototropically grown Se-Te electrodeposits. *Nanoscale* **2020**, *12* (44), 22478-22486.
34. Carim, A. I.; Hamann, K. R.; Batara, N. A.; Thompson, J. R.; Atwater, H. A.; Lewis, N. S., Template-free synthesis of periodic three-dimensional PbSe nanostructures via photoelectrodeposition. *J Am Chem Soc* **2018**, *140* (21), 6536-6539.

35. Hamann, K. R.; Carim, A. I.; Meier, M. C.; Thompson, J. R.; Batara, N. A.; Yermolenko, I. S.; Atwater, H. A.; Lewis, N. S., Optically tunable mesoscale CdSe morphologies via inorganic phototropic growth. *Journal of Materials Chemistry C* **2020**, *8* (36), 12412-12417.
36. Hale, G. M.; Querry, M. R., Optical Constants of Water in the 200-nm to 200- μ m Wavelength Region. *Appl. Opt.* **1973**, *12*, 555-563.